

Morphology, exhumation, and Holocene erosion rates
from a tropical glaciated mountain range:
the Cordillera Blanca, Peru

by

Keith R. Hodson

Department of Earth & Planetary Sciences
McGill University, Montreal
August 2012

A thesis to be submitted to McGill University in partial
fulfillment of the requirements of the degree of Masters of
Science

Acknowledgements

This project was made possible with the support of many people who helped me along the way. First and foremost, none of the work from the last two years would have ever been realized without the aid of my advisor Dr. Sarah Hall. It is only with her continued support, guidance, and attention that this project has grown to its current state of completion. Cosmogenic and thermochronologic analyses were made possible with the aid of Melanie Michalak, Daniel Farber, and Jeremy Hourigan from the University of California, Santa Cruz, Earth and Planetary Sciences department. Undergraduates Phillip Greene, Marc-Antoine Fortin, and Kasparas Spokas were invaluable in the lab and during field work, and I wish them all luck on their future endeavors. Thanks to Marc-Antoine Longpré for help with translation. Big thanks to officemates Tyler Doane, Simon Yang, and David Corozza for the company and continuing support, even now that we are spread across the globe. Thanks to Anne Kosowski, Kristy Thornton and Angela Di Ninno for ensuring a smooth graduate school experience. And lastly: endless thanks to my parents for remaining supportive and encouraging this whole time, even though I ran away to Canada.

Table Of Contents

0 - Abstract to the Thesis and Résumé	1
1 - Introduction	5
2 - Regional Overview	7
2.1 Regional Climate and Glaciation	8
2.2 Tectonic Setting	10
2.3 Important Units	11
2.3.1 The Coastal Batholith	11
2.3.2 The Chicama Formation	12
2.3.3 The Calipuy Formation	12
2.3.4 The Yungay Formation	12
2.3.5 The Cordillera Blanca Batholith and Carhuish Stock	13
2.3.6 Quaternary Deposits	14
2.4 Extension in the Cordillera Blanca	14
2.5 Emplacement and Uplift of the Cordillera Blanca Batholith	18
3 - Methods	20
3.1 Cosmogenic Radionuclides	21
3.1.1 CRN Production	21
3.1.1.1 The Geomagnetic Field	22
3.1.1.2 Attenuation Through Interaction with Matter	23
3.1.2 Sample Collection	24
3.1.2.1 Incision Rate Samples	24
3.1.2.2 Basin-averaged Erosion Rate Samples	25
3.1.3 Sample Preparation and Analysis	26
3.1.4 Calculating a Surface Exposure Age	27
3.1.5 Calculating an Erosion Rate	28
3.2 Apatite and Zircon U-Th/He Thermochronology	29
3.2.1 Sample Collection	31
3.2.2 Sample Preparation and Analysis	32
3.3 Mapping and Remote Sensing	32
4 - Results	33
4.1 Remote Sensing	33
4.1.1 Basin Morphology	33
4.1.2 Swath Profiles	35
4.2 ¹⁰ Be Basin-averaged Erosion Rates	36
4.3 ¹⁰ Be Exposure Ages	37
4.4 Apatite and Zircon Thermochronology	38

Continued Table Of Contents

5 - Discussion	38
5.1 Patterns in Morphology Along the Cordillera Blanca Mountain Range	38
5.1.1 Models for Topographic Evolution of Normal Fault Footwalls	40
5.1.2 The Glacial Buzzsaw	42
5.1.3 Morphology of the Calejón de Huaylas Supradetachment Basin	43
5.2 Validity of the ^{10}Be Basin-Averaged Erosion Rates	44
5.2.1 Assumption 1: Short Transport Time	44
5.2.2 Assumption 2: Constant Erosion Over the Erosion Time Scale	45
5.2.3 Assumption 3: Well Mixed Sample	46
5.2.4 Estimation of Total Error	47
5.2.5 Comparison to Previous Work	47
5.2.6 Interpretation of ^{10}Be Erosion Rate Results	48
5.3 Regional Patterns in Erosion Rates and Morphology	49
5.4 Patterns in Erosion Along the Cordillera Blanca Mountain Range	52
5.5 River Incision	54
5.6 Exhumation of the Cordillera Blanca Batholith	56
5.7 Regional Patterns of Exhumation	58
5.8 Implications for the Evolution of the Cordillera Blanca and the CBDF	59
6 - Conclusion	61
7 - References Cited	63
Appendix 1: Relationships Between Erosion and Uplift	70

Included Figures

- 1 - Tectonic Map of Northern South America
- 2 - Geographic, Structural, and Rainfall Maps of the Cordillera Blanca
- 3 - Photographs of the Cordillera Blanca Detachment Fault
- 4 - Photographs of Glacial Features
- 5 - Geologic Map of the Cordillera Blanca and Surrounding Region
- 6 - Photographs of Mylonite in the Cordillera Blanca Batholith
- 7 - Morphology and Structures in the Callejón de Huaylas Supradetachment Basin
- 8 - Conceptual Figures for CRN Production
- 9 - Maps of Sample Collection Sites and Regions Used for Morphometric Studies
- 10 - Photographs of Example River Incision Sample Site
- 11 - Photographs of Example Basin-averaged Erosion Rate Sample Site
- 12 - Plots of Basin Morphology Along the Cordillera Blanca Mountain Range
- 13 - Swath Profiles of the Cordillera Blanca Mountain Range
- 14 - ^{10}Be Results and Scaling Scheme Comparison
- 15 - Map of ^{10}Be Basin-averaged Erosion Rates
- 16 - Thermochronologic Age-elevation Relationships
- 17 - Plots of Basin Areas, Slopes, and Modal Elevations
- 18 - Plot of Mean Slope and Mean Elevation for Basins Used for ^{10}Be Analysis
- 19 - Plots of Erosion Rate, Mean Slope, and Local Relief
- 20 - Plots of Exposure Ages and Incision Rates
- 21 - Synthesis Figure of Range Morphology, Erosion, and Geology

Included Tables

- 1 - Morphometric Statistics of Basins along the Western Cordillera Blanca
- 2 - Morphometric Statistics of Other Basins of Interest to this Study
- 3 - ^{10}Be Sample Information
- 4 - ^{10}Be Erosion Rate Results
- 5 - ^{10}Be Exposure Age Results
- 6 - Apatite (U-Th)/He Sample Information and Results
- 7 - Zircon (U-Th)/He Sample Information and Results

Morphology, exhumation, and Holocene erosion rates from a tropical glaciated mountain range: the Cordillera Blanca, Peru

By Keith Hodson

Abstract to the Thesis

Both tectonics and climate profoundly influence orogenesis, but specifics regarding the forcings, interactions and feedbacks are still largely unclear. This study addresses the evolution of the Cordillera Blanca Mountain Range of northern Peru: an elevated, high-relief, 200 km long string of glaciated peaks comprising the spine of the Andes. Extension along the Cordillera Blanca Detachment Fault (CBDF) actively produces relief along the western flank of the range, exceeding several kilometers in many areas. Abundant records of past glaciations span from >440 ka to the present in the form of moraine and bog deposits. Thus, tectonics (active faulting) and climate (glacial erosion) are operating in tandem to produce some of the highest topography in the western hemisphere. Understanding these processes in the Cordillera Blanca will provide an invaluable perspective into tectonic and climatic effects on orogenesis.

Through the combined use of cosmogenic ^{10}Be , low temperature thermochronology and digital terrain analysis, I explore the erosional and morphologic history of the range over a variety of spatial and temporal scales. Significant variations in modern range elevation (maximum, mean, modal and minimum), relief (local and within basins) and slope (maximum, mean and minimum) exist along the strike of the range, potentially reflecting the combined effects of variable displacement along the CBDF and varying degrees of glacial erosion. The morphology of the adjacent supradetachment basin varies as well, containing zones with distinct styles of faulting and basin growth, likely defined in part by the segmentation history of the CBDF.

By combining Holocene-scale ^{10}Be basin-averaged erosion rates with new thermochronologic data, I expand the known denudation history of the range. These two datasets constrain the exhumation and erosional history of the range-forming Cordillera Blanca Batholith from the late Miocene to Holocene, and expand the thermal history of the range southwards to include the older Carhuish Stock. Two new vertical ^{10}Be exposure age transects allow comparison of fluvial incision rates within the Cordillera Blanca Batholith and the older Coastal Batholith. Incision rates from the site in the Cordillera Blanca record uplift on the order of $\sim 1 \text{ mm yr}^{-1}$, and potentially place a minimum constraint on CBDF slip rates at this location. Incision rates from the Coastal Batholith are twice as fast ($\sim 2 \text{ mm yr}^{-1}$) possibly representing large-scale regional uplift. Exhumation rates and erosion rates generally fall between 0.01 and 0.5 mm/yr, suggesting a fairly continuous state of erosion over long-term (10^6 yrs) to recent ($<10^3$ yrs) time scales. Aside from a seemingly isolated zone of elevated erosion rates, no trends are observed along the strike of the mountain range. As the CBDF is believed to display variable slip-rates along strike, it seems that associated base level lowering is not a first order control on basin-averaged erosion rate.

Résumé

Bien qu'il soit établi que la tectonique et le climat influencent profondément l'orogénèse, plusieurs questions demeurent en ce qui a trait aux forçages, interactions et rétroactions. Cette étude se penche sur l'évolution de la cordillère Blanche, dans le nord du Pérou : une chaîne de sommets glacés à haut relief de 200 km de longueur, épine dorsale des Andes. L'extension le long de la faille de détachement de la cordillère Blanche (FDCB) cause la formation de relief sur le flanc ouest de la chaîne sur plusieurs kilomètres dans certaines zones. D'abondantes traces de glaciations passées, datant de plus de 440 ka jusqu'à la période actuelle, sont présentes sous forme de dépôts de moraines et de tourbières. Donc, la tectonique (mouvements de failles actives) et le climat (érosion glaciaire)

opèrent en tandem pour produire l'une des topographies les plus accidentées de l'hémisphère ouest. Une évaluation pointue des procédés en cause dans la cordillère Blanche permettra une meilleure compréhension des effets de la tectonique et du climat sur l'orogénèse.

En utilisant une combinaison de datation par l'isotope cosmogénique ^{10}Be , de thermo-chronologie de basse température et d'analyse de modèles numériques de terrain, cette étude explore l'historique d'érosion et morphologique de la chaîne sur plusieurs échelles spatiales et temporelles. Des variations significatives d'altitude moderne de la chaîne (maximale, moyenne, modale et minimale), de relief (local et en bassin) et de pente (maximale, moyenne et minimale) existent le long de la chaîne et sont potentiellement dues aux effets combinés de mouvements variables le long de la FDCB et de différents degrés d'érosion glaciaire. La morphologie du bassin de supra-détachement adjacent varie également et contient des zones dotées de styles distincts de faille et de développement de bassin, probablement définis en partie par l'historique de segmentation de la FDCB.

En combinant les rythmes d'érosion (âges ^{10}Be , moyennes de bassin à l'échelle holocène) avec de nouvelles données thermo-chronologiques, ces travaux augmentent l'étendue connue de l'historique de dénudation de la chaîne. Ces deux bases de données documentent l'historique d'exhumation et d'érosion du batholithe de la cordillère Blanche depuis la fin du Miocène jusqu'à l'Holocène et étendent l'historique thermal de la chaîne vers le sud pour inclure le plus ancien Carhuish Stock. Deux coupes d'âges d'exposition verticale par ^{10}Be permettent une comparaison des rythmes d'incision fluviale au sein du batholithe de la cordillère Blanche et du plus ancien batholithe côtier. Les rythmes d'incision au site de la cordillère Blanche indiquent un soulèvement d'environ 1 mm par an et suggèrent un glissement minimal de la FDCB de cet ordre à cet endroit. Les rythmes d'incision au batholithe côtier sont deux fois plus rapides (~2 mm par an), possiblement dû à un soulèvement d'échelle régionale. Les rythmes

d'exhumation et d'érosion sont généralement de 0.01 à 0.5 mm par an, indiquant une érosion continue sur le long (10^6 années) et court terme ($<10^3$ années). Outre une zone isolée de rythmes d'érosion apparemment élevés, aucune tendance n'est observée le long de la chaîne de montagnes. Comme la FDCB est connue pour ses rythmes de glissement variables le long de la chaîne, il semble que l'abaissement du niveau de base associé ne soit pas un contrôle de premier ordre sur les rythmes d'érosion moyens à l'échelle du bassin.

1 Introduction

The evolution of mountainous terrain has long been of interest to earth scientists (e.g. Davis, 1899). As a result, our understanding of the processes that build orogens up and erode them back down has seen continuous improvement. The potential for causal links and feedbacks between climate and orogenesis stems from an apparent temporal link between late Cenozoic climate change and the generation of high topography (e.g. Molnar and England, 1990; Raymo and Ruddiman, 1992; Zhang et al., 2001; Lamb and Davis, 2003). While this link remains controversial (e.g. Willenbring and von Blanckenburg, 2010), the idea has spurred the development of numerous theories regarding connections between tectonic and climatic processes on a range of spatial and temporal scales. Predictions regarding the potential for climate and surface processes to influence both the structural and topographic evolution of active mountain belts have been the subject of many recent analog (e.g. Bonnet and Crave, 2003; Bonnet et al., 2008; Cruz et al., 2008; Malavieille and Konstantinovskaya, 2010) and numerical modeling experiments (e.g. Willet, 1999; Hilley and Strecker, 2004; Whipple, 2009). The concept of equilibrium topography and steady-state orogens has been at the center of these experiments, where tectonically driven fluxes of material into an orogen are balanced by the removal of material from the surface (e.g. Willet and Brandon, 2002). In these highly simplified scenarios, predictable responses to changes in the modeled tectonic and climatic forcings can be observed, usually as a transition in range elevation (e.g. Bonnet and Crave, 2003) or the locus of active lithospheric deformation (e.g. Willet, 1999). While some field-based studies have supported causal links between temporal and spatial climate patterns and tectonic and structural deformation (e.g. Montgomery et al, 2001; Montgomery and Brandon, 2002; Montgomery and Stolar, 2006; Berger et al, 2008), most return complex results that do not clearly corroborate model predictions. Further developments in our understanding of the couplings between

climate and tectonics will rely on the characterization of timing, rates, and locations of related events and processes (Whipple, 2009).

To address the need for improved understanding of tectonic and climatic interactions, I quantify surface denudation in the Cordillera Blanca Mountain Range of northern Peru: a glaciated, tectonically active mountain range. The Cordillera Blanca runs for ~200km, comprising the crest of the Andean mountain chain between ~8 and 10°S and containing some of the highest topography on earth, including multiple peaks over 6000 m a.s.l. (Ames, 1998). The Andes are an active orogen, and most of the current contractile deformation is focused along the eastern flank of the range in the Sub-Andean Fold and Thrust Belt (Fig. 1; Gregory-Wodzicki, 2000). In the Cordillera Blanca, however, active extensional deformation along a crustal-scale detachment structure is facilitating large magnitudes of relief production (Figs. 2 and 3; McNulty and Farber, 2002). While the specifics surrounding the mechanisms driving this extension remain unclear, extensional faulting has profoundly influenced the local development of the mountain range and the adjacent supra-detachment basin (Schwartz, 1988; Giovanni et al., 2010). Glaciation has also had a prominent role in shaping the mountain range, and records of past glaciations reach into the Pleistocene (Farber et al., 2005). Modern glaciers still adorn the high peaks, but are limited to elevations over ~4900 m a.s.l. (Fig. 4; Mark and Seltzer, 2005). Thus, the Cordillera Blanca is simultaneously experiencing the effects of tectonic and climatic activity through active faulting and glacial erosion, respectively.

Prior work in the region has begun to characterize the lithologies, structures, and development of the range (e.g. Cobbing et al., 1981; Schwartz, 1988; Giovanni et al., 2010). Many questions remain about the history and geodynamics of the Cordillera Blanca, especially regarding the drivers of regional extension, structural development of the detachment system, uplift and exhumation of the range-forming granitoid batholiths, and timing and extent of glaciations. While this study does not directly address any specific models

regarding drivers of extension in the Cordillera Blanca, it aims to answer the following questions: 1) How do erosion rates vary within and around the Cordillera Blanca? 2) Are there any long or short term variations in rock uplift along the range? 3) Does the range morphology reflect patterns in erosion and uplift? 4) How do patterns of erosion, uplift and morphology relate to structural deformation and glacial erosion?

To address these questions, I utilize: 1) digital terrain analysis to characterize the modern topography, 2) cosmogenic ^{10}Be to quantify average erosion rates within individual basins and rates of river incision over Holocene time scales, and 3) low temperature thermochronology to determine the cooling and exhumation history of the range over million year time scales. Rates and magnitudes of erosion and exhumation can be interpreted as proxies for rates and magnitudes of rock uplift (see Appendix 1; Molnar and England, 1990). In this sense, my results yield uplift information over a range of time scales for the Cordillera Blanca and I connect these findings to the modern topography. The new data are placed into context with the known geologic and climatic history, and I demonstrate: 1) consistency between long and short term rates of erosion; 2) a locus of rapid Holocene erosion rates near the center of the range; 3) along-strike trends in range morphology; and 4) an apparent disconnect between erosion rates and structural deformation. The following work provides an important look at the erosion, uplift and topographic history of the range from ~ 7 Ma to Holocene timescales, and should prove valuable to future studies investigating the structural, thermal, and climatic evolution of the Cordillera Blanca Mountain Range.

2 Regional Overview

The Andean mountain chain runs for over 4000 miles along the western margin of South America. In the north, the range is ~ 200 - 250 km wide, and is generally divided into five range-parallel provinces: (1) The Coastal Plains (2)

The Western Cordillera, (3) The Altiplano, (4) The Eastern Cordillera, and (5) The Sub-Andes (Fig. 1). The Cordillera Blanca runs for ~200 km from ~8 to 10°S along the crest of the Andes (Fig. 2), containing some of the highest elevations in South America, including 27 peaks over 6000 m a.s.l. (Ames, 1998). The western flank of the range is delineated by the impressive Cordillera Blanca Detachment Fault (CBDF; Fig. 2B). The associated Callejón de Huaylas Supradetachment Basin contains the Rio Santa Watershed, one of the few large river systems draining west to the Pacific Ocean (Figs. 2A and 2B). Further west, across the basin from the Cordillera Blanca, is the Cordillera Negra Mountain Range, a ~100 km long mountain front named for the dark Tertiary volcanic units capping the range (Fig. 2A).

A rich glacial history has sculpted the Cordillera Blanca, forming characteristic U-shaped valleys with over-steepened cliffs and moraines (Fig. 4). Modern glaciers still cap the elevated topography (Fig. 2A), awarding the region the designation of being the most glaciated in the tropics (Mark and Seltzer, 2005). Range morphology displays significant north-south trends in peak elevation, catchment relief and mean slope (Giovanni, 2007; Farber and Hancock, *In Prep*). Relief and slope decrease linearly towards the south. Peak elevations trend towards a maximum around Mt. Huascaràn, the highest peak in the region, and decrease towards both the northern and southern range tips.

2.1 Regional Climate and Glaciation

The Cordillera Blanca acts as an orographic barrier to moisture-laden air carried eastwards from the Amazon Basin (Montgomery et al., 2001; Bookhagen and Strecker, 2008; Racoviteanu et al., 2008). While the largest orographic effects on precipitation occur further east in the Sub-Andes (Fig. 1), the rain shadow imposed by the Cordillera Blanca results in 2 to 3 times less moisture reaching the western flank (Fig. 2C; Johnson, 1976). Annual precipitation is

highly seasonal, and most rainfall is received between October and April (Mark and Seltzer, 2005).

Modern glaciers cap peaks at elevations over 4900 m a.s.l., covering over 600 km² and providing the region with the distinction of being the most glaciated mountain range in the tropics (Fig. 2A; Mark and Seltzer, 2005; Rodbell et al., 2009). Modern glacial areas follow along-strike trends in peak elevation, covering up to 39% of basin area near Huascarán (Armstrong et al, 2005).

Abundant records of previous glaciations are preserved in the form of lateral and end moraines, as well as sediment cores from lakes throughout the glacial valleys and Callejón de Huaylas Supradetachment Basin (Rodbell, 1993; Farber et al, 2005; Rodbell et al, 2008; Glasser et al., 2009). Farber et al. (2005) identified two moraine sets associated with the Last Glacial Maximum (LGM), which correlate with moraine sets investigated by Smith et al. (2005) ~140 km to the south in the Junin Plain. Using ¹⁰Be surface exposure dating, both studies produced similar age ranges for the moraines of ~30 to 20 ka and ~20 to 16 ka. Farber et al. (2005) also reported ages from larger, more extensive moraine systems predating the LGM. These moraines returned exposure ages from ca. 120 to 440 ka, possibly supporting the occurrence of up to 3 separate advances at ca. 125, 225, and 440 ka. Glasser et al. (2009) described four to five moraine sets in valleys near the southernmost extent of the Cordillera Blanca. Reported ¹⁰Be ages from these moraines span 12.5 and 7.6 ka, leading the authors to assign the older ages to advances during the Younger Dryas and more recent ages to post-Younger Dryas temperature fluctuations. Preserved lateral moraines found further north near the center of the Cordillera Blanca Mountain Range yield ¹⁰Be ages spanning ~8 to 6 ka, and end moraines with exposure ages of 600 to 400 yrs BP represent an advance during the Little Ice Age (Fortin and Hall, 2011).

2.2 Tectonic Setting

Subduction of the Nazca Plate beneath the South American continent has produced the Andean Mountain Range along the western margin of South America. The oceanic Nazca Plate is currently moving at a velocity of $75 \pm 5 \text{ mm yr}^{-1}$ relative to stable continental South America in the direction N70°E (Norabuena et al., 1998). Convergence at the subduction trench is 68 mm yr^{-1} directed at N76°E (Fig. 1; Norabuena et al., 1998). Two zones of flat-slab subduction are present along the strike of the trench. The northern zone extends from 2-15°S (Fig. 1) and the southern zone extends from 28-33.5°S, each with a corresponding volcanic gap in the overriding plate (Gregory-Wodzicki, 2000). The subduction angle is similar in both flat-slab subduction zones, with the oceanic plate initially descending at an angle of $\sim 30^\circ$ before flattening to near horizontal at $\sim 100\text{km}$ depth (Gutscher et al., 2000; Manea et al., 2012). The location of the north and south flat-slab subduction zones are associated with subducting aseismic ridges (the Nazca Ridge and Juan-de-Fuca Ridge, respectively; Fig. 1), and these have been employed as mechanisms for formation for the flat-slab subduction systems, albeit controversially (Gutcher et al., 2000; Gerya et al., 2009; Manea et al., 2012).

The formation of the Andes is attributed to compressional stresses due to ongoing subduction since the Mesozoic (Megard, 1984). Punctuated episodes of deformation lasting $\sim 10^6$ - 10^7 years were separated by periods of relative quiescence. These episodes of heightened deformation are termed the (1) Mochica (Middle Cretaceous), (2) Peruvian (Late Cretaceous), (3) Incaic (Middle to Late Eocene), (4) Quechua 1 (Early Miocene), (5) Quechua 2 (Middle Miocene), and (6) Quechua 3 (Pliocene; Megard, 1984). The Incaic phase is of particular importance to the Peruvian Andes, as it is deemed responsible for the formation of the large Marañón Fold and Thrust Belt occupying the eastern flank of the Peruvian Andes. Deformation in the Sub-Andean Fold and Thrust Belt (Fig. 1) is attributed to the Quechua 3 phase as well as Quaternary compressional

deformation in the foothills bordering the Amazon Basin (Megard, 1984; Dumont, 1996).

Large-scale extensional faulting is actively deforming the Cordillera Blanca region, and relatively minor extensional structures have been described in the region to the north-east. The tectonic explanation for these structures is still debated (see section 2.4).

2.3 Major Units

2.3.1 The Coastal Batholith.

The Coastal Batholith of Peru is a continuous chain of over 1000 individual plutons extending some 1200 km along the Peruvian coast and extending northwards into southern Ecuador and southwards into Chile (Fig. 5). Ages from the Coastal Batholith span from the mid-Cretaceous to the late Eocene (100 to 37 Ma; Cobbing et al., 1981; Atherton and Petford, 1996) and have been estimated to contain up to 1000 individual plutonic events (Cobbing et al., 1981). Regionally, the Coastal Batholith is notable for comprising the core of the Cordillera Negra Mountains and is extensively exposed in the northern Rio Santa River Valley, which incises through the Coastal Batholith on its path to the Pacific Ocean.

The Coastal Batholith intruded into a young rift basin that was present off the Peruvian coast at least until the batholith began to form (Anderson, 1990). There is no clear evidence that subduction had initiated before the emplacement of the Coastal Batholith began, but it seems likely (Atherton, 1990). Geochemical and geophysical analyses are consistent with the melts being produced via decompression melting of the fresh oceanic crust, not metasomatism, and they propagated along networks of dykes and sills to depths of 2-3 km where they crystallized into the wide and flat, tabular morphology of the Coastal Batholith (Atherton, 1990; Haederle and Atherton, 2002).

2.3.2 The Chicama Formation.

The Jurassic Chicama Formation is an approximately 1.5 km thick unit containing mainly black to grey shales with intercalations of siltstone, quartzite, and volcanics (Fig. 5). Lower sections are commonly pyritic, and the upper portion is known to contain coal seams and plant matter (Atherton and Sanderson, 1987). The formation is extensively exposed to the east of the range divide and is commonly observed as roof pendants in the high peaks of the Cordillera Blanca Mountains. While there is a sharp intrusive contact between the Chicama Formation and the Cordillera Blanca Batholith (CBB), deformation is commonly observed in the host rock adjacent to the intrusion, including a pronounced rodding that suggests the forcible intrusion of the batholith (Atherton and Sanderson, 1987; Petford and Atherton, 1992).

2.3.3 The Calipuy Formation.

The Calipuy Formation is a volcanic unit exposed extensively along the Western Cordillera of Northern Peru (Fig. 5). It is up to 2 km thick in some localities, unconformably overlying Mesozoic units. The bulk of the formation is andesite and pyroclastic flows with the exception of the dacitic/rhyolitic upper portion and a conglomerate bed that marks the base of the formation in some areas (Cobbing et al., 1981). The lower age limit for the formation is precisely dated to 52.5 Ma (Cobbing et al., 1981). The upper age limit of the volcanics is somewhat uncertain due to variable levels of erosion, but the youngest reported age from the unit is 14.6 Ma (Farrar and Noble, 1976; Cobbing et al., 1981). In the Cordillera Blanca region the Calipuy Formation can be observed in the Cordillera Negra Mountains, where it unconformably overlies the Coastal Batholith.

2.3.4 The Yungay Formation.

The 9 to 6 Ma ignimbrites of the Yungay Formation represent the latest known volcanism above the northern flat-slab subduction zone (Cobbing et al., 1981; Giovanni et al., 2010). These ignimbrites can be found exposed for ~60 km

within the Callejón de Huaylas Supradetachment Basin between Huaraz and Huayllanca (Figs. 2 and 5) displaying thicknesses of up to 950 m in some localities (Coldwell et al., 2011). The units are stratigraphically homogenous, contain abundant phenocrysts, and are poorly welded (Coldwell et al., 2011). Clasts of metasediments, granitoids, and ignimbrite are common. The Yungay Formation has a similar Sr, Na₂O, Y, and HREE signature to the CBB, prompting the interpretation of the Yungay Ignimbrites as the extrusive counterpart to the CBB (Atherton and Petford, 1993).

2.3.5 The Cordillera Blanca Batholith and Carhuish Stock.

The Cordillera Blanca Batholith (CBB) and Carhuish Stock are granitic to granodioritic intrusions comprising the core of the Cordillera Blanca Mountain Range (Figs. 2 and 5). Similarities in bulk chemistry, mineralogy, and emplacement age indicate that these intrusions are likely related (Cobbing et al., 1981). The major mineral composition includes: plagioclase, K-feldspar, quartz, amphibole, and biotite. Accessory minerals include: zircon, apatite, and magnetite. Zircon U-Pb ages for the batholith range from 8.2 to 5 Ma (Mukasa, 1984; McNulty et al., 1998; Giovanni, 2007), and a single age for the Carhuish Stock is 13.7 Ma (Mukasa, 1984; see section 2.5 for additional geochronological history). Emplacement pressure is estimated to be >2 kbar based on metamorphic mineral assemblages in the contact aureole, corresponding to a depths greater than ~6 km (Petford and Atherton, 1992). The melt source for the intrusion is interpreted to have been freshly underplated basaltic material, not subducted oceanic lithosphere (Petford and Atherton, 1996). High Sr and Na₂O, and low Y and HREE contents give the CBB a borderline trondhjemitic composition which supports production through partial melting of basaltic material at lower crustal conditions (Petford and Atherton, 1996; Atherton and Petford, 1993).

A penetrative foliation can be observed in the CBB, extending ~2.5 km eastwards into the batholith from its western extent (Petford and Atherton, 1992). This is associated with deformation along the CBDF, which delineates the western

boundary of the CBB (see below). Towards the core of the batholith weak foliations cut magmatic flow banding. Nearer to the western margin, mylonitic and brittle deformation become dominant, cutting the foliation (Fig. 6; Petford and Atherton, 1992).

2.3.6 Quaternary deposits.

Quaternary deposits are ubiquitous in the Cordillera Blanca Region, and include sediment derived from fluvial, colluvial, and glacial processes (Fig. 5). Glacial moraine deposits (Fig. 4) and postglacial lake and bog sediments are commonly found throughout the valleys of the Cordillera Blanca Mountain Range (e.g. Farber et al., 2005; Rodbell, 1993; Rodbell et al., 2008). Patches of glacial material can be found in isolated locations in the Cordillera Negra Mountains as well (Cobbing and Sanchez, 1996).

Landslide-fed talus cones are prevalent along the over-steepened glacial valley walls of the granitic CBB. Massive landslide deposits can also be observed in the Callejón de Huaylas basin, in places spanning its entire width. Fluvial sediment is sporadically preserved in fill terraces along the course of the Rio Santa, which is actively eroding and displacing the deposits of the Callejón de Huaylas. In places these terraces also preserve fine-grained lacustrine sediment, evidence for periodic damming of the valley, potentially due to episodic mass wasting events.

2.4 Extension in the Cordillera Blanca

The morphology of the Cordillera Blanca is dominated by a large, active, crustal scale extensional structure: the Cordillera Blanca Detachment Fault (CBDF; Figs. 2, 3 and 5). The fault sharply delineates the western boundary of both the Cordillera Blanca Mountains and the CBB, extending for over 100 km before dying out to the north and south. The CBDF has been active since at least 5.4 ± 0.1 Ma, and displacement has generated a significant amount of relief along its central and northern reaches, resulting in mylonitized fault surfaces (Figs. 3

and 6) along the range front that reach upwards of 2 km above the valley floor (Giovanni, 2007; Farber and Hancock, *in prep*). A normal sense of displacement has long been identified by researchers (e.g. Cobbing et al., 1981; Suarez et al., 1983; Schwartz, 1988), but McNulty and Farber (2002) were the first to identify it as a crustal-scale detachment structure.

The presence of this large extensional system in the high Andes is somewhat problematic. The trend of the structure is perpendicular to the primary axis of compression (Figs. 1 and 5), and appears to be an isolated phenomena sandwiched between the reverse-fault ridden Cordillera Huayhuash to the south and the Calipuy volcanic plains and Marañon Fold and Thrust Belt to the north. Several normal faults have been observed east of the Cordillera Blanca, although these do not appear to have accrued as much offset as the CBDF, and therefore have received much less attention in the literature (Doser, 1987; McNulty and Farber, 2002).

The mechanism driving the observed extension has not been agreed upon, and the list of proposed models continues to grow. The current spectrum of proposed mechanisms includes: 1) gravitational potential of the high topography exceeding rock strength and triggering topographic collapse (Suarez, 1983); 2) the development of a strike-slip pull-apart basin and transtensional tectonics (Petford and Atherton, 1992; McNulty et al., 1998); 3) differential crustal support due to a “sag” in the subducting oceanic plate (Gutcher, 1999); 4) interplate coupling between the subducting oceanic plate and the overriding continental crust (McNulty and Farber, 2002); and 5) the existence of an unmapped sub-vertical reverse fault at the front of the range (Gonzalez and Pfiffner, 2012). A general lack of subsurface data, with the exception of the subduction geometry described by Gutcher (1999), has hindered the exploration of the regional crustal dynamics.

As the CBDF is primarily responsible for the Neogene structural development of the region, it has also profoundly influenced the development of its hanging wall: the Callejón de Huaylas Supradetachment Basin (Figs. 2 and 7).

Giovanni et al. (2010) investigated the sedimentation history of the basin, identifying trends in depositional facies, stratal dip, and paleocurrent. Changes in depositional style, in conjunction with variable preservation of the Yungay Formation and trends in fault morphology, were interpreted to reflect the southward propagation of the tip of the CBDF past the study site, located ~15 km south of Huaraz (Fig. 2A), at 5.4 ± 0.1 Ma.

A common attribute of large normal faults is the presence of multiple segments that rupture and slip semi-autonomously (Schwartz, 1988; Machette et al., 1991; Densmore et al., 2003). These segments generally range in length from ~30 to 60 km, and are often delimited by preexisting structures and lithologic variations (Crone and Haller, 1991; DePolo et al., 1991). Schwartz (1988) proposed the presence of 4 to 5 segments within the CBDF on the basis of changes in fault geometry (Fig. 2B). Two segments were suggested south of Huaraz: the southern most extends ca. 35 km north from the southern fault tip to an eastward step in the main fault scarp, and the second extends some 45 km to the large salient near Huaraz. North of the salient the fault switches from a dispersed en echelon pattern to a single, well defined trace. Schwartz (1988) suggested the presence of 2 more boundaries north of Huaraz: one corresponding to a locale of high structural complexity near Huayllanca and a second to a small salient near Carhuaz, although this one was labeled as speculative.

Whether the CBDF system has effectively operated as a single segment that propagated north and southward or as multiple independent segments that eventually united is not entirely clear. The mylonitized escarpment that clearly marks the CBDF (Fig. 3) in the northern half of the range becomes discontinuous in the south, and variations in the fault pattern and the morphology of the supradetachment basin suggest that the fault system is behaving differently in different locations (Fig. 7). Fault-tip propagation is the primary mode of growth for individual normal-fault segments, but fault systems tend to grow by segment linkage (Crider, 2001). Schwartz (1988) identified 4 to 5 segments in the CBDF

based on range and fault geometry (Fig. 2B), so the potential for a complex growth history is high.

The fault is clearly active, as evidenced by offset Quaternary glacial and fluvial geomorphic features (Yonekura et al., 1979; Schwartz, 1988; Farber and Hancock, *In Prep*). Studies utilizing these offset features have determined the rate of dip-slip for multiple locations along the CBDF. Prior to the advent of cosmogenic radionuclide (CRN) surface exposure dating, reliable estimates of many geomorphic surfaces were elusive. Early studies on fault motion on the CBDF suffered from this imprecision, as can be seen by the range of rates estimated from one moraine in Querococha Valley: the reported slip rate decreased incrementally with each subsequent study, from 2.5 ± 0.5 mm yr⁻¹ to 1.11 ± 0.25 mm yr⁻¹ to 0.77 ± 0.1 mm yr⁻¹ (Yonekura, 1979; Schwartz, 1988; Farber and Hancock, *In Prep*). Farber and Hancock (*In Prep*) utilized ¹⁰Be exposure ages from preserved geomorphic features to quantify vertical slip rates for 4 locations along the CBDF, spanning ~2/3 of the >100 km long fault. These rates display a clear decreasing trend from 5.1 ± 0.8 to 0.59 ± 0.2 mm yr⁻¹ as they approach the southern fault tip, and correlate spatially with the changing distribution of structures associated with the CBDF and trends in range elevation, basinal relief, and basinal slope.

Reported kinematic indicators for the CBDF have produced some contradicting interpretations. While there is general agreement in the literature that the fault system is transtensional, the sense of horizontal displacement is still a matter of discussion. Microstructures described by Petford and Atherton (1992) had a predominantly dextral sense of motion, which fit lineations found in the mylonitized shear zone and rodding found in the metamorphic aureole near the contact with the Chicama Formation. McNulty et al. (1998) measured lineations, rotated clasts, and mica fish in the mylonitized shear zone, but reported a primarily sinistral sense of horizontal shear. The horizontal slip led both authors to interpret the extension as a strike-slip rift basin. McNulty et al. (1998)

compared the extension to the strain ellipse produced by sinistral shear due to oblique subduction, which is roughly compatible with the observed extension along the CBDF. Petford and Atherton (1992) invoked a Riedel shear model to describe the extension, noting the approximate correlations of regional structures and glacial valleys with predicted R_1 and R_2 fracture orientations. Clearly, the kinematics of the CBDF system require further attention.

2.5 Emplacement and Uplift of the Cordillera Blanca Batholith

The development of the Cordillera Blanca Mountain Range is intimately connected to both the CBB and the CBDF, as is evidenced by the batholith forming the core of the range (Fig. 5) and the role of the fault in the production of much of the relief along the western flank of the range (Fig. 3). The formation and uplift of the CBB has been investigated through a variety of approaches, including zircon U-Pb ages (Mukasa, 1984; McNulty et al, 1998; Giovanni, 2007), petrography and geochemistry (Petford and Atherton, 1992; Atherton and Petford, 1993), and thermochronology (Giletti and Day, 1968; Stewart, 1974; Cobbing et al, 1981; Montario, 2001; Giovanni, 2007).

The depth of emplacement of the CBB is constrained through a metamorphic mineral assemblage present in the contact aureole with the country rock. The presence of cordierite places a lower pressure limit of 2 kbar on the batholith, indicating an emplacement depth greater than ~6 km (Petford and Atherton, 1992). The crystallization age for the CBB and the adjacent Carhuish Stock to the south have been constrained through the use of zircon U-Pb dating from the granitoid bedrock. The two ages presented by Mukasa (1984) place the intrusion of the CBB at 6.3 Ma and the Carhuish Stock at 13.7 Ma, with no errors reported. This disparity in age has gone essentially unexplored by subsequent U-Pb studies, which have focused solely on the CBB. Later studies produce largely consistent ages for the CBB: McNulty et al. (1998) present a single age of 8.2 ± 0.2 Ma; and Giovanni (2007) produced 10 ages, 9 of which fall between 8.0 ± 0.7

and 5.3 ± 0.3 Ma (the 10th sample was an apparent outlier with an age of 23.1 ± 0.4 Ma). Thus, the emplacement age of the CBB is constrained to between 8.2 ± 0.2 and 5.3 ± 0.3 Ma, and the range of ages is consistent with petrologic observations suggesting the episodic emplacement of nested, upwards-younging ‘nappes’ (Atherton and Sanderson, 1987). Considering the ~5 to 8 Ma difference in U-Pb ages between the two intrusions, the emplacement of the Carhuish Stock can be treated as a separate, earlier event.

A suite of thermochronologic data has been previously collected from both the CBB and Carhuish stock, including K-Ar, $^{40}\text{Ar}/^{39}\text{Ar}$, and apatite fission track (AFT) and (U-Th)/He (AHe) analyses. Interestingly, biotite K-Ar analyses do not display the same disparity as the U-Pb ages. Biotite ages from the CBB range from 12.0 to 2.7 ± 0.4 Ma and ages from the Carhuish Stock range from 10.1 ± 0.2 to 9.1 ± 0.4 (Giletti and Day, 1968; Stewart et al., 1974; Cobbing et al., 1981). Hornblende K-Ar ages from the Carhuish Stock range from 16.5 ± 0.5 to 11.3 ± 0.6 Ma (Cobbing et al., 1981) and muscovite K-Ar ages from the CBB range from 6.3 ± 0.2 to 3.6 ± 0.3 Ma (Stewart et al., 1974; Cobbing et al., 1981).

Giovanni (2007) reports 24 $^{40}\text{Ar}/^{39}\text{Ar}$ ages from biotites, muscovites, and potassium feldspars spanning much of the length of the CBB. Four valleys lining the western Cordillera Blanca were targeted, listed here from north to south along the range: Yanac, Pachma Alta, Llanganuco, and Honda (Fig. 2A). Biotite ages span from 6.8 ± 0.1 to 4.1 ± 0.1 Ma, muscovite ages range from 7.3 ± 0.2 to 4.5 ± 0.5 Ma, and potassium feldspar ages range from 5.2 ± 0.1 to 4.0 ± 0.1 Ma. pseudo-vertical transects of biotite ages from Giovanni (2007) in Yanac, Llanganuco, and Honda Valleys, produce apparent exhumation rates of 0.18, 0.54, and 0.19 mm yr^{-1} , respectively, corresponding to the ~7 to 4 Ma time window.

AFT and AHe dating from sites along the CBB give insight into the later cooling history and uplift of the range (Montario, 2001; Giovanni, 2007). AFT ages from a collection of sites between Llanganuco and the southern tip of the CBDF record the time since cooling past $\sim 180^\circ\text{C}$, and range from 4.2 ± 5.5 to 1.8

± 0.8 Ma (Montario, 2001). A pseudo-vertical AFT transect along Llanganuco Valley yields an apparent exhumation rate of 0.56 mm yr^{-1} between 2.9 ± 0.9 and 2.3 ± 1.2 Ma. AHe dating records time since cooling past the $\sim 60^\circ\text{C}$ isotherm. AHe ages from samples collected from Llanganuco Valley range from 4.2 ± 0.9 to 2.0 ± 0.1 Ma, and yield an apparent exhumation rate of 0.47 m yr^{-1} (Giovanni, 2007)

Exhumation rates can be used to represent bulk rock uplift if surface elevations are assumed to be constant (e.g. Molnar and England, 1990; Reiners and Brandon, 2006). In this context, exhumation rates from the Cordillera Blanca can be used to interpret spatial and temporal patterns of rock uplift for the CBB. The assumption of constant surface elevation is probably not accurate in most settings, but relative variation in exhumation can be informative even if it is not entirely quantitative. Exhumation rates from Llanganuco Valley are fairly constant across all proxies for cooling history: 0.47 mm yr^{-1} (AHe), 0.56 mm yr^{-1} (AFT), and 0.54 mm yr^{-1} (biotite $^{40}\text{Ar}/^{39}\text{Ar}$). This suggests constant uplift rates in the Llanganuco region between 6.2 ± 0.2 and 2.0 ± 0.1 Ma. Biotite $^{40}\text{Ar}/^{39}\text{Ar}$ transects from other valleys return lower exhumation rates, between 0.18 and 0.20 mm yr^{-1} , revealing slower uplift relative to Llanganuco, at least between ~ 7 to 4 Ma. These exhumation rates provide an outline of the uplift history for the Cordillera Blanca, but a robust interpretation is hindered by a lack of data from outside of Llanganuco Valley. New data presented in this work adds a new transect of zircon (U-Th)/He (ZHe) and AHe ages, adding spatial and temporal breadth to the current data set.

3 Methods

This study draws upon a variety of methods to characterize the erosional and exhumational history of the CBB as well as its modern topography and morphology. CRN basin-averaged erosion rates and surface exposure ages are used to quantify surface denudation over time scales of $\sim 10^3$ to 10^6 yrs (Bierman

and Nichols, 2004). AHe and ZHe thermochronology give insight into longer-term ($\sim 10^6$ to 10^7 yrs) exhumation rates from previously unstudied portions of the mountain range. Trends in range morphology and topography are investigated through field mapping and the manipulation of digital elevation models (DEMs) in a geographic information system (GIS).

3.1 Cosmogenic Radionuclides

In situ CRN based analyses have become a common method for addressing a wide range of surficial processes including: erosion and surface preservation (e.g. Brown et al., 1995; Safran et al., 2005; Abbuhl et al., 2010; Valla et al., 2010), recreating paleo-glacial chronologies (e.g. Farber et al., 2005; Smith et al., 2005; Hall et al., 2009), and quantifying regional uplift and deformation patterns (e.g. Zehfuss et al., 2001; Stock et al., 2005; Hall et al., 2008; Dortz et al., 2009; Saillard et al., 2011). Erosion rates are sensitive to variations in climate patterns (e.g. Abbuhl et al., 2010; Delunel et al., 2010), tectonic activity (e.g. Whittmann et al., 2007; Insel et al., 2010), as well as lithology (e.g. Gosse and Phillips, 2001; Abbuhl et al., 2011). For this reason, spatial patterns in erosion rates can lend valuable insight into the efficacy of climatic denudation and tectonic deformation in a given region. I use the *in situ* production of ^{10}Be to measure basin scale erosion rates and river incision rates in order to investigate these processes in the Cordillera Blanca and surrounding regions.

3.1.1 CRN production.

The galactic cosmic ray flux, and to some degree the solar energy flux, is the source of energy responsible for production of all CRNs. This energy produces a series of reactions with the atoms of the earth's upper atmosphere, resulting in a shower of energized particles (termed the "secondary cosmic ray flux"; Fig. 8A). These particles interact with target atoms in minerals exposed at the surface of the earth, producing CRNs (Fig. 8B; Gosse and Phillips, 2001). Six

CRNs receive more frequent attention: ^{14}C , ^{10}Be , ^{26}Al , ^{36}Cl , ^3He , and ^{21}Ne . Each has its own advantages and disadvantages, which are outlined by Gosse and Phillips (2001). The primary differences lie in the stability/radioactivity of the nuclide, although differences in target elements and minerals, diffusivity through solids, and the fundamental understanding of the nuclide's properties lends them to different applications. In this study, I will be using the CRN ^{10}Be since it forms in quartz-bearing rock, has a long half-life (~1.4 Ma; Chmeleff et al., 2010), is well characterized and has a well-developed protocol for isolation and measurement (Kohl and Nishiizumi, 1992).

The secondary cosmic ray flux is not uniform across the surface of the earth. Spatial variances in the amount of energy reaching the surface are produced due interactions with the earth's magnetic field and mass encountered along a particle's trajectory towards its target element (i.e. the atmosphere, rock and overburden, water and ice). The effects of these interactions must be modeled in order to determine the site-specific production rate of the studied CRN at the sampling location.

3.1.1.1 The geomagnetic field.

Charged particles comprise the primary component of the galactic cosmic ray flux (Gosse and Phillips, 2001). For this reason, particle trajectories are highly affected by the earth's magnetic field. The Earth's magnetic field is oriented such that contours of equal magnetic strength are parallel to the surface of the earth near the equator and perpendicular to the surface of the earth near the poles (Fig. 8C). Particle trajectories are deflected along these contours in proportion to the charge of the particle and inversely proportional to the particle's momentum (Gosse and Phillips, 2001). As the incoming particle trajectory is predominantly perpendicular to the surface of the earth, the magnetic field is more effective at diverting them near the equator than it is near the poles. The result is a variation in the galactic (and therefore the secondary) cosmic ray flux that is

highly dependent on latitude. Rates of CRN production are lowest at low latitudes and increase north and south towards the earth's poles.

The strength of the earth's magnetic field is not constant over geologic time (e.g. Balco et al., 2008), and therefore the CRN production rate must vary as well. The most widely employed model for CRN production, originally presented by Lal (1991) and later updated by Stone (2000), does not account for these variations, but owes its appeal to its excellent fit to calibration data sets (Balco et al., 2008), and in the case of the Cordillera Blanca, produces the best fit to the nearest production calibration site: the Breque Moraine (Farber et al., 2005). Other scaling schemes address the time dependency of production rate by varying the energy required for a particle to penetrate the magnetic field (termed the cut-off rigidity; Dunai, 2001; Desilets, 2006; Lifton, 2005) and in some cases adjusting the power of the solar wind (Lifton, 2005). Balco et al. (2008) presented a time dependent scaling scheme based on the Lal (1991)/Stone (2000) model that includes simple paleomagnetic correction based on the work of Nishiizumi (1989). It is worth noting that even though the magnetic field of the earth is known to fluctuate over time, the details regarding these fluctuations are poorly understood, and in most cases, exposure ages and erosion rates calculated using these different methods do not differ by more than 5 to 20%.

3.1.1.2 Attenuation through interaction with matter.

A particle capable of penetrating the geomagnetic field will interact with matter in the atmosphere and on the surface of the earth. The cosmic ray flux is attenuated at a rate proportional to the density of the matter it passes through. Elevation has a strong effect since higher elevations require the flux to pass through a shorter amount of atmosphere, resulting in a higher flux at the earth's surface and a faster production rate. The original scaling scheme of Lal (1991) uses the sample's elevation to correct for this effect. Stone (2000) recast the elevation dependence into air pressure, which allowed for corrections based on global variations in atmospheric pressure. Air pressure and elevation relationships

for the Cordillera Blanca Region are described in Farber et al. (2005), and this relationship is used in all CRN calculations for this study.

Rock is much denser than air, and thus attenuates the cosmic ray flux much more quickly. This is reflected in the penetration depth of the cosmic ray flux into rock at the surface of the earth, which is on the order of a few meters (Gosse and Phillips, 2001). Since rock attenuated the flux so efficiently, elevated topography surrounding a sample location will shield the sample from a portion of the cosmic ray flux, lowering the site-specific production rate. In the case of bedrock samples, this shielding effect is corrected using measurements taken during sample collection. In the case of basin-averaged erosion rate samples, the shielding effect is calculated for points across the entire contributing catchment with the aid of GIS software and a DEM. For samples taken from below the surface, an added correction must be made for the mass of overlying material. In this study, all samples were either collected from the surface of the earth directly (exposure ages) or were assumed to be representative of surface material (erosion rates), eliminating the need for the depth correction. Additional considerations must be made for samples with more complicated shielding histories such as seasonal snow cover or multiple episodes of burial and exposure.

3.1.2 Sample collection.

3.1.2.1 *Incision rate samples.*

Exposure age samples used to calculate rates of river incision were collected from two locations: 1) from the Coastal Batholith along the Rio Santa's northern reach (Fig. 9), and 2) from the CBB where a westerly-draining tributary to the Rio Santa crosses the CBDF (Figs. 9 and 10). In each location, a smooth, fluvially polished bedrock wall was sampled with an approximate vertical spacing of 3 meters between samples (Fig. 10A). A constant, assumed error in measured elevations of ± 0.2 m was used for all samples. This practice ensures minimal effects due to erosion of the surface after incision (Gosse and Phillips, 2001) and allows for calculation of an incision rate via the vertical distribution of exposure

ages. Acceptable sample sites can be rare, and exposure age transects were collected at available opportunities.

The rate at which a river incises down through its bedrock substrate is sensitive to changes in relative fluvial base level and stream power (e.g. Finnegan et al., 2005; Whipple, 2004), which can be produced through processes such as surface uplift and subsidence, changes in sea level, or changes in regional climate patterns. In this context, I seek to address the tectonically driven uplift of the landscape in the Cordillera Blanca Region, where variations in precipitation and climate are minor (Fig. 2C). Samples collected from the Coastal Batholith are predicted to reflect regional uplift and samples collected from the CBB should reflect uplift and base level change across the CBDF.

3.1.2.2 Basin-averaged erosion rate samples.

Samples used for calculating basin-averaged erosion rates were collected from basins throughout the Rio Santa drainage as well as basins to the east and north of the Cordillera Blanca (Fig. 9A). Morphometric data was collected for all associated basins as well (Fig. 9B). At least 2 kg of fine- to medium-grained sand was collected from the active river channel (Fig. 11). A set of samples were collected from basins in the Cordillera Blanca mountain range just upstream of where the tributary crosses the main strand of the CBDF. By sampling a collection of fault-bounded basins from along the length Cordillera Blanca Mountain Range, I am able to test for spatial variations in erosion rate driven through variability in fault dynamics and along-strike trends in climate and glaciation. The erosion rates only represent the footwall of the fault, which is undergoing active uplift relative to the supradetachment basin below.

In the case of drainage systems undergoing continuous erosion, a sample of sand collected from an active stream channel can be taken as a representative collection of material from the entire upstream area (Brown et al., 1995; von Blanckenburg, 2005). This method assumes equal input from all areas in the catchment and negligible sediment transport time. These assumptions are not

always valid, and the nature of sediment production and transport in glacial valleys, such as those of the Cordillera Blanca, produces some potential problems. Landsliding and sediment storage, in particular, can be issues in glacially sculpted landscapes since the over-steepened valley walls are prone to gravitational collapse and glacio-fluvial systems can be severely transport limited with multiple lakes and bogs along the valley floor.

Investigations into the effects of landsliding on CRN basin-averaged erosion rates suggest larger basins with shallow landslides are preferable (Niemi et al., 2005; Yanites et al., 2009). Many of the basins of interest to this study are limited in size by the CBDF to the west and the range crest to the east. In some instances I was forced to collect samples from smaller basins, potentially generating error in the inferred erosion rates. To further combat this potential error, all sampling sites were chosen so as to maximize the distance from any talus cones encroaching on the active channel, thereby limiting the potential for direct contamination with landslide-sourced material. Whitmann and Blanckenburg (2009) showed that sediment transport and storage in fluvial systems results in neither further irradiation nor significant decay.

Anthropogenic activity can also effect measured erosion rates, and in the case of the Cordillera Blanca, active road work, unconfined mine tailings and hydroelectric dams are all potential sources of error. Samples were collected away from sources of anthropogenic alteration to landscapes whenever possible in order to minimize their effects.

3.1.3 Sample preparation and analysis.

All ^{10}Be samples for this study were prepared either at McGill University or the University of California, Santa Cruz following a procedure modified from that of Kohl and Nishiizumi (1992). All samples were crushed and/or sieved to a diameter between 250 and 500 μm . In the case of the sand samples, if enough grains were within the 250 to 500 μm size fraction (500 to 800 g) no grinding was performed. If additional material was needed, grains from the 500 to 1000 μm

and 1 to 2 mm size fractions were sequentially ground until ~500 g of material in the 250 to 500 μm size fraction was recovered (Table 3). Ground and sieved material was then subjected to a 12-hour leach in a solution of heated 5% nitric acid in order to remove any carbonate present in the sample.

Cleaned, fine-grained sand underwent a 2-stage mineral separation procedure to isolate quartz grains. First, magnetic susceptibility separation was performed using a Frantz Isodynamic Separator to remove paramagnetic minerals. Separations were commonly run under currents ranging from 0.5 to 1 Ampere. Second, a density separation was performed using a lithium polytungstate liquid to differentiate feldspar grains from quartz grains.

Quartz separates were then cleaned and etched. Samples underwent a series of rinses in a 2% hydrofluoric acid (HF) and 1% nitric acid (HNO_3) solution in a sonic bath under elevated temperature for a period of 2 to 3 days per rinse. Rinses were repeated at least 3 times or until all non-quartz material and meteoric ^{10}Be was assumed to have been removed.

To isolate the ^{10}Be , purified quartz was dissolved into a solution of 50% HF and 1N HNO_3 and then spiked with ^9Be . Dissolved samples were then fumed with perchloric acid and run through anion and cation liquid chromatography columns to isolate the Be. Isolated Be was then precipitated as BeO , blended with Nb powder, and loaded into steel targets for measurement on the accelerator mass spectrometer located at Lawrence Livermore National Laboratory in California. Measured ratios were normalized to standard 07KNSTD3110, and ^{10}Be concentrations were calculated using the known mass of ^9Be added in the spike.

3.1.4 Calculating a surface exposure age.

CRNs accumulate in rock in relation to exposure time. In the case of radiogenic CRNs, this relationship is described by (Eq. 1):

$$(1) \quad N = \left(e^{-\lambda t} \right) \left(\frac{P}{\lambda + \epsilon} \right) \left(1 - e^{-t(\lambda + \epsilon)} \right)$$

Where N is the nuclide concentration (atoms g^{-1}), x is the sample burial depth (cm), ρ is the rock density (g cm^{-3}), Λ is the e-folding attenuation path length (g cm^{-2}), P is the site-specific production rate (atoms $\text{g}^{-1} \text{yr}^{-1}$), ε is the erosion rate (cm yr^{-1}), λ is the radioactive decay constant (yr^{-1}), and t is surface exposure time (years; *Gosse and Phillips, 2001*). Common values for ρ and Λ are $\sim 2.7 \text{ g cm}^{-3}$ and 160 g cm^{-2} , respectively (*Gosse and Phillips, 2001; Balco et al., 2008*). The decay constant for ^{10}Be is $4.62 \times 10^{-7} \text{ yr}^{-1}$ (*Balco et al., 2008*).

Since equation 1 contains two variables (t and ε), it is impossible to solve for an exposure age or erosion rate. It can, however, be simplified using two end member assumptions: 1) no erosion of the surface has occurred since exposure began, and 2) erosion has been constant and ongoing for long time scales relative to the erosion time scale. Because all samples in this study are surface samples, the conditions of the first scenario allows equation 1 to be reduced to (Eq. 2):

$$(2) \quad N = \left(\frac{P}{\lambda} \right) (1 - e^{-t(\rho\Lambda^{-1} + \lambda)})$$

and for the second scenario (Eq. 3):

$$(3) \quad N = \left(\frac{P}{\rho\varepsilon\Lambda^{-1} + \lambda} \right)$$

The resultant values represent the minimum exposure age and maximum erosion rate for the sampled surface. Virtually all surfaces will fall somewhere between these two end members, although careful sampling of surfaces with signs of good preservation can help reduce the error involved in estimating a surface exposure age (*Gosse and Phillips, 2001*).

3.1.5 Calculating an erosion rate.

Calculation of a basin-averaged erosion rate from a sample of fluvial sand can be readily performed using equation 3 as long as several assumptions are made regarding the sample's history (*von Blanckenburg, 2005*). As described above, equation 3 requires that the sample originates at the surface and that the surface has been in an erosive steadily steady state for a relatively long period of time. This time can be calculated by dividing the rock density by the product of

the attenuation length and calculated erosion rate (Eq. 4; e.g. von Blanckenburg, 2005):

$$(4) \quad t_e = \left(\frac{\rho}{\lambda} \right) \varepsilon^{-1}$$

where t_e is the erosion timescale, or the time required to erode one e-folding attenuation length of rock. This method assumes a short transport history for the sample, where the sand has not been exposed in the active channel long enough to be significantly dosed after erosion. Similarly, the sample cannot have become temporarily buried for long enough to allow significant radioactive decay. As the calculated erosion rate is interpreted as an average for the whole basin, it is assumed to be a representative sample of all parts of the drainage system. In situations where multiple lithologies are exposed in a basin and are contributing to a sample, it can be necessary to account for different quartz concentrations in the different units. Safran et al. (2005) addressed this issue by weighting the regions of different lithology by their relative quartz content. These assumptions are discussed in further detail below.

3.2 Apatite and Zircon U-Th/He Thermochronology

AHe and ZHe thermochronology are powerful tools for unraveling spatial and temporal patterns of long-term landscape evolution (e.g. Reiners and Brandon, 2006; Barnes et al., 2006; Garver et al., 2005; Berger et al., 2008). In the Cordillera Blanca, a body of prior work has provided a small suite of thermochronologic data from portions of the CBB (Cobbing et al., 1981; Montario, 2001; Giovanni, 2007). The Carhuish Stock, which is exposed some ~10 km south of the CBB's southernmost exposure, has been less studied with ages only from zircon U-Pb (Mukasa, 1981) and K-Ar (Cobbing et al., 1981). The CBDF is clearly active in this region, so the cooling and exhumation history of the Carhuish Stock will give insight into the fault's evolution along its southern reach. I present a new transect of AHe and ZHe ages collected from the Carhuish

Stock, helping to constrain the thermal dynamics of the system as it cooled past the closure temperatures for the ZHe and AHe thermochronometers.

The radioactive decay of ^{238}U , ^{235}U , ^{232}Th , and ^{147}Sm results in the production of ^4He , which can be retained in a host mineral's crystal lattice. A mineral's ability to retain and accumulate the daughter isotope is primarily dependent on its temperature, although other factors, such as excessive radiation damage (e.g. Garver et al., 2005), can modify its retention properties. The temperature at which ^4He begins to be retained is more accurately described as a temperature range, termed the partial retention zone (PRZ), in which the daughter isotope is partially, but not entirely held within the crystal lattice. The PRZ can be modeled to produce the effective closure temperature for that mineral, but this value is highly dependent on cooling rate. For zircon and apatite, effective closure temperatures for a cooling rate of $\sim 10^\circ\text{C yr}^{-1}$ are approximately 180°C and 60°C , respectively (Reiners and Brandon, 2006).

Thermochronologic cooling ages are often converted into exhumation rates, which can be extremely useful for investigating landscape evolution over timescales relevant to many tectonic and orogenic processes. Exhumation rates can be determined in a variety of ways. A common method is to use a model of the geothermal gradient to pin the mineral at a given depth using its closure temperature (e.g. Safran et al., 2006). Accurate use of this method, however, requires detailed knowledge of the geothermal gradient, which is not always available. Another method involves the use of a vertical transect of cooling ages. The slope of the line of best fit for the age-elevation relationship (AER) of a collection of cooling ages is equivalent to the vertical exhumation rate during the time bounded by the sample's ages (e.g. Braun, 2002).

AERs are particularly useful because they do not rely on a precise linear geothermal gradient to determine the exhumation rate. They are, however, sensitive to deflections of the geothermal gradient due to topography. This effect is most prominent near the surface, and can alter AERs from lower temperature

thermochronometers (Braun, 2002). Specifically, AERs from low temperature thermochronometers will tend to overestimate exhumation rates, and can even produce negative values in situations involving relief reduction. Conversely, in situations with extremely large amounts of relief production, the AER from a low temperature thermochronometer will underestimate the exhumation rate (Braun, 2002). The amount to which they will be affected depends on a variety of factors including: wavelength of topography, the geothermal gradient, exhumation rates, and changes in topographic relief.

I use the AER method to calculate exhumation rates in the Carhuish Stock. This method was chosen for 4 reasons: 1) no detailed information on the geothermal gradient in the Cordillera Blanca region is available, 2) the thermal history of the Cordillera Blanca is probably complex due to a combination of magmatic heating and refrigeration due to flat-slab subduction (e.g. Dumitru et al., 1991), 3) transects from the CBB (Montario, 2001; Giovanni, 2007) allow me to directly compare exhumation rates derived from similar methods, and 4) the topographic wavelength in the Cordillera Blanca is ~8 to 15 km, and topographic wavelengths <10 km do not substantially alter AERs from low temperature thermochronometers (Braun, 2002).

Samples collected for this study and by previous workers (e.g. Montario, 2001; Giovanni, 2007) are not from true vertical profiles, and are partially distributed along the length of valleys. As a result, cooling ages will reflect both the vertical and horizontal exhumation histories of the valley. Precise determinations of AER exhumation rates require consideration of the horizontal sample distribution as well as the topographic effects discussed above. As such, all exhumation rates presented and discussed herein should be deemed approximate.

3.2.1 Sample Collection.

Samples were collected from solid granitic bedrock outcrops along a vertical transect across the Carhuish Stock (Figs. 2A, 5, and 9A). Outcrops with

signs of extensive chemical weathering were either avoided or the outer portion was removed and fresh rock was sampled. A vertical distance of ~250 m was targeted between sample locations, although this was not always possible due to accessibility and the height of the ridge crest. In total, samples were taken from three localities spanning from the first and lowest exposure to near the ridge crest, just below the contact with the overlying Chicama Fm. Both zircon and apatite grains were recovered from each sample.

3.2.2 Sample Preparation and Analysis.

All samples were prepared and analyzed at McGill University and The University of California, Santa Cruz. Rock samples were crushed to grain sizes of <250 μm , and the pulverized samples were leached in a solution of 5% nitric acid at elevated temperature for >12 hrs to remove any carbonate. A Frantz Isodynamic separator was run iteratively at increasing currents ranging from ~0.5 to 1.5 Amperes to remove paramagnetic minerals. Resulting material was subjected to a density separation using a lithium polytungstate fluid, which allowed recovery of relatively dense zircon and apatite grains. Individual grains were hand picked under a binocular microscope, their dimensions were measured and they were then wrapped in niobium foil. Grains were then placed under a Nd-YAG laser and ^4He was out-gassed at temperatures of ~1350°C. Evolved helium was mixed with a spike of ^3He , condensed cryogenically, and run on a quadrupole mass spectrometer to measure the $^4\text{He}/^3\text{He}$ ratio. Degassed grains were then dissolved and spiked with known quantities of ^{233}U and ^{229}Th and analyzed for U and Th ratios on an ICP-MS.

3.3 Mapping and Remote Sensing

Mapping was aided with the use of Advanced Spaceborne Thermal Emission and Reflectance Radiometer (ASTER) imagery and 30 m DEMs (USGS and Japan ASTER Program, 2003), and Shuttle Radar Topography Mission (SRTM) 90 m DEMs (USGS, 2006). Handheld geographic positioning system

(GPS) receivers (horizontal accuracy of ~5 m) recorded sampling sites and the locations of major geologic and geomorphic features. Field measurements of topographic shielding for calculation of CRN production rates were performed using a Brunton Geotransit, with a measurement error of 1 degree.

Remote sensing-based topographic analyses mainly utilized the ESRI ArcDesktop GIS and the tools included therein to manipulate SRTM DEMs (USGS, 2006). DEM files were mosaiced and filtered for anomalous gaps within the dataset. Catchment extents and river profiles were extracted using the tools in the ArcGIS Hydrology Toolbox and these features defined the boundaries for basin statistics. Zonal and Neighborhood Statistics, were used for local relief calculations and swath profile generation, respectively.

4 Results

4.1 Remote Sensing

4.1.1 Basin morphology.

Using DEMs, I extracted the morphometry of 2 groups of drainage basins: 1) those that drain the western flank of the Cordillera Blanca Mountain Range (Table 1 and 2) those corresponding to basins used for ^{10}Be basin-averaged erosion rate analysis (Table 2; Fig. 9). Values for basin elevation (max, min, mean, mode, total relief) come from the 90m resolution SRTM DEMs, and slope maps generated from the SRTM DEMs allowed quantification of the slope of valley walls (max, min, mean). I determined local relief for each pixel on the SRTM DEMs within radii of 1 and 3 km, and the maximum local relief in each basin is reported for both radii. Radii for local relief measurements were chosen based on values used in previous studies (e.g. Montgomery and Brandon, 2002), and the observation that radii larger than 3 km begin to produce similar results. A 1 km radius was used to identify smaller-scale relief patterns that would be smoothed by a larger window. Basins along the western flank of the Cordillera

Blanca were limited to the area above the trace of the CBDF, which delineates the western edge of the CBB, restricting the analysis to the footwall of the fault.

North-south variations along the strike of the range are evident in many of the morphometric indices (Fig. 12). Peak basin elevations reach a maximum of 6733 m a.s.l. near Mt. Huascarán and steadily decrease to the north and south to elevations of ~5250 and 5500 m a.s.l., respectively (Fig. 12A). Minimum basin elevations decrease from south to north from ~4300 to 1500 m a.s.l., but it should be noted that the lowest point in each basin was selected as being the approximate location of the CBDF, and as such this decrease represents a northward decline in the elevation of the main strand of the CBDF. Mean basin elevations remain between ~4500 and 4700 m a.s.l. along the length of the range. Modal basin elevations display much more scatter than mean basin elevations, on the order of 1000 m over distances of 10 km. Calculation of a 3 point running average reveals the general trend of the data set: a slight decrease in modal basin elevations towards the north from ~4800 to 4500 m.

All 3 measures of relief (total basin relief, 1 km radius local relief, and 3 km radius local relief) display a similar trend of decreasing towards the south (Fig. 12B). The values produced by the 3 methods are quite different, as are the magnitudes of along-strike change. Total basin relief ranges from ~1000 to 4000 m along strike, 3 km radius local relief ranges from ~1000 to 3250 m, and 1 km radius local relief ranges from ~800 to 1900 m. All 3 measures display a prominent “notch” in the data at ~90 km south of the northern fault tip, coincident with the large salient in the mountain front near the city Huaraz. South of this point, basins begin to display lower values for all 3 measures of relief.

Both maximum and mean values for valley slope decrease towards the southern end of the range (Fig. 12C). Mean slope shows relatively little scatter, decreasing from ~30° in the north to ~22° in the south. Maximum slope decreases from ~65 to 70° in the north to 45 to 55° in the south. Scatter in maximum slope values increases sharply at ~90 km south of the northern fault tip,

similar to that described in relief data above. Another locus of higher scatter occurs between ~20 and 40 km south of the north fault tip. Minimum valley slopes range from 0 to ~10°, although no along-strike trends are observable.

4.1.2 Swath profiles.

A ~255 km long, range-parallel swath profile of the Cordillera Blanca Mountain Range, oriented at 155° (B to B'; Fig. 9B), reveal patterns in range elevation (maximum, mean, minimum; Fig. 13A), slope (maximum, mean, minimum; Fig. 13B), and relief (1 km radius local relief, 3 km radius local relief; Figs. 13C and 13D). These analyses integrate data from both sides of the range, thereby reflecting larger scale trends in range morphology. Each data point represents a 90 km long by 1 km wide swath oriented perpendicular to the strike of the range, reaching approximately from the Rio Santa to the Rio Marañon (Fig. 9B).

Maximum elevations occur around Huascarán, and decrease to the north and south. Peaks near 235 km along strike represent part of another mountain range, the Cordillera Huayhuash, located to the south of the Cordillera Blanca Mountain Range (Fig. 2A). Mean elevations decrease towards the north from ~4500 m a.s.l. near Querrococha Valley to ~3100 m a.s.l. near where the Rio Santa curves westward towards the Pacific Ocean. Minimum elevations reach a maximum near Querrococha Valley and decrease to the north and south.

Both 1 km and 3 km radius local relief follow similar trends, although there are clear differences in the magnitude of relief and the wavelength sampled between the 2 methods. Maximum, mean and minimum reliefs for both radii reach a low at Querrococha Valley and increase to the north and south. Results from the 1 km radius seem to be more sensitive to smaller scale variations, especially in maximum relief. The 3 km radius seems to differentiate localities of increased relief that are not observed in the 1 km relief profile, particularly the locality surrounding Mt. Huascarán.

Slope also reaches a low near Querrococha and increases to the north and south. Mean slopes range from $\sim 15^\circ$ to 25° , and maximum slopes range from ca. 45° to $>70^\circ$. Maximum slope values are much less consistent than mean slope, varying by as much as 20° over distances of 10 km. The calculation of a running average through the maximum slope data exposes an overall shift of $\sim 10^\circ$, similar to that observed in mean slope data.

4.2 ^{10}Be Basin-averaged Erosion Rates

The 21 new ^{10}Be basin-averaged erosion rates presented in this study (Tables 3 and 4) describe patterns of erosion covering portions of the Rio Santa watershed and the Rio Marañon watershed. Using the time-variant Lal (1991)/Stone (2000) scaling scheme described in Balco et al. (2008), erosion rates range from 0.015 ± 0.001 to $4.6 \pm 0.4 \text{ mm yr}^{-1}$ with external uncertainties on the order of 7 to 10%. The comparison of results from different scaling schemes shows that their effect is relatively negligible and is generally within the external error of the data (Fig. 14), and the grain size of material used did not have any observable effects (Table 3). The calibration of Lal (1991)/Stone (2000) yields the best fit to the nearest calibration site: the Breque Moraine (Farber et al., 2005). Thus, all ^{10}Be erosion rates and exposure ages discussed in this text will be calculated using this scaling scheme.

Thirteen erosion rates were collected from the western flank of the Cordillera Blanca Mountain Range (Fig. 9A). All of these basins, with the exception of Yanac Valley (sample RS11-BE03) in the north, are in the granitoids of the CBB or Carhuish Stock, which generally possess classic U-shaped glacial valleys formed from repeated glaciations dating to at least 400 ka (Farber et al., 2005). The mainly granitoid basins have areas ranging from 15 to 144 km^2 and mean slopes between 24° and 31° . As compared to the other basins, Yanac Valley has a more fluvial morphology, covers a larger area (515 km^2), has a mean slope of 23° , and is predominantly situated in the metasediments of the Chicama Fm.

^{10}Be erosion rates from basins in the western Cordillera Blanca range from 0.015 to 4.6 mm yr⁻¹. A sample collected from the Rio Santa (RS07-R2) yields a ^{10}Be erosion rate of 0.084 ± 0.007 mm yr⁻¹, integrating tributary drainages from both the glacial Cordillera Blanca and the dry, unglaciated Cordillera Negra Mountain Ranges over an area of 5,752 km².

East of the drainage divide, ^{10}Be erosion rates from 3 samples span a much tighter range from 0.094 ± 0.007 to 0.12 ± 0.009 mm yr⁻¹ (Figs. 9B and 15). With the exception of small granitoid areas near the drainage divide, all 3 basins are in metasedimentary rock and exhibit highly fluvial morphologies. Basin areas span a large range of 57 to 14,058 km², but mean slopes are essentially invariant (20 to 21°). Included in these is a sample from the Rio Marañon (RM07-R1), which drains the eastern flank of the Cordillera Blanca and yields an erosion rate of 0.10 ± 0.008 mm yr⁻¹.

Northwest of the Cordillera Blanca, the Rio Chuquicara drainage system forms a large tributary to the Rio Santa (Fig. 9). One sample (RC07-R1), taken from approximately 10 km upstream from the confluence with the Rio Santa, yields a ^{10}Be erosion rate of 0.054 ± 0.004 mm yr⁻¹. Erosion rates from the upper reaches of the drainage include 2 smaller basins with erosion rates of 0.077 ± 0.006 and 0.044 ± 0.004 mm yr⁻¹ and one sample collected below their confluence that yields an erosion rate of 0.086 ± 0.007 mm yr⁻¹. These basins lie in a mixture of metasedimentary and volcanic rocks, with some granitoids present at high elevations. Valley morphologies are predominantly fluvial and mean slopes fall between 19 and 22°.

4.3 ^{10}Be Exposure Ages

Vertical transects were collected from 2 fluvially polished bedrock cliffs (Fig. 9A and 10). One transect, located along the northern reach of the Rio Santa, was taken from the granitoids of the Coastal Batholith (RS07-I). The second transect was located in the northern CBB, just upriver from the main strand of the

CBDF (RS11-IA). All reported errors account for inaccuracies due to measurements during sample collection, preparation and analysis and are calculated as the square root of the sum of the squares of all absolute errors.

Three ^{10}Be exposure ages were calculated from the Rio Santa transect in the Coastal Batholith, spanning ~ 9000 yrs (Table 5). Listed by vertical position, from highest to lowest, they are: $11,916 \pm 1150$ yrs, $5,907 \pm 559$ yrs, and $2,718 \pm 332$ yrs. Elevations above the surface of the active channel are 24.01 m, 18.13 m, and 3.13 m respectively. The northern CBB transect has 2 ^{10}Be exposure ages: $9,113 \pm 948$ yrs and $7,826 \pm 725$ yrs. These 2 samples are 9.67 m and 1.98 m above the surface of the active channel, respectively (Table 5).

4.4 Apatite and Zircon Thermochronometry

Cooling ages for AHe and ZHe thermochronometry record time since a rock cooled past ~ 60 and $\sim 180^\circ\text{C}$, respectively. One transect along Conde Valley consist of 3 sample locations spanning a vertical distance of 458 m. AHe ages range from 2.94 to 3.88 Ma with analytical errors between 9 and 11% (Table 6). ZHe ages range from 4.42 to 7.20 Ma and have analytical errors between 14 and 19% (Table 7). By fitting a line of best fit to age vs. elevation plots from this data, apparent exhumation rates in Conde valley are 0.16 mm yr^{-1} between ~ 7 and 4 Ma and 0.49 mm yr^{-1} between ~ 4 and 3 Ma (Fig. 16).

5 Discussion

5.1 Patterns in Morphology Along the Cordillera Blanca Mountain Range

The glacial valleys of the Cordillera Blanca are a mix of large basins reaching from the CBDF to the drainage divide and smaller basins occupying the spaces in between (Fig. 9B). Some of the smallest basins extend only a few km into the batholith, almost superimposed onto the western escarpment of the range. A plot of basin areas and mean basin slopes reveals decreasing variability in the mean slope of basins larger than $\sim 50 \text{ km}^2$, which become limited to between ~ 28

and 31° (Fig. 17). A similar trend is observed in maximum slope and modal elevation (Fig. 17), as well as total basin relief, 1 and 3 km radius local relief, and mean elevations (Table 1). Thus, it appears that as the glacial valleys grow in size they trend towards a preferred morphology that is consistent along the strike of the range.

Previous workers have recognized north to south trends in range morphology. Farber and Hancock (*in prep*) note decreasing relief and peak elevations towards the south, citing diminishing glacial erosion as the driving cause. Giovanni (2007) calculated statistics from basins along the strike of the CBDF, but unlike this study the basins extended from the ridgeline down to the confluence with the Rio Santa. Drainage relief, area, mean slope, channel length, channel gradient, range half-width, and hypsometric integral were determined for each of these basins, and north to south trends were similar to those from basins described in this study. Giovanni (2007) describes consistent channel length and gradient along strike, possibly displaying a slight southward decrease, and a southward increase in elevations along the drainage divide. Range half width was determined to reach a minimum near Mt. Huascarán (Fig. 2A). Hypsometric integrals decreased southwards along strike, reflecting a decreasing glacial influence on the distribution of elevations.

The along-strike distribution of the larger (>50 km²) basins provides further insight into the topographic development of the Cordillera Blanca. All of these valleys are located north of ~110 km along strike (Fig. 12B), and their relief is consistently higher than neighboring smaller valleys (<50 km²). Modal elevations in the larger valleys tend to be lower than neighboring smaller valleys, but mean elevations do not seem to differ vary with basin size. Since modal elevations in glacial valleys approximate the flat valley floor, they can be interpreted as a coarse representation of the equilibrium line elevation (ELA; Brozović et al., 1997), and in the Cordillera Blanca modal elevations from the larger valleys are very similar to estimations of the LGM ELA (Fig. 17; see

section 5.1.2). The ELA depends primarily on climate factors such as temperature and precipitation, where lower temperatures or increased precipitation will result in a lower ELA. The better approximation of the ELA by the modal elevation in larger valleys suggests that basin area affects modal elevations and the ELA in the Cordillera Blanca. Perhaps the added accumulation area available to larger valleys allows for a more powerful glacier that is capable of eroding down to the ELA that is dictated by climate factors. The observation that the larger basins are limited to the northern half of the range is interesting (Fig. 12B). The southern limit for large valleys (>50 km²) also corresponds with the southern exposure limit of the CBB (Fig. 5) and the location of a proposed segment boundary in the CBDF (Fig. 2B), supporting the possibility of a lithologic or structural control on the development of large valleys.

5.1.1 Models for topographic evolution of normal fault footwalls.

In the model described by Densmore et al. (2004), normal faults tend to generate a symmetrical, range parallel topographic profile that reflects along-strike gradients in displacement. The highest magnitudes of displacement are found in the center portion of the fault and decreases to zero at the fault tips. Range elevation and relief reach an equilibrium elevation that is controlled by threshold erosive processes and the half width of the footwall, producing fairly level topographic profiles where the fault has accrued enough displacement to reach the threshold topography (Densmore et al., 2004; Densmore et al., 2007). Segmentation in normal faults, such as the CBDF, would also affect the evolution of the fault system, with the aforementioned topographic profile existing over the length of individual segments as well as the whole fault system (Densmore et al., 2004). In the context of normal fault systems, the term “segment” traditionally refers to a portion of a fault that is seismically independent (e.g. Schwartz, 1988; Crone and Haller, 1991; Machette et al., 1991). Due to a lack of recorded surface-rupturing seismicity in the Cordillera Blanca, little is known about the co-seismic

behavior of the fault segments of the CBDF. I will therefore use the term in the geometric sense, as by Schwartz (1988).

Giovanni (2007) compared the Cordillera Blanca to this model of topographic evolution, concluding that the CBDF may be propagating southwards, but the north tip could not be characterized. The identification of increased basin maturity in the northern portion of the mountain range supports the southward propagation of the fault system. The fault development model of Densmore et al. (2004 and 2007) predicts that maximum relief and elevations will be constant in the central portion of the range and variable within ~10-15 km of the fault tips. The CBDF does not follow these trends (Figs. 12 and 13). The footwall topography is highly asymmetrical and elevations and relief vary along its entire ~200 km length, not just near the tips. Densmore et al. (2005) suggests that range half-width controls the maximum relief a range can achieve at a given location along strike, but the Cordillera Blanca does not uphold this notion since relief increases monotonically to the north and range half-width is highly variable along strike (Figs. 2 and 9). In fact, some of the highest relief is found in parts of the range with the narrowest half-width (Figs. 2A and 12A).

Major differences do exist between the study sites of Densmore et al. (2004, 2005 and 2007) and the Cordillera Blanca, which may complicate interpretation. In particular, surface processes in the Cordillera Blanca are mainly due to glacial erosion, as opposed to the fluvial processes active in the Basin and Range, USA. Lithologies are very different as well, with granitoids in the Cordillera Blanca as opposed to the sedimentary units described by Densmore et al. (2004, 2005 and 2007). These differences could be affecting the length and time scales of the model, and it is possible that the topography of the Cordillera Blanca is still approaching a maximum elevation and relief or that the erosional processes acting in the range do not respond to normal fault development in the same way.

The Sierra Nevada Mountain Range in eastern California has many similarities to the Cordillera Blanca. Both ranges feature predominantly granitic lithologies, are bounded on one side by a normal fault system, and have experienced extensive glaciation. The Sierra Nevada also has an asymmetric along-strike topographic profile (Figueroa and Knott, 2010) and relief on the order of 1-2 km (Wakabayashi and Sawyer, 2001). Notable differences lie between the rates of dip-direction fault slip and erosion rates from the two mountain ranges, both of which are lower in the Sierra Nevada (Riebe et al., 2000; Stock et al., 2005; Rood et al., 2011). Since the tectonic setting is much better understood in the Sierra Nevada, relationships may be more easily inferred between the topography and tectonic activity. Extrapolation of these relationships to the Cordillera Blanca may help identify tectonic processes acting in that region, and I suggest this as an avenue for future investigations.

5.1.2 The glacial buzzsaw.

In many glaciated orogens, glacial erosion has been invoked as a mechanism of limiting relief and peak elevations (eg. Brozović et al., 1997; Brocklehurst, 2010). Brozović et al. (1997) introduced the glacial buzzsaw hypothesis, which posits that in glaciated environments the erosive potential of glaciers is capable of keeping pace with rates of tectonic uplift. This will effectively pin the modal elevation of a mountain range at the ELA and limit the peak elevations a mountain range can achieve through threshold limits in valley relief. In the Cordillera Blanca, these predictions are partially upheld. Modal elevations for the range fall between ~4000 and 5000 m a.s.l. (Fig. 12), bridging the elevations of the modern ELA (~5000 m a.s.l.; Rodbell, 1992) and the estimated LGM ELA (~4250 to 4500 m a.s.l.; Smith et al., 2005b). Modal elevations from basins >50km² display less variation, ranging from ~4000 to 4500 m a.s.l., fairly concordant with estimates for the LGM ELA (Fig. 17). Thus, it seems reasonable that glaciation has controlled the modal elevations in the basins of the Cordillera Blanca. The northward decrease in modal elevations could

indicate the northward lowering of the ELA (Brozović et al., 1997) or an increase in the degree of glacial erosion (Molnar and England, 1990). While modal basin elevations seem to be concordant with ELA elevations, peak elevations vary along strike. In the context of the glacial buzzsaw, this suggests that glaciers have pinned modal elevations at the ELA, but have not succeeded in limiting peak elevations. It is possible that the valleys have not reached the threshold relief required for slope failure, or there may be variations in rock strength due to lithologic differences within the batholith.

5.1.3 Morphology of the Calejón de Huaylas Supradetachment Basin

The fault patterns used by Schwartz (1988) to propose segment boundaries in the CBDF outline several major styles of faulting, ordered here from south to north: 1) horse-tailing with formation of a full graben (Figs. 2B and 7C); 2) small, right-stepping to en echelon fragments (Figs. 2B and 7C); 3) A single, continuous strand (Figs. 2B and 7B); and 4) a poorly defined lineation with a complex pattern of smaller structures (Figs. 2B and 7A). The presence of numerous lineations that crosscut the range and supradetachment basin support the presence of additional structures that may be affecting the CBDF as well as basin development. One such feature runs perpendicular to the range in the area between the Carhuish Stock and the southern tip of the CBB (Fig. 2B). The lineation extends across the supradetachment basin, marking a divide between lower relief plains to the south and higher relief foothills to the north. This shift in basin topography suggests that the lineation could be an active structure generating relief on its northern flank. The supradetachment basin has a conspicuous morphology in the region near Mt. Huascarán, where a pattern of lineations suggests a series of parallel, NNW-SSE oriented left-stepping structures linked by another family of E-W to NW-SE oriented structures that cross the basin and possibly extend into the CBB (Fig. 7B). The position of the left-stepping lineations along the western boundary of the basin could indicate the presence of a full graben, as opposed to the half

graben that was previously described in this region (e.g. McNulty and Farber, 2002; Gonzalez and Pfiffner, 2012).

5.2 Validity of the ^{10}Be Basin-averaged Erosion Rates

As described above, the ^{10}Be concentration in sand collected from an active river channel can be used to calculate a basin-averaged erosion rate that is representative of the entire upstream catchment area as long as three main assumptions can be met: 1) that transport time has been short relative to rates of radioactive decay; 2) that erosion has been constant and continuous over the erosion time scale; and 3) that the sample is a well mixed representation of material from the entire basin area.

5.2.1 Assumption 1: short transport time.

Prolonged sediment storage is a potential problem in the valleys of the Cordillera Blanca. River systems tend to be transport limited and large amounts of sediment can be stored in the riverbanks. In the glacial basins of the Cordillera Blanca Mountain Range, the flat valley floors are filled with dense organic-rich bogs, termed *pampas*, which potentially store many cubic kilometers of sediment and peat (Fig. 4A; Maharaj et al., *In Prep*). The dynamics of sediment storage and transport can produce extremely complex exposure histories for CRNs. Deeply buried sediment will be shielded from further irradiation, allowing radioactive decay to decrease CRN concentrations. Sediment stranded on or near the surface, such as on an overbank deposit or fill terrace, will continue to be irradiated and accumulate CRNs. In the former scenario, decreased CRN concentrations due to burial will result in an artificially high erosion rate. In the latter, increased CRN concentrations due to post-erosion exposure will produce an artificially low erosion rate. Despite the potential for loss of the original ^{10}Be concentration, the magnitude of the effects may not be large enough to significantly affect erosion rate calculations: Whitmann and von Blanckenburg (2009) modeled the potential effects of sediment storage in a wide range of basins

and floodplains, and concluded that isotopes with long half-lives (such as ^{10}Be) are generally not effected by sediment storage and mixing with previously shielded bank deposits. Thus, I take this assumption to be valid.

5.2.2 Assumption 2: constant erosion over the erosion time scale.

The erosion time scale for a basin is inversely proportional to the calculated erosion rate, and may be calculated using Eq. 6. The erosion time scale represents the time needed for an eroding basin to reach equilibrium between CRN production through *in situ* spallogenic reactions and CRN removal through erosion. Higher erosion rates require less time to reach this equilibrium since rock advecting towards the surface will spend relatively less time within the top few meters of the earth where *in situ* CRNs are produced. Samples from this dataset have erosion time scales ranging from ~130 to 40,000 years, reflecting the 3 orders of magnitude variation in measured erosion rates. Most samples from the Cordillera Blanca Mountain Range have erosion time scales less than a few thousand years.

Considering the primarily glacial environment of the Cordillera Blanca, it is reasonable to assume the valleys have experienced varying degrees of glaciation during multiple glacial advances. In addition, there has been a long-term decrease in glaciation since the LGM. Geologic evidence, on the other hand, supports the continued aridity with episodic precipitation in the region since at least 40 ka (Wells and Noller, 1997), indicating long-term continuity of precipitation patterns. Many of the basins in this study have a mainly fluvial morphology, indicating that the dynamics of glacial erosion will have a minimal effect on the basin-wide erosion rate. The basins along the western flank of the Cordillera Blanca, on the other hand, have textbook glacial morphology and certainly reflect glacial processes. Basin-averaged erosion rates from these basins will bridge multiple glacial advances over the course of their integration time scale, effectively integrating the processes acting during these times. Additionally, ice cover since the LGM would have left significant portions of the

valley floor and walls exposed, so paraglacial processes, not sub-glacial erosion, would drive erosion in these areas. In this sense, erosion rates can be taken to be sufficiently continuous over the time scales applicable to this study.

5.2.3 Assumption 3: well-mixed sample.

The assumption of a well-mixed sample is difficult to justify in this study area. The paraglacial valleys of the Cordillera Blanca Mountain Range and the steep-sided fluvial valleys to the north and east are prone to landsliding. Mass wasting events pull deep-seated, less-exposed rock from valley walls, which can contaminate a sample and bias it toward a higher erosion rate. The degree to which landslide material has affected the measured erosion rates is difficult to determine, as it involves numerous unquantified variables such as: landslide frequency (both spatial and temporal), depth of landsliding, and the rate that landslide-originated sediment is supplied to the channel (Niemi et al., 2005). Niemi et al. (2005) determined that landslide-prone basins are more likely to produce reliable results if they are larger than a certain threshold area. The authors note that the threshold area is inversely proportional to the measured erosion rate and suggest the following relationship (Eq. 5):

$$(5) \quad A_{th} = \frac{100 \text{ km}^3 \text{ Myr}^{-1}}{\epsilon}$$

Where A_{th} is the threshold area in km^2 and ϵ is in units of mm yr^{-1} . Out of the 21 analyzed basins in my data set, only 4 meet the above criteria: one from the Cordillera Blanca Mountain Range (Honda Valley), and the 3 largest basins in this study (Rio Santa, Rio Marañon, and Rio Chuquicara). Eleven of the remaining 17 basins are within one order of magnitude of the suggested minimum area. The potential for overestimation of erosion rates due to landslide contamination is high, and care must be taken when interpreting the results from the Cordillera Blanca region.

5.2.4 Estimation of total error.

The new data affords an opportunity to estimate the uncertainty in our ^{10}Be basin-averaged erosion rate measurements. Three samples were taken from above and below a confluence in the upper reaches of the Chuquicara River: one from each tributary (RP07-R1 and RP07-R2) and one from the main channel (RP07-R3; Fig. 9A). By weighting the measured erosion rates from the two tributaries by their sediment flux, their combined average erosion rate can be predicted with a simple two end-member mixing model (Eq. 6; e.g. Wittman and von Blanckenburg, 2009):

$$(6) \quad \varepsilon_p = \left(\frac{Q_a}{Q_t} \times \varepsilon_a \right) + \left(\frac{Q_b}{Q_t} \times \varepsilon_b \right)$$

Where ε_p is the predicted erosion rate for the combined basin; ε_a and ε_b are the measured erosion rates for the two sub basins; Q_a and Q_b are the sediment flux from the two basins, calculated as $Q = \varepsilon * \text{area}$; and Q_t is the sum of Q_a and Q_b . The two sub-basins have erosion rates of 0.076 and 0.044 mm yr⁻¹ and areas of 326 and 367 km², respectively. Using equation 6, the erosion rate for the combined basin area is predicted to be 0.064 mm yr⁻¹. The measured erosion rate for the combined area is 0.086 mm yr⁻¹, suggesting a comprehensive ~25% error in the measured erosion rates.

5.2.5 Comparison to previous work.

Comparison of new data from this study to other ^{10}Be basin-averaged erosion rate measurements from nearby and global studies supports the validity of the new data. Portenga and Bierman (2011) compiled and recalculated data from 87 ^{10}Be erosion rate studies covering the equivalent of ~2.3% of the earth's land area. Using the time dependent scaling scheme of Balco et al. (2008), erosion rates spanned from ~0 to 5 mm yr⁻¹ with a mean of 0.218 mm yr⁻¹. The distribution was heavily skewed towards lower erosion rates, with a median value of 0.054 mm yr⁻¹. Higher erosion rates were associated with tectonically active regions like the Himalaya or the Andes. Abbuhl et al. (2011) presented ^{10}Be

basin-averaged erosion rates from two rivers draining the Western Cordillera of northern Peru, the Rios Piura and Pisco, which ranged from ~ 0.01 to 0.25 mm yr^{-1} .

All but one of the new basin-averaged erosion rates from this study fall within the ranges of values described in the studies above. The remaining sample returned an anomalous erosion rate relative to the global data set (RS11-BE05, erosion rate of $\sim 4 \text{ mm yr}^{-1}$), prompting me to interpret it to contain an unrepresentative amount of landslide material and exclude it from further analysis. All of the high erosion rates come from basins along the western flank of the Cordillera Blanca Mountain Range. Basins to the north and east of the Cordillera Blanca Mountain Range have a smaller range of erosion rates bracketed by those described by Abbuhl et al. (2011). While it may seem suspicious that the highest erosion rates come from the paraglacial and highly landslide prone basins of the Cordillera Blanca Mountain Range, they are also spatially associated with active base level lowering along the CBDF and more extensive glaciation, both of which could generate higher erosion rates. The potential effects of the CBDF on erosion rates are discussed below.

5.2.6 Interpretation of ^{10}Be erosion rate results.

In summary, the basin-averaged erosion rates presented here should be regarded as high-end estimates due to the potential for contamination with landslide material. A sediment flux error estimation suggests that the external error is on the order of 25%, and the rates fall within the range of measured values for similar climatic and tectonic regimes elsewhere on earth. Considering the potential error, little emphasis will be placed on the finite amounts of the measured erosion rates. Instead, trends in relative concentration will be used in interpretations.

5.3 Regional Patterns in Erosion Rates and Morphology

Considering the range of climatic and tectonic environments surrounding the Cordillera Blanca, it is helpful to divide the region into three general morpho-tectonic provinces: 1) the upper Rio Santa watershed including basins along the western flank of the Cordillera Blanca Mountain Range and the Rio Santa itself; 2) the region north of the Cordillera Blanca Mountain Range, including the Rio Chuquicara watershed and the sub-basins in its upper reaches; and 3) the Rio Marañon watershed and sub-basins to the east of the Rio Santa watershed (Fig. 9B). The upper Rio Santa is arid (Johnson, 1976) and predominantly formed in the basin generated by the CBDF, although the westerly draining basins in the fault's footwall flow into this drainage as well. The Rio Chuquicara shares a similar climate with the Rio Santa Basin (Fig. 2C), but it drains an area that is outside of the zone of apparent deformation associated with the CBDF (Fig. 2B). The Rio Marañon region drains the eastern flank of the Cordillera Blanca Mountains, receives ~2 to 3 times more precipitation (Johnson, 1976), and occupies a portion of the footwall block of the CBDF. Glacial features can be observed in all 3 regions, but they are most prevalent in the footwall of the CBDF. Valley systems in the Rio Marañon and Chuquicara regions have highly fluvial morphologies, and glacial features are limited in extent.

¹⁰Be erosion rate and morphometric data from the analyzed basins do not produce any strong linear, exponential, or logarithmic correlations. A weak correlation exists between mean basin elevation and mean basin slope ($R^2 = 0.68$; Fig. 18), suggesting the occurrence of steeper hillslopes in higher catchments. By considering the 3 morpho-tectonic regions together, it becomes clear that the basins in the Rio Santa are steeper and at higher mean elevations as compared to the more fluvial Rio Chuquicara and Rio Marañon regions. A mean basin slope of ~22° clearly divides the dataset (Fig. 18). The highest part of the region, the Cordillera Blanca Mountains, have enough area above the ELA to support glaciation, and as such have developed the steep slopes typical of glacial

landscapes. The fluvial basins of the Rio Chuquicara and Rio Marañon have lower mean basin slopes, limited to between ~ 19 and 21° , while the glacial basins have mean slopes ranging from ~ 20 to 35° (Fig. 18).

No statistically significant relationship could be found between the basin-averaged erosion rates and mean basin slopes. Mean slopes reach a maximum value of ~ 29 to 31° (Fig. 19A), similar to the values described by Montgomery and Brandon (2002) in the Washington Cascades and Burbank et al. (1996) in the Himalaya. In these studies, mean basin slopes were shown to reach a threshold value at which erosion rates increased asymptotically, and a similar relationship was found for local relief in the Washington Cascades (Montgomery and Brandon, 2002). It is possible that some valleys have reached a threshold slope in the Cordillera Blanca, but there is no evidence for a similar relationship in relief across the Cordillera Blanca region (Fig. 19B). Three kilometer radius local relief varies by more than 2000 m across the glacial valleys, but most of the fluvial basins fall within a ~ 500 m window (Fig. 19B). This wide range of values for local relief in the glacial basins of the Rio Santa is unusual for glacial environments, since glacial valleys tend to limit relief to an approximate threshold value above the ELA (e.g. Brozović et al., 1997), and may indicate that the valleys have not reached this threshold (see section 5.1.2).

The Cordillera Blanca as has the fastest erosion rates in the study area (mean of 0.68 mm yr^{-1}), while the regions to the north and east are generally lower (means of 0.065 and 0.11 mm yr^{-1} , respectively; Fig. 15). Granted, this could be an effect of sampling resolution since sample sites are heavily weighted to the high basins of the western flank of the Cordillera Blanca, but the higher erosion rates could also be explained as the product of warm-based glaciation or higher rates of relief production due to slip along the CBDF (e.g. Thompson et al., 2010). Relationships between erosion rates and the CBDF are discussed further in section 5.7.

If the glacial basins are excluded, more subtle differences between the fluvial systems can be described. The drainages from the Rio Marañon have the highest erosion rates, and are tightly clustered between 0.094 and 0.12 mm yr⁻¹ (Fig. 15; Table 4). The sample from the main trunk of the Rio Santa (RS07-R2) produced an erosion rate of 0.084 mm yr⁻¹, and the erosion rates from the Rio Chuquicara range from 0.044 to 0.086 mm yr⁻¹. While the difference is small, the elevated erosion rates from the Rio Marañon could be the result of increased rainfall on the eastern flank of the Cordillera Blanca (Fig. 2C; Johnson 1976). The erosion rate from the Rio Santa falls within the range of rates from the Rio Chuquicara, but is slightly higher than the average. While it is somewhat surprising that the more structurally active Rio Santa region returned such a similar rate, it is also draining the arid and tectonically quiescent Cordillera Negra Mountain Range and is subject to influences of the large population that lives within the drainage system. Examples of such influences include hydroelectric dams and the introduction of mine tailings and runoff, both of which could potentially modify the ¹⁰Be concentration in a downstream sample.

The low erosion rates in the sub-basins of the Rio Chuquicara, as compared to the western Cordillera Blanca, likely reflect the glacial and structural differences between the 2 regions. The northern extent of the CBDF is not precisely known, and is not readily apparent on satellite imagery or DEMs of the Rio Chuquicara region (Fig. 2). Giovanni (2007) suggested that the fault is pinned near this region and is unable to propagate further northwards. The lower basin-averaged erosion rates in the region adjacent to the known northern extent of the CBDF (Figs. 2B and 15) could indicate that the fault is pinned just to the south, although I can not rule out the possibility of a northward propagating fault tip that has not yet affected the ¹⁰Be basin-averaged erosion rates in that area. The different glacial history in the region could also be responsible for the muted erosion rates. No modern glaciers exist in the Rio Chuquicara drainage (Fig. 2A), and it is not clear when the system transitioned from glacial to fluvial.

5.4 Patterns in Erosion Along the Cordillera Blanca Mountain Range

Along-strike patterns are apparent in ^{10}Be basin-averaged erosion rates from the Cordillera Blanca Mountain Range, despite the large range of measured values. Most basins have erosion rates between ~ 0.11 and 0.40 mm yr^{-1} (Table 4), although a collection of elevated rates between ~ 0.88 and 1.1 mm yr^{-1} are found between ~ 90 and 110 km along strike (Fig. 12). Basins $>50 \text{ km}^2$ have consistently higher erosion rates than smaller neighboring basins. So not only do these basins have lower modal elevations and higher relief (see section 5.1), but they are eroding faster as well.

Despite the potential for overestimation of erosion rates due to landslide contamination (see section 5.2), I interpret the rates from the Cordillera Blanca to be valid for the following reasons: 1) with the exception of one small zone of faster erosion, erosion rates consistently fall within a narrow band of values; 2) in the zone of faster erosion, three adjacent valleys produced similar results; and 3) the fastest erosion rates in a given locality come from the largest basins, which tend to be less sensitive to landslide contamination (Niemi et al., 2005). Thus, the locality between ~ 90 and 110 km along strike (with erosion rates over 2 times faster than the rest of the range) can be interpreted as representing a zone of faster erosion and not landslide bias. Unfortunately, both samples collected between 40 and 89 km along strike returned unreliable results: RS11-BE05 was biased by low concentration landslide material (see section 5.2.5), and RS11-BE04 produced an unreliable analytical result. Despite the analytical problem, the measured ^{10}Be concentration and calculated erosion rate ($\sim 0.35 \text{ mm yr}^{-1}$) in RS11-BE04 probably represents an approximation of the erosion rate, albeit statistically poor (R. Finkel, *Per. Comm.*). In the absence of any other data from that portion of the range, RS11-BE04 will be used as a placeholder to predict the trends in erosion rate through that portion of the range.

While being a coarse approximation, the measured value from RS11-BE04 fits fairly well with the rest of the erosion rate data (Fig. 12). This sample

corresponds to Llanganuco Valley, adjacent to Huascarán, which is large (>50km²) and in the portion of the range with the highest peak elevations and very high relief. The approximation is similar to erosion rates measured in the larger basins immediately to the north (~0.3 to 0.4 mm yr⁻¹), suggesting that it could be reasonably accurate. Since this is not verifiable, I will consider the data both with and without the questionable data point.

The 3 elevated erosion rates come from basins around the large salient near Huaráz (Figs. 2A and 15). If RS11-BE04 is excluded, the large gap in data between 40 and 89 km along strike prevents the identification of any patterns through the central portion of the range. It is clear, however, that the northern and southern ends of the sample distribution are eroding at similar, slower rates compared to the area around the salient. Without RS11-BE04, the northern limit to the elevated erosion rates is unclear. If sample RS11-BE04 is taken to be acceptable, erosion rates around Huascarán are effectively equal to the rates observed along the rest of the range and the zone of elevated erosion rates is truly limited to the area around the salient.

Along-strike patterns in relief, elevation, modern glacial cover, and slope show little resemblance to patterns in erosion rate, with or without the addition of sample RS11-BE04 (Fig. 12). The apparent disconnection between ¹⁰Be basin-averaged erosion rates and any form of morphometry requires that the forces responsible for the distribution of topography be different than those responsible for erosion over at least as long as the ¹⁰Be erosion timescale (~10³-10⁵ years). Aside from the zone of elevated erosion rates, the rest of the mountain range is eroding at a similar pace to the Chuquicara and Marañón valleys (Fig. 15), as well as the Rio Piura to the northwest (Abbuhl et al 2010) and Rio Pisco to the south (Abbuhl et al., 2011).

The zone of elevated erosion rates corresponds to the basins around the large salient near Huaraz. This salient was interpreted as marking a segment boundary in the CBDF (Schwartz, 1988), and roughly marks a gradual transition

in the morphology of the Callejón de Huaylas Supradetachment Basin from high relief and narrow in the north to broad and flat in the south. Segment boundaries can be associated with higher degrees of fracturing (e.g. Janecke, 1993), which could weaken the bedrock and promote higher erosion rates. Alternatively, precipitation patterns could have an effect: TRMM annual rainfall measurements identify a locus of increased precipitation in the area around the salient, as well as around Huascarán (Fig. 2C). Considering the 4 km horizontal and $\sim 1000 \text{ mm yr}^{-1}$ rainfall resolutions, as well as the limited ~ 20 year dataset, the true difference cannot be precisely evaluated. In any case, a local increase in precipitation could be responsible for the elevated erosion rates. However, if the sample from near Huascarán is considered (RS11-BE04), it is not clear why the increased precipitation that occurs in that region would not result in higher erosion rates as well.

5.5 River Incision

Exposure ages from fluvially polished bedrock (Fig. 10) were calculated from two vertical transects: 1) along the northern reach of the Rio Santa in the granite of the Coastal Batholith (3 ages), and 2) within the northern portion of the CBB, just on the footwall side of the main trace of the CBDF (2 ages; Fig. 9A). In the transect from the Coastal Batholith, exposure ages yield time-averaged incision rates of $0.95 \pm 0.45 \text{ mm yr}^{-1}$ between $\sim 12,000$ and $6,000$ yrs B.P., and $4.76 \pm 2.33 \text{ mm yr}^{-1}$ between $\sim 6,000$ and $2,700$ yrs B.P (Fig. 20). In the Cordillera Blanca transect, the time-averaged incision rate between ~ 9000 and 8000 yrs B.P. is $5.98 \pm 0.64 \text{ mm yr}^{-1}$.

If the active channel is considered to have an exposure age of 0 years, an additional incision rate may be calculated. All elevation differences were measured from the surface of the active channel, but the base of the channel is the true location of material with no exposure history. At the Cordillera Blanca transect the river was very shallow, with a depth of no more than ~ 0.2 m (Fig.

10B). In the Coastal Batholith transect, however, the river is quite deep and the true depth is unknown. Using the surface of the active channel, minimum time-averaged incision rates can be calculated for the 2 locations: $1.15 \pm 0.94 \text{ mm yr}^{-1}$ since ~ 2700 yrs B.P. for the Coastal Batholith transect and $0.25 \pm 0.27 \text{ mm yr}^{-1}$ since ~ 8000 yrs B.P. for the Cordillera Blanca transect (Fig. 20). Using approximate channel depths of $2.0 \pm 1.0 \text{ m}$ for the Coastal Batholith and $0.1 \pm 0.1 \text{ m}$ for the Cordillera Blanca produces incision rates of $1.89 \pm 1.55 \text{ mm yr}^{-1}$ and $0.27 \pm 0.29 \text{ mm yr}^{-1}$, respectively. The difference between the two methods is significant for the Coastal Batholith transect, but fairly negligible for the Cordillera Blanca transect.

Using the surface of the active channel (0 cm depth) as the base of the transect, the minimum long-term incision rate for the Coastal Batholith transect is $2.01 \pm 2.09 \text{ mm yr}^{-1}$, and for the Cordillera Blanca is $1.06 \pm 1.02 \text{ mm yr}^{-1}$. While it is interesting that the long-term incision rate from the transect associated with a large active structure (the CBDF) is lower, it is important to note that the two long-term incision rates represent different tectonic and climatic influences. Tectonically, the Coastal Batholith transect likely represents regional uplift while the Cordillera Blanca transect likely represents local relief production across the CBDF. In this regard, the difference in magnitude between the 2 overall incision rates could reflect differences in the tectonic uplift and relief generation rates, but it could also include the effects of lithology and stream power.

Time-averaged river incision at the Coastal Batholith locality is generally between ~ 1 to 2 mm yr^{-1} with the exception of a period of accelerated incision between ~ 3000 and 6000 yrs B.P. (Fig. 20B). At the Cordillera Blanca locality the recorded time-averaged incision is rapid for ~ 1000 yrs before decreasing around 8000 yrs B.P. (Fig. 20B). As discussed above, river incision rates can record changes in climate and relative base level. Both transects have overall incision rates on the order of 1 or 2 mm yr^{-1} , but contain a period of accelerated incision rates between 4 and 6 mm yr^{-1} . The periods of accelerated incision do not

overlap temporally, suggesting independent causes. It is not clear what produced the periods of accelerated incision, but possible causes could include tectonic processes or changes in stream power. A punctuated tectonic event could generate regional uplift or relief along the CBDF. Stream power could be affected by episodic events, such as a lake outburst flood, or changes in the upstream precipitation or supply of glacial meltwater.

5.6 Exhumation of the Cordillera Blanca Batholith

The new thermochronologic transect presented in this study extends the known cooling history of the range southwards into the Carhuish Stock. This smaller intrusion was emplaced around 13 Ma (Mukasa, 1984), making it older than the CBB by over 5 Ma. Its similarity in chemistry to the CBB and the Yungay Ignimbrites suggest a similar origin, despite the difference in age (13.7 vs. 9 to 5.4 Ma; Cobbing et al., 1981).

Giovanni (2007) and Montario (2001) present apparent age-elevation-relationship (AER) exhumation rates from the CBB, describing the cooling history of the batholith between ~7 and 2 Ma. Transects from Llanganuco Valley using AHe, AFT, and biotite $^{40}\text{Ar}/^{39}\text{Ar}$ all yield apparent exhumation rates between 0.45 and 0.55 mm yr⁻¹. Biotite $^{40}\text{Ar}/^{39}\text{Ar}$ transect from further north and south (Yanac and Honda Valleys) produced apparent exhumation rates of 0.18 and 0.19 mm yr⁻¹, respectively, evidencing faster exhumation near Llanganuco Valley over the timescale recorded by biotite $^{40}\text{Ar}/^{39}\text{Ar}$ (~7 to 5 Ma). A linear regression of the AER of the AHe data from Honda Valley (Giovanni, 2007) has a negative slope, giving the appearance of a negative exhumation rate. A negative regression line can be formed when a valley is losing relief (Braun, 2002). A closer look at the 5 AHe ages from Honda Valley reveals a clear outlier: the oldest age (4.01 ± 2.59 Ma) is not only near the bottom of the transect, which is opposite the standard AER, but has an extremely high analytical error of nearly 65%. If this age is taken as an outlier a positive AER is produced, equating to an apparent

exhumation rate of 0.26 mm yr^{-1} . While the possibility exists that relief has diminished as these samples cooled past the AHe closure temperature, this notion seems highly unlikely. Honda Valley is one of the larger, more mature glacial valleys in the Cordillera Blanca, which have some of the highest amounts of relief in the Mountain Range. As such, I choose to remove the outlier from the AHe data set and use the resultant exhumation rate in further discussion: Honda Valley seems to have exhumed at around half of the pace of Llanganuco over the same time interval (~ 7 to 2 Ma).

The new transect from the southern end of the fault system records exhumation from ~ 7 to 3 Ma, with apparent exhumation rates of 0.16 mm yr^{-1} between 7 and 4 Ma and 0.49 mm yr^{-1} from 4 to 3 Ma. This may indicate an increase in exhumation rate around 4 Ma, or it may be the result of topographic effects on the thermal gradient. It is interesting, however, that the age ranges for the ZHe and AHe transects in the Carhuish Stock correspond almost exactly with the age ranges for biotite $^{40}\text{Ar}/^{39}\text{Ar}$ and AHe transects in the CBB, respectively (Fig. 21). The difference in closure temperatures for ZHe ($\sim 180^\circ\text{C}$) and biotite $^{40}\text{Ar}/^{39}\text{Ar}$ ($\sim 350^\circ\text{C}$) has significant implications for the interpretation of these apparent exhumation rates. Even though the two methods record data from a similar range of ages, the CBB and Carhuish Stock must have been experiencing very different thermal conditions during that time. An explanation for this must reconcile the fact that before 4 Ma the CBB was twice as hot as the Carhuish Stock, but both were at the same temperature by ~ 3 Ma. One possibility is that the CBB has been rapidly exhumed from a deeper level since before 4 Ma, which would require the removal of an additional 6 or 7 km of overburden (Montario, 2001) and exhumation rates on the order of ~ 3 to 4 km yr^{-1} . Another possibility is that the biotite $^{40}\text{Ar}/^{39}\text{Ar}$ ages from the CBB record rapid conductive cooling after batholith emplacement at shallow crustal levels. The reality is likely a combination of these models. Petford and Atherton (1992) proposed the coeval emplacement and exhumation of the CBB along the CBDF. I support this model

for the following three reasons: 1) while there is no known evidence for the removal of an extra 6 km of material in the CBB versus the Carhuish Stock, the CBDF is much more developed in the north and may have differentially exhumed different locations; 2) U-Pb ages from the CBB overlap with biotite $^{40}\text{Ar}/^{39}\text{Ar}$ ages by about 2 Myr, suggesting rapid cooling during emplacement; and 3) the older Carhuish Stock might be cooler than the CBB since it has had more time to thermally equilibrate with its surroundings.

5.7 Regional patterns of exhumation.

The 6 AERs from the Cordillera Blanca Batholith indicate that exhumation has been fairly continuous between ~ 7 and 2 Ma. Rates were faster in Llanganuco Valley ($\sim 0.5 \text{ mm yr}^{-1}$) and slower ($\sim 0.2 \text{ m yr}^{-1}$) to the north and south, although AER exhumation rates after ~ 4 Ma have not been measured north of Llanganuco (Fig. 21). Exhumation rates from Conde Valley in the Carhuish Stock ~ 10 km south of the CBB were slow between ~ 7 and 4 Ma (0.16 mm yr^{-1}) and as rapid as Llanganuco between ~ 4 and 3 Ma (0.49 mm yr^{-1}).

Exhumation rates are very similar to ^{10}Be basin-averaged erosion rates from much of the range (Fig. 21), suggesting that the Cordillera Blanca has been erosionally exhumed at a fairly constant pace between ~ 0.1 to 0.5 km Myr^{-1} since ~ 7 Ma. The elevated ^{10}Be basin-averaged erosion rates, which correspond to the area around Honda Valley, are a clear exception and must be a relatively short-term and recent occurrence.

Garver et al. (2005) used zircon fission track (ZFT) and ZHe analysis in the Cordillera Huayhuash just south of the Cordillera Blanca to identify a period of rapid cooling around 11 Ma followed by erosional exhumation. No exhumation rates were reported. Michalak et al. (*In Prep*) reported similar ranges of AHe cooling ages from transects near Sihuas and Balsas (Fig. 1), suggesting increases in erosional exhumation around 10 Ma. Another transect from the Rio Pampas, on the northern border of the Cordillera Blanca Mountain Range, records

ZHe ages between 24.9 ± 10 and 2.7 ± 0.2 Ma, as well as a single AHe age of 2.0 ± 0.2 Ma (Michalak et al., *In Prep*). The young ZHe and AHe ages are very similar to AHe ages from the Cordillera Blanca, which generally range from ~ 4 to 2 Ma, prompting the authors to associate the increase in exhumation with the CBDF.

5.8 Implications for the Evolution of the Cordillera Blanca and the CBDF

Spatial and temporal patterns of erosion and exhumation in the Cordillera Blanca Mountain Range begin to outline the emplacement and exhumation of the CBB as well as the initiation and evolution of the CBDF. With the exception of the older ZHe ages from the Rio Pampas in the upper Rio Chuquicara watershed reported by Michalak et al. (*In Prep*), all of the thermochronologic data from the Cordillera Blanca are younger than ~ 7 Ma. Exhumation rates derived from AERs are between 0.1 and 0.5 km Myr⁻¹ throughout the range, although a variety of thermochronologic systems and closure temperatures complicate interpretation. ¹⁰Be basin-averaged erosion rates are generally similar to longer-term exhumation rates, with the exception of the region near the large salient near Huaraz and Honda Valley, which are much faster (~ 1 mm yr⁻¹). As discussed above, the similarity between biotite ⁴⁰Ar/³⁹Ar ages from the CBB and ZHe ages from the Carhuish Stock necessitates different magnitudes of post-cooling exhumation. Larger amounts would be needed in the CBB, which is supported by the higher elevations and relief in the northern half of the range where the CBB is present. It is unclear how much of the exhumation was driven through erosion versus displacement along the CBDF.

ZHe ages from the northern end of the Cordillera Blanca Mountain Range do not record the cooling event between ~ 7 and 4 Ma, but the single AHe age is very similar to the rates observed in the CBB. In the Carhuish Stock near the southern end of the range ZHe data record similar apparent exhumation rates to the CBB, but through a lower closure temperature. AHe ages from the southern

end of the mountain range are very similar to the rest of the range, as is the apparent exhumation rate. This supports less exhumation at the ends of the mountain range during the ~7 to 4 Ma time window relative to the CBB. After ~4 Ma, however, the cooling history appears to be fairly consistent along the entire length of the Cordillera Blanca. This pattern is consistent with the northward and southward propagation of the CBDF past these sites prior to ~4 Ma.

The zone of elevated ^{10}Be erosion rates near the large salient in the range front aligns with one of the proposed segment boundaries of Schwartz (1988) and marks a broad change in both the style of faulting along the CBDF and basin morphology (Fig. 2B). As discussed above, the elevated erosion rates could be caused by an increased level of structural deformation and fracturing due to fault segment interaction. However, other ^{10}Be basin-averaged erosion rates measured from catchments near proposed segment boundaries, such as the region near the town of Huayllanca, are not elevated. Something must be unique about the salient segment boundary to produce the observed pattern. Along-strike patterns in basin relief change at this point, gaining much more irregularity on the south side (Fig. 12). The occurrence of the large, mature basins ceases south of this zone as well, indicating less developed glacial morphology. Since the salient marks the boundary between the more glacial and less glacial portions of the range, the elevated erosion rates may be recording relief generation due to recently enhanced glacial erosion. Alternatively, the two segments could have joined relatively recently and the elevated erosion rates could be in response to equilibration to a new structural regime.

Granted, without accurate data from the region immediately north of the salient segment boundary I cannot be certain that the section of the range from the salient to Mt. Huascarán is not eroding quickly as well. If the approximated erosion rate from Llanganuco Valley (RS11-BE04) is not actually representative, the zone of elevated erosion rates could be much more wide spread, and could follow the trend of increased displacement along the CBDF described by Farber

and Hancock (*In Prep*; Fig. 21). Considering the current data, however, it appears that displacement rate is not a first-order control on the erosion rates in the basins bounded by the CBDF.

Since incision rates are potentially sensitive to changes in relative base level, the rates from the Cordillera Blanca transect may reflect relief generation across the CBDF in the far north. The time-averaged incision rate of $\sim 1 \text{ mm yr}^{-1}$ falls within the range of measured fault displacement rates, which taper from 5.1 ± 0.8 to $0.59 \pm 0.2 \text{ mm yr}^{-1}$ between the area just north of Llanganuco Valley down to Querrococha Valley in the south (Fig. 21; Farber and Hancock, *In Prep*). If this incision rate is taken as a proxy for displacement rate for the CBDF, the along-strike pattern of displacement could be interpreted as decreasing north of Huascarán. The transect is located in the footwall of the CBDF and is high above the valley floor, indicating that river incision is not capable of keeping pace with rates of base level change at this knick point. In this context, if all of the river incision is due to displacement along the CBDF, the measured overall incision rate is best interpreted as a minimum slip-rate. A slip-rate of $>1 \text{ mm yr}^{-1}$ in the northern extent of the CBDF indicates that the fault is rapidly generating relief, and loosely constrains the northern continuation of the fault slip rates measured by Farber and Hancock (*In Prep*).

6 Conclusion

The Cordillera Blanca of northern Peru has been subjected to the influences of structural deformation and glacial erosion, resulting in topography that represents these two processes and their interactions. This study has characterized the deformational history of the mountain range from the perspectives of Holocene erosion rates, late Miocene exhumation rates, and analysis of the modern topography. To accomplish this, I have drawn upon a collection of techniques: ^{10}Be basin-averaged erosion rates, AHe and ZHe low temperature thermochronology, and GIS-based digital terrain analysis. I find:

1. Clear north-south patterns in range morphology can be observed along the Cordillera Blanca in data retrieved from both individual fault-bounded basins and broader scale swath profiles. These data depict the trend from steeper, high-relief basins in the north to lower-relief basins in the south. Modal basin elevations decrease northwards, but mean elevations do not seem to vary substantially along strike. Patterns in range topography do not strictly follow predictions from models of glacial erosion or normal fault development.
2. Basins along the western flank of the Cordillera Blanca are consistently higher elevation and higher relief than basins located towards the north and east, reflecting the strong glacial influence on the morphology of the range.
3. Fault segmentation within the CBDF has shaped the evolution of the adjacent supra-detachment basin. Sharp changes in the morphology of the valley and style of faulting could indicate the presence of active cross-valley structures.
4. The glacially-sculpted valleys along the western flank of the Cordillera Blanca have higher erosion rates than valleys to the north and east. This may be due to either: 1) a higher degree of glacial erosion or 2) enhanced relief generation along the CBDF, or a combination of both.
5. Erosion rates along the Cordillera Blanca generally fall between 0.1 and 0.5 mm yr⁻¹. A zone of higher erosion rates (~1 mm yr⁻¹) exists near the center of the range, concordant with a probable segment boundary in the CBDF. It appears that varying rates of fault slip along the CBDF do not have a first-order effect on erosion rates, but further measurements are required for verification.
6. AHe and ZHe analyses from Conde Valley near the southern end of the range yield similar AER exhumation rates to thermochronologic studies from the rest of the range (~0.2 to 0.5 km Myr⁻¹).

7. The similarity between longer-term exhumation rates and shorter-term erosion rates suggests fairly constant erosional denudation in the Cordillera Blanca since ~7 Ma.
8. River incision rates from the two transects likely represent a combination of tectonic and climatic processes. If incision at the Cordillera Blanca transect is taken to reflect base level change across the CBDF, a minimum fault slip rate of ~1 mm yr⁻¹ can be inferred, possibly indicating a decrease in slip rate north of Mt. Huascaran.

My findings indicate that while the topography of the Cordillera Blanca clearly reflects tectonic and climatic processes, general models for predicting patterns of mountain range morphology are not sufficient in this region. The outline of the thermal history of the range provided here indicates along strike cooling trends, and erosion rates suggest long-term continuity in exhumation rates. Future work characterizing the finer-scale thermal history of the CBB will allow for numerical modeling of its emplacement and exhumation due to fault activity and erosion, which will be critical to understanding the dynamics of the range and the CBDF.

7 References Cited

- Abbuhl, LM., KP. Norton, F. Schlunegger, O. Kracht, A. Aldahan, and G. Possnert. (2010). El Niño forcing on ¹⁰Be-based surface denudation rates in the northwestern Peruvian Andes? *Geomorph.* 123:257-268.
- Abbuhl, LM., KP. Norton, JD. Jansen, F. Schlunegger, A. Aldahan, and G. Possnert. (2011). Erosion rates and mechanisms of knickzone retreat inferred from ¹⁰Be measured across strong climate gradients on the northern and central Andes Western Escarpment. *Earth Surf. Process. Landforms.* 36:1,464-1,473.
- Ames, A. (1998). A documentation of glacier tongue variations and lake developments in the Cordillera Blanca. *Zeitschrift für Gletscherkunde und Glazialgeologie.* 34(1):1-26.
- Armstrong, R., B. Raup, SJS. Khalsa, R. Barry, J. Kargel, C. Helm, and H. Kieffer. (2005). GLIMS glacier database. *Boulder, Colorado USA: National Snow and Ice Data Center.* Digital Media.
- Atherton, MP. and M. Sanderson. (1987). The Cordillera Blanca Batholith: a study of granite intrusion and the relation of crustal thickening to peraluminosity. *Geologische Rundschau.* 76(1):213-232.
- Atherton, MP. (1990). The Coastal Batholith of Peru: the product of rapid recycling of 'new' crust formed within rifted continental margin. *Geol. Jour.* 25:337-349.
- Atherton, MP. and N. Petford. (1993). Generation of sodium-rich magmas from newly underplated basaltic crust. *Nature.* 362:144-146.

- Balco, G., JO. Stone, NA. Lifton, and TJ. Dunai. (2008). A complete and easily accessible means of calculating surface exposure ages or erosion rates from ^{10}Be and ^{26}Al measurements. *Quat. Geochron.* 3:174-195.
- Barnes, JB., TA. Ehlers, N. McQuarrie, PB. O'Sullivan, and JD. Pelletier. (2006). Eocene to recent variation in erosion rates across the central Andean fold-thrust belt, northern Bolivia: Implications for plateau evolution. *Earth Plan. Sci. Lett.* 248:118-133.
- Berger, AL., JA. Spotila, JB. Chapman, TL. Pavilis, E. Enkelmann, NA. Ruppert, and JT. Buscher. (2008). Architecture, kinematics, and exhumation of a convergent orogenic wedge: A thermochronological investigation of tectonic-climatic interactions within the central St. Elias orogen, Alaska. *Earth Plan. Sci. Lett.* 270:13-24.
- Bierman, PR., and KK. Nichols. (2004). Rock to sediment – Slope to sea with ^{10}Be – Rates of landscape change. *Annu. Rev. Earth. Plan. Sci.* 32:215-255.
- Bishop, P. (2007). Long-term landscape evolution: linking tectonics and surface processes. *Earth Surf. Process. Landforms.* 32:329-365.
- Bonnet, S. and A. Crave. (2003). Landscape response to climate change: insights from experimental modeling and implications for tectonic versus climatic uplift of topography. *Geology.* 31(2):123-126.
- Bonnet, C., J. Malavieille, and J. Mosnar. (2008). Surface processes versus kinematics of thrust belts: impact on rates of erosion, sedimentation, and exhumation – Insights from analog models. *Bull. Soc. Geol. Fr.* 179(3):297-314.
- Bookhagen, B. and MR. Strecker. (2008). Orographic barriers, high-resolution TRMM rainfall, and relief variations along the eastern Andes. *Geophys. Res. Lett.* 35:L06403.
- Bookhagen, B. (in review). High resolution spatiotemporal distribution of rainfall seasonality and extreme events based on a 12-year TRMM time series.
- Braun, J. (2002). Quantifying the effect of recent relief changes on age-elevation relationships. *Earth Plan. Sci. Lett.* 200:331-343.
- Brocklehurst, SH. (2010). Tectonics and Geomorphology. *Prog. Phys. Geog.* 34:357-383.
- Brown, ET., RF. Stallard, MC. Larsen, GM. Raisbeck, and F. Yiou. (1995). Denudation rates determined from the accumulation of *in situ*-produced ^{10}Be in the Luquillo Experimental Forest, Puerto Rico. *Earth Planet. Sci. Lett.* 129:193-202.
- Brozović, N., DW. Burbach, AJ. Meigs. (1997). Climatic Limits on Landscape Development in the Northwestern Himalaya. *Science.* 276:571-574.
- Buck, WR. (1991). Modes of continental lithospheric extension. *Jour Geophys. Res.* 96:20,161-20,178.
- Burbank, DW., J. Leland, E. Fielding, RS. Anderson, N. Brozovic, MR. Reid, and C. Duncan. (1996) Bedrock incision, rock uplift and threshold hillslopes in the northwestern Himalayas. *Nature.* 379:505-510.
- Chmeleff, J., F. von Blanckenburg, K. Kossert, D. Jakob. (2010). Determination of the ^{10}Be half-life by multicollector ICP-MS and liquid scintillation counting. *Nuc. Inst. Meth. Phys. Res.* 268:192-199.
- Cobbing, EJ., WS. Pitcher, JJ. Wilson, JW. Baldock, WP. Taylor, W. McCourt, and NJ. Snelling. (1981). The Geology of the Western Cordillera of Northern Peru. *Institute of Geological Sciences, London.*
- Cobbing, EJ. and AW. Sanchez. (1996). Mapa geologico del cuadrangulo de Huaraz, 1:100,000. *Instituto Geologico Minero y Metalurgico.* Digitized 1996.
- Coldwell, B., J. Clemens, N. Petford. (2011). Deep crustal melting in the Peruvian Andes: Felsic magma generation during delamination and uplift. *Lithos.* 125:272-286.
- Crider, JG. (2001). Oblique slip and the geometry of normal-fault linkage: mechanics and a case study from the Basin and Range in Oregon. *Jour. Struct. Geol.* 23:1997-2009.
- Crone, AJ. and KM. Haller. (1991). Segmentation and the coseismic behavior of Basin and Range normal faults: examples from east-central Idaho and southwestern Montana. *Jour Struct. Geol.* 13(2):151-164.
- Cruz, L., C. Teyssier, L. Perg, A. Take, and A. Fayon. (2008). Deformation, exhumation, and topography of experimental doubly-vergent orogenic wedges subjected to asymmetric erosion. *Jour. Struct. Geol.* 30:98-115.
- Davis, W.M. (1899). The geographical cycle. *The Geog. Jour.* 14(5):481-504.
- Delunel, R., PA. van der Beek, J. Carcaillet, DL. Bourlés, PG. Valla. (2010). Frost-cracking control on catchment denudation rates: Insights from *in situ* produced ^{10}Be concentrations

- in stream sediments (Ecrins-Pelvoux massif, French Western Alps). *Earth Plan. Sci. Lett.* 293:72-83.
- Densmore, AL., NH. Dawers, S. Gupta, PA. Allen, and R. Gilpin. (2003). Landscape evolution at extensional relay zones. *Jour. Geophys. Res.* 108(B5):2273.
- Densmore, AL., NH. Dawers, S. Gupta, R. Guifon, T. Goldfin. (2004). Footwall topographic development during continental extension. *Jour. Geophys. Res.* 109:F03001.
- Densmore, AL., NH. Dawers, S. Gupta, R. Guidon. (2005). What sets topographic relief in extensional footwalls? *Geology.* 33(6):453-456.
- Densmore, AL., S. Gupta, PA. Allen, NH. Dawers. (2007). Transient landscapes at fault tips. *Jour. Geophys. Res.* 112:F03S08.
- DePolo, CM., DG. Clark, DB. Slemmons, and AR. Ramelli. (1991). Historical surface faulting in the Basin and Range province, western North America: implication for fault segmentation. *Jour. Struct. Geol.* 13(2):123-136.
- Desilets, D., M. Zreda. (2003). Extended scaling factors for *in situ* cosmogenic nuclides: New measurements at low latitude. *Earth Plan. Sci. Lett.* 176:157-169.
- Dortz., KL., B. Meyer, M. Sébrier, H. Nazari, R. Braucher, M. Fattahi, L. Benedetti, M. Foroutan, L. Siame, D. Bourlés, M. Talebian, MD. Bateman, and M. Ghoraiishi. (2009). Holocene right-slip rate determined by cosmogenic and OSL dating on the Anar fault, Central Iran. *Geophys. Jour. Int.* 179:700-710.
- Doser, DI. (1987). The Ancash, Peru, earthquake of 1946 November 10: evidence for low-angle normal faulting in the high Andes of northern Peru. *Geophys. Jour. Royal. Astr. Soc.* 91:57-71.
- Dumitru, TA., PB Gans, DA. Foster, and EL. Miller. (1991). Refrigeration of the Western Cordilleran lithosphere during Laramide shallow-angle subduction. *Geology.* 19(11): 1145-1148.
- Dumont, JF. (1996). Neotectonics of the Subandes-Brazilian craton boundary using geomorphological data: the Marañon and Beni basins. *Tectonophysics.* 257:137-151.
- Dunai, TJ. (2001). Influence of secular variation of the geomagnetic field on production rates of *in situ* produced cosmogenic nuclides. *Earth Plan. Sci. Lett.* 193:197-212.
- Fabel, D., AP. Stroeven, J. Harbor, J. Kleman, D. Elmore, and D. Fink. (2002). Landscape preservation under Fennoscandian ice sheets determined from *in situ* produced ¹⁰Be and ²⁶Al. *Earth Plan. Sci. Lett.* 201:397-406.
- Farber, DL., GS. Hancock, RC. Finkel, and DT. Rodbell. (2005). The age and extent of tropical alpine glaciation in the Cordillera Blanca, Peru. *Jour. Quat. Sci.* 20(7-8):759-776.
- Farber, DL. and GS. Hancock. (*In Preparation*). The role of tectonics and climate in uplift along the Cordillera Blanca Detachment Fault, Peru.
- Farrar, E. and DC. Noble. (1976). Timing of late Tertiary deformation in the Andes of Peru. *Bull. Geol. Soc. Am.* 87:1247-1250.
- Figueroa, AM. and JR. Knott. (2010). Tectonic geomorphology of the southern Sierra Nevada Mountains (California): Evidence for uplift and basin formation. *Geomorph.* 123:34-45.
- Finnegan, NJ., B. Hallet, DR. Montgomery, PK. Zeitler, JO. Stone, AM. Anders, and L. Yuping. (2008). Coupling of rock uplift and river incision in the Namche Barwa-Gyala Peri massif, Tibet. *GSA Bull.* 120:142-155.
- Fortin, MA. and SR. Hall. (2011). Knickpoint analysis and glacial geochronology of the Cordillera Blanca, Peru. *Undergraduate Research Conference*. Poster.
- Garver, JJ., PW. Reiners, LJ. Walker, JM. Ramage, and SE. Perry. (2005). Implications for timing of Andean uplift from thermal resetting of radiation-damaged zircon in the Cordillera Huayhuash, Northern Peru. *Jour. Geol.* 113:117-138.
- Gerya, TV., D. Fossati, C. Cantieni, and D. Seward. (2009). Dynamic effects of aseismic ridge subduction: numerical modeling. *Eur. Jour. Min.* 21:649-661.
- Giletti, BJ. and HW. Day. (1968). Potassium-argon ages of igneous intrusive rocks in Peru. *Nature.* 220:570-572.
- Giovanni, MK. (2007). Tectonic and thermal evolution of the Cordillera Blanca Fault Zone, Peruvian Andes: Implications for normal faulting in a contractional orogen. *Ph.D. Dissertation, Department of Earth Sciences, University of California, Los Angeles.*
- Giovanni, MK., BK. Horton, CN. Garzzone, B. McNulty, and M. Grove. (2010). Extensional basin development in the Cordillera Blanca, Peru: Stratigraphic and isotopic records of detachment faulting and orogenic collapse in the Andean Hinterland. *Tectonics.*

29:TC6007.

- Glasser, NF., S. Clemmens, C. Schnabel, CR. Fenton, and L. McHargue. (2009). Tropical glacier fluctuations in the Cordillera Blanca, Peru between 12.5 and 7.6 ka from cosmogenic ^{10}Be dating. *Quat. Sci. Rev.* 28:3,448-3,458.
- Gosse, GC., and FM. Phillips. (2001). Terrestrial *in situ* cosmogenic nuclides: theory and application. *Quart. Sci. Rev.* 20:1,475-1,560.
- Gonzalez, L. and OA. Pfiffner. (2012). Morphologic evolution of the Central Andes of Peru. *Int. Jour. Earth. Sci.* 101:307-321.
- Gregory-Wodzicki, KM. (2000). Uplift history of the central and northern Andes: A review. *GSA Bull.* 112(7):1091-1105.
- Gutscher, MA., JL. Oliviet, D. Aslanian, JP. Eissen, R. Maury. (1999). The “lost Inca Plateau”: cause of flat subduction beneath Peru? *Earth Plan. Sci. Lett.* 171:335-341.
- Gutscher, M., W. Spakman, H. Bijwaard, and ER. Engdahl. (2000). Geodynamics of flat subduction: Seismicity and tomographic constraints from the Andean margin. *Tectonics.* 19(5):814-833.
- Gutscher, M. (2002). Andean subduction styles and their effect on thermal structure and interplate coupling. *Jour. South Amer. Earth Sci.* 15:3-10.
- Haederle, M. and MP. Atherton. (2002). Shape and intrusion style of the Coastal Batholith, Peru. *Tectonophysics.* 345:17-28.
- Hall, SR., DL. Farber, L. Audin, RC. Finkel, and AS. Mériaux. (2008). Geochronology of pediment surfaces in southern Peru: Implications for Quaternary deformation of the Andean forearc. *Tectonophysics.* 459:186-205.
- Hall, SR., DL. Farber, JM. Ramage, DT. Rodbell, RC. Finkel, JA. Smith, BG. Mark, and C. Kassel. (2009). Geochronology of Quaternary glaciations from the tropical Cordillera Huayhuash, Peru. *Quat. Sci. Rev.* 28:2,991-3,009.
- Hilley, GE. and MR. Strecker. (2004). Growth and erosion of fold-and-thrust belts with an application to the Aconcagua fold-and-thrust belt, Argentina. *Jour. Geophys. Res.* 109:B01410.
- Hilley, GE. and I. Coutand. (2010). Links between topography, erosion, rheological heterogeneity, and deformation in contractional settings: Insights from the central Andes. *Tectonophysics.* 495:78-92.
- Insel, N., TA. Ehlers, M. Schaller, JB. Barnes, S. Tawackoli, CJ. Poulsen. (2010). Spatial and temporal variability in denudation across the Bolivian Andes from multiple geochronometers. *Geomorph.* 122:66-77.
- Janecke, SU. (1993). Structures in segment boundary zones of the Lost River and Lemhi Faults, east central Idaho. *Jour. Geophys. Res.* 98(B9):61,223-16,238.
- Johnson, AM. (1976). The climate of Peru, Bolivia and Ecuador. In: *Schwerdtfeger (Ed.), World Survey of Climatology.* Elsevier, Amsterdam. pp. 147-218.
- Kaser, G. and C. Georges. (1997). Changes of the equilibrium-line altitude in the tropical Cordillera Blanca, Peru, 1930-50, and their spatial variations. *Ann. Glac.* 24:344-349.
- Kohl, CP., and K. Nishiizumi. (1992). Chemical isolation of quartz for measurement of *in situ*-produced cosmogenic nuclides. *Geochim. Cosmochim. Acta.* 56(9):3,583-3,587.
- Koppes, MN., DR. Montgomery. (2009). The relative efficacy of fluvial and glacial erosion of modern to orogenic timescales. *Nat. Geosci.* 2:644-647.
- Lal, D. (1991). Cosmic ray labeling of erosion surfaces: *in situ* nuclide production rates and erosion models. *Earth Plan. Sci. Lett.* 104:424-439.
- Lamb, S. and P. Davis. (2003). Cenozoic climate change as a possible cause for the rise of the Andes. *Nature.* 425:792-797.
- Lifton, N., J. Bieber, J. Clem, M. Duldig, P. Evenson, J. Humble, and R. Pyle. (2005). Addressing solar modulation and long-term uncertainties in scaling secondary cosmic rays for *in situ* cosmogenic nuclide applications. *Earth Plan. Sci. Lett.* 239:140-161.
- Machette, MN., SF. Personius, AR. Nelson, DP. Schwartz, and WR. Lund. (1991). The Wasatch fault zone, Utah – segmentation and history of Holocene earthquakes. *Jour. Struct. Geol.* 11(2):137:149.
- Maharaj, L., JM. McKenzie, KR. Hodson, SR. Hall, and BG. Mark. (*In Preparation*). Investigating proglacial groundwater systems in the Quilcayhuanca and Yanamarey Pampas, Cordillera Blanca, Peru.

- Malavieille, J. and E. Konstantinovskaya. (2010). Impact of surface processes on the growth of orogenic wedges: insights from analog models and case studies. *Geotectonics*. 44(6): 541-558.
- Manea, VC., M. Pérez-Gussinyé, and M. Manea. (2012). Chilean flat subduction controlled by overriding plate thickness and trench rollback. *Geology*. 40(1):35-38.
- Mark, BG. and GO. Seltzer. (2005). Evaluation of recent glacier recession in the Cordillera Blanca, Peru (AD 1962-1999): spatial distribution of mass loss and climate forcing. *Quart. Sci. Rev.* 24:2,265-2,280.
- McNulty, B., DL. Farber, GS. Wallace, R. Lopez, O. Palacios. (1998). Role of plate kinematics and plate-slip-vector partitioning in continental magmatic arcs: Evidence from the Cordillera Blanca, Peru. *Geology*. 26(9):927-830.
- McNulty, B. and D. Farber. (2002). Active detachment faulting above the Peruvian flat slab. *Geology*. 30(6):567-570.
- Megard, F. (1984). The Andean orogenic period and its major structures in central and northern Peru. *Jour. Geol. Soc. London*. 141:893-900.
- Michalak, MJ., SR. Hall, DL. Farber, L. Audin, JK. Hourigan, and EJ. Rose. (In Preparation). Late Miocene-Pliocene accelerated exhumation in the northern Peruvian Andes.
- Molnar, P., and P. England. (1990). Late Cenozoic uplift of mountain ranges and global climate change: chicken or egg? *Nature*. 346: 29-34.
- Montario, MJ. (2001). Exhumation of the Cordillera Blanca Batholith, northern Peru, based on apatite fission track analysis. *Undergraduate Honors Thesis, Department of Geology, Union College, NY*.
- Montgomery, DR., G. Balco, SD. Willett. (2001). Climate, tectonics, and the morphology of the Andes. *Geology*. 29(7):579-582.
- Montgomery, DR., and MT. Brandon. (2002). Topographic controls on erosion rates in tectonically active mountain ranges. *Earth and Plan. Sci Lett*. 201:481-489.
- Montgomery, DR. and DB. Stolar. (2006). Reconsidering Himalayan river anticlines. *Geomorph*. 82:4-15.
- Mukasa, BS. (1984). Comparative Pb isotope systematics and zircon U-Pb geochronology for the Coastal, San Nicholas, and Cordillera Blanca Batholiths, Peru. *Ph.D. Dissertation, University of California, Santa Barbara*.
- Niemi, NA., M. Oskin, DW. Burbank, AJ. Heimsath, EJ. Gabet. (2005). Effects of bedrock landslides on cosmogenically determined erosion rates. *Earth Plan. Sci. Lett*. 237:480-498.
- Nishiizumi, K., E. Winterer, C. Kohl, J. Klein, R. Middleton, D. Lal, J. Arnold. (1989). Cosmic ray production rates of ²⁶Al and ¹⁰Be in quartz from glacially polished rocks. *Jour. Geophys. Res.* 94:17,907-17,915.
- Norabuena, E., L. Leffler-Griffin, A. Mao, T. Dixon, S. Stein, IS. Sacks, L. Ocola, and Michael Ellis. (1998). Space geodetic observations of Nazca-South America convergence across the Central Andes. *Science*. 279:358-362.
- Petford, N., MP. Atherton. (1992). Granitoid emplacement and deformation along a major crustal lineament: the Cordillera Blanca, Peru. *Tectonophysics*. 205:171-185.
- Petford, N., M. Atherton. (1996). Na-rich partial melts form newly underplated basaltic crust: the Cordillera Blanca Batholith, Peru. *Jour. Pet.* 37(6):1491-1521
- Racoviteanu, AE., Y. Arnaud, MW. Williams, J. Ordoñez. (2008). Decadal changes in glacier parameters in the Cordillera Blanca, Peru, derived from remote sensing. *Jour. Glaciology*. 54(186):499-510.
- Raymo, ME. and WF. Ruddiman. (1992). Tectonic forcing of late Cenozoic climate. *Nature*. 359:117-122.
- Riebe, CS., JW. Kirchner, DE. Granger, RC. Finkel. (2000). Erosional equilibrium and disequilibrium in the Sierra Nevada, inferred from cosmogenic ²⁶Al and ¹⁰Be in alluvial sediment. *Geology*. 28(9):803-806.
- Reiners, PW., and MT. Brandon. (2006). Using thermochronology to understand orogenic erosion. *Annu. Rev. Earth Plan. Sci.* 34:419-466.
- Rodbell, DT. (1992). Late Pleistocene equilibrium-line-altitude reconstructions in the northern Peruvian Andes. *Boreas*. 21:43-52.
- Rodbell, DT. (1993). The timing of the last deglaciation in Cordillera Occidental, northern Peru, based on glacial geology and lake sedimentology. *GSA Bull.* 105:923-934.

- Rodbell, DT., GO. Seltzer, BG. Mark, JA. Smith, and MB. Abbott. (2008). Clastic sediment flux to tropical Andean lakes: records of glaciation and soil erosion. *Quat. Sci. Rev.* 27:1612-1626.
- Rodbell, DT., JA. Smith, BG. Mark. (2009). Glaciation in the Andes during the Lateglacial and Holocene. *Quart. Sci. Rev.* 28:2,165-2,212.
- Rood, DH., DW. Burbank, RC. Finkel. (2011). Spatiotemporal patterns of fault slip rates across the Sierra Nevada Frontal Fault Zone. *Earth Plan. Sci. Lett.* 301:457-468.
- Ryan, WBF. (2009). Global multi-resolution topography synthesis. *Geochem. Geophys. Geosyst.* 10(Q03014);doi 10.1029/2008GC002332.
- Safran, EB., PR. Bierman, R. Aalto, T. Dunne, KX. Whipple, and M. Caffee. (2005). Erosion driven by channel network incision in the Bolivian Andes. *Earth Surf. Process. Landforms.* 30:1,007-1,024.
- Safran, EB., A. Blythe, T. Dunne. (2006). Spatially variable exhumation rates in orogenic belts: An Andean example. *Jour. Geology.* 114(6):665-681.
- Saillard, M., SR. Hall, L. Audin, DL. Farber, V. Regard, G. Hérail. (2011). Andean coastal uplift and active tectonics in southern Peru: ¹⁰Be surface exposure dating of differentially uplifted marine terrace sequences (San Juan de Marcona, ~15.4°S). *Geomorph.* 128:178-190.
- Schildgen, T., DP. Dethier, P. Bierman, and M. Caffee. (2002). ²⁶Al and ¹⁰Be dating of late Pleistocene and Holocene fill terraces: A record of fluvial deposition and incision, Colorado Front Range. *Earth Surf. Process. Land.* 27:773-787.
- Schwartz, DP. (1988). Paleoseismicity and neotectonics of the Cordillera Blanca Fault Zone, Northern Peruvian Andes. *Jour. Geophys. Res.* 93(B5):4,712-4,730.
- Smith, JA., GO. Seltzer, DL. Farber, DT. Rodbell, RC. Finkel. (2005a). Early local Last Glacial Maximum in the tropical Andes. *Science.* 308:678-681.
- Smith, JA., GO. Seltzer, DT. Rodbell, AG. Klein. (2005b). Regional synthesis of last glacial maximum snowlines in the tropical Andes, South America. *Quat. Int.* 139-139:145-167.
- Stewart, JW., JF. Evernden, and NJ. Snelling. (1974). Age determinations from Andean Peru: a reconnaissance survey. *GSA Bull.* 85:1107-1116.
- Stock, GM., RS. Anderson, RC. Finkel. (2005). Rates of erosion and topographic evolution of the Sierra Nevada, California, inferred from ²⁶Al and ¹⁰Be concentrations. *Earth Surf. Process. Landforms.* 30:985-1006.
- Stone, JO. (2000). Air pressure and cosmogenic isotope production. *Jour. Geophys. Res.* 105(B10):23,753-23,759.
- Suarez, G., P. Molnar, and BC. Burchfiel. (1983). Seismicity, fault plane solutions, depth of faulting, and active tectonics of the Andes of Peru, Ecuador, and Southern Columbia. *Jour. Geophys. Res.* 88(B12):10,403-10,428.
- Thompson, SN., MT. Brandon, JH. Tomkin, PW. Reiners, C. Vásquez, and NJ. Wilson. (2010). Glaciation as a destructive and constructive control on mountain building. *Nature.* 467:313-317.
- USGS and Japan ASTER Program. (2003). Multiple scenes. 1B. USGS, Sioux Falls.
- USGS. (2006). Shuttle radar topography mission. 1 Arc Second scene srtm_21_13 and 1 Arc Second scene srtm_21_15, version 2.0. *Global Land Cover Facility, Univ. Maryland.* College Park, Maryland, February 2000.
- Valla, PG., PA. van der Beek, and J. Carcaillet. (2010). Dating bedrock gorge incision in the French Western Alps (Ecrins-Pelvoux massif) using cosmogenic ¹⁰Be. *Terra Nova.* 22:18-25.
- Von Blanckenburg, F. (2005). The control Mechanisms of erosion and weathering at basin scale from cosmogenic nuclides in river sediment. *Earth Plan. Sci. Lett.* 237:462-479.
- Wakabayashi, J. and TL. Sawyer. (2001). Stream incision, tectonics, uplift and evolution of topography of the Sierra Nevada, California. *Jour. Geol.* 109:539-562.
- Wells, LE. and JS Noller. (1997). Determining the early history of the El Niño. *Science.* 276:965-967.
- Whipple, KX. (2004). Bedrock rivers and the geomorphology of active orogens. *Annu. Rev. Earth Planet. Sci.* 32:151-185.
- Whipple, KX. And BJ. Meade. (2006). Orogen response to changes in climatic and tectonic forcing. *Earth Plan. Sci. Lett.* 243:218-228.
- Whipple, KX. (2009). The influence of climate on the tectonic evolution of mountain belts. *Nat. Geosci.* DOI:10.1038.

- Whittaker, AC., PA. Cowie, M. Attal, GE. Tucker, and GP. Roberts. (2007). Contrasting transient and steady-state rivers crossing active normal faults: new field observations from the Central Apennines, Italy. *Basin Res.* 19:529-556.
- Willenbring, JK. and F. von Blanckenburg. (2010). Long-term stability of global erosion rates and weathering during late-Cenozoic Cooling. *Nature.* 463:211-214.
- Willett, SD. (1999). Orogeny and orography: The effects of erosion on the structure of mountain belts. *Jour. Geophys. Res.* 104(B12):28,957-28,981.
- Willett, SD. and MT Brandon. (2002). On steady states in mountain belts. *Geology.* 30(2): 175-178.
- Wittmann, H., F. von Blanckenburg. (2009). Cosmogenic nuclide budgeting of floodplain sediment transfer. *Geomorph.* 109:246-256.
- Yanites, BJ., GE. Tucker, and RS. Anderson. (2009). Numerical and analytical models of cosmogenic radionuclide dynamics in landslide-dominated drainage basins. *Jour. Geophys. Res.* 114:F01007.
- Yonekura, N., T. Matsuda, M. Nogami, and S. Kaizuka. (1979) An active fault along the western foot of the Cordillera Blanca, Peru. *Jour. Geogr.* 88:1-19.
- Zehfuss, PH., PR. Bierman, AR. Gillespie, RM. Burke, and MW. Caffee. (2001). Slip rates on the Fish Springs fault, Owens Valley, California, deduced from cosmogenic ¹⁰Be and ²⁶Al and soil development on fan surfaces. *GSA Bull.* 113(2):241-255.
- Zhang, P., P. Molnar, and WR. Downs. (2001). Increased sedimentation rates and grain sizes 2-4 Myr ago due to the influence of climate change on erosion rates. *Nature.* 410:891-897.

Appendix 1: Relationships Between Erosion and Uplift

Molnar and England (1990) carefully defined the terms rock uplift, surface uplift, and erosion and represented the relationship between them in this simple expression (Eq. A1):

$$(A1) \quad \text{Rock Uplift} = \text{Surface Uplift} + \text{Erosion}$$

in which rock uplift is defined as the vertical movement of a package of rock, surface uplift is the vertical movement of the surface of the earth, and erosion is the rate of mass removal from the surface, all of which are measured relative to a reference depth such as mean sea level, a datum, or the center of the earth. In this model, a scenario where rock uplift is precisely matched by erosion will result in no change in the elevation of the earth's surface. Likewise, a scenario with little or no erosion will result in surface uplift that equals rock uplift. In subduction zones, rock uplift is mainly controlled by the collision of tectonic plates and the accretion of crustal material to the base of the crust. This can generate "equilibrium topography" where rock uplift is matched by erosion rates and surface uplift is effectively zero (Whipple and Meade, 2006; Hilley and Strecker, 2004; Molnar and England, 1990). In tectonically inactive areas, erosional lowering of surface elevations induces isostatic rock uplift. In this scenario, mean surface elevations will have a net lowering (ΔH) described by (Eq. A2):

$$(A2) \quad \Delta H = \frac{\Delta T(\rho_m - \rho_c)}{\rho_m}$$

in which ΔT is the mean thickness of eroded material and ρ_m and ρ_c are the densities of the mantle and crust, respectively (Molnar and England, 1990). In the case of the Cordillera Blanca, there is potential for tectonically driven rock uplift along the Cordillera Blanca Detachment Fault as well as isostatic uplift due to glacial erosion.

Figures

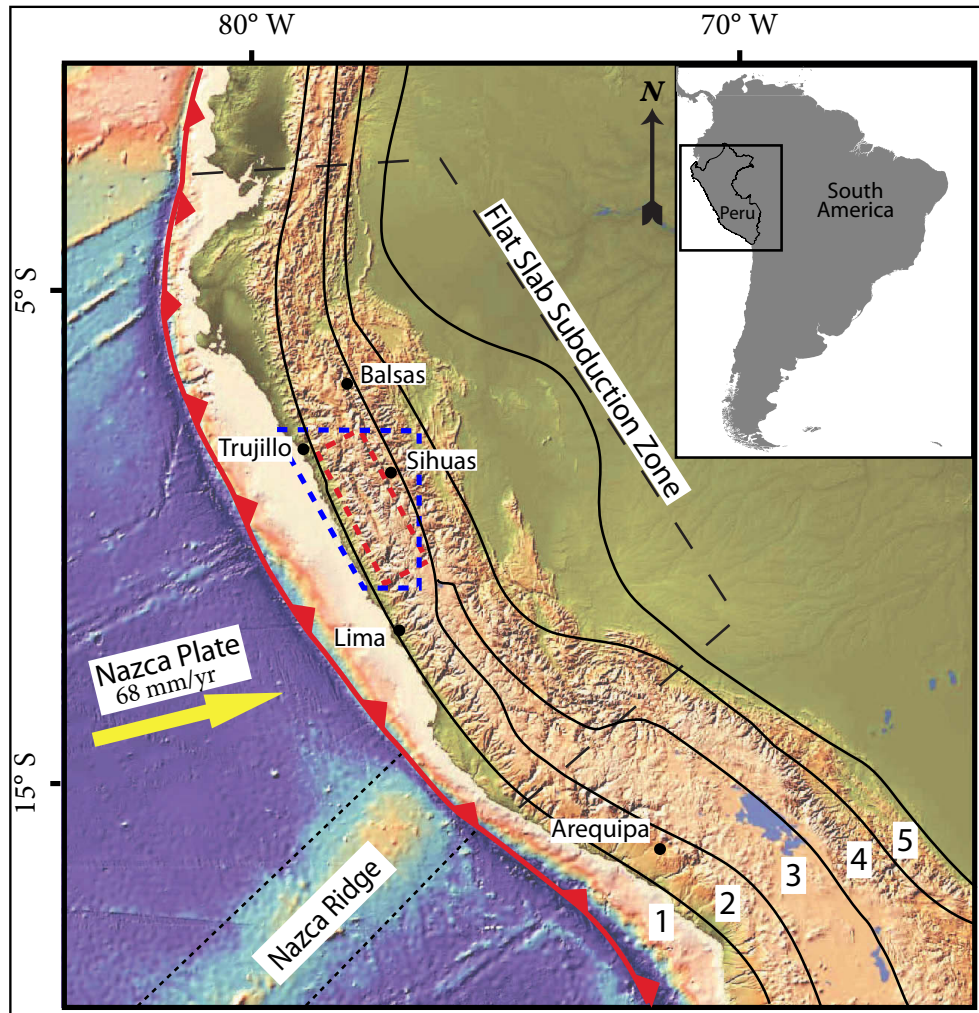


Figure 1. Tectonic map of northern South America displaying prominent features and important provinces. Dashed black line denotes approximate boundary of the northern flat-slab subduction zone. Dotted black line marks the boundary of the Nazca Ridge. Direction of Nazca Plate motion is displayed by the yellow arrow along with plate velocity relative to stable South America (Norabuena et al., 1998). Solid black lines mark boundaries between the major morpho-tectonic provinces: (1) Coastal Plains, (2) Western Cordillera, (3) Altiplano, (4) Eastern Cordillera and (5) sub-Andean zone (after Suarez et al., 1983). Red dashed line indicates location of Fig. 2 and blue dashed line indicates location of Fig. 5. Basemap image from Ryan et al. (2009) and <http://www.geomapapp.org>.

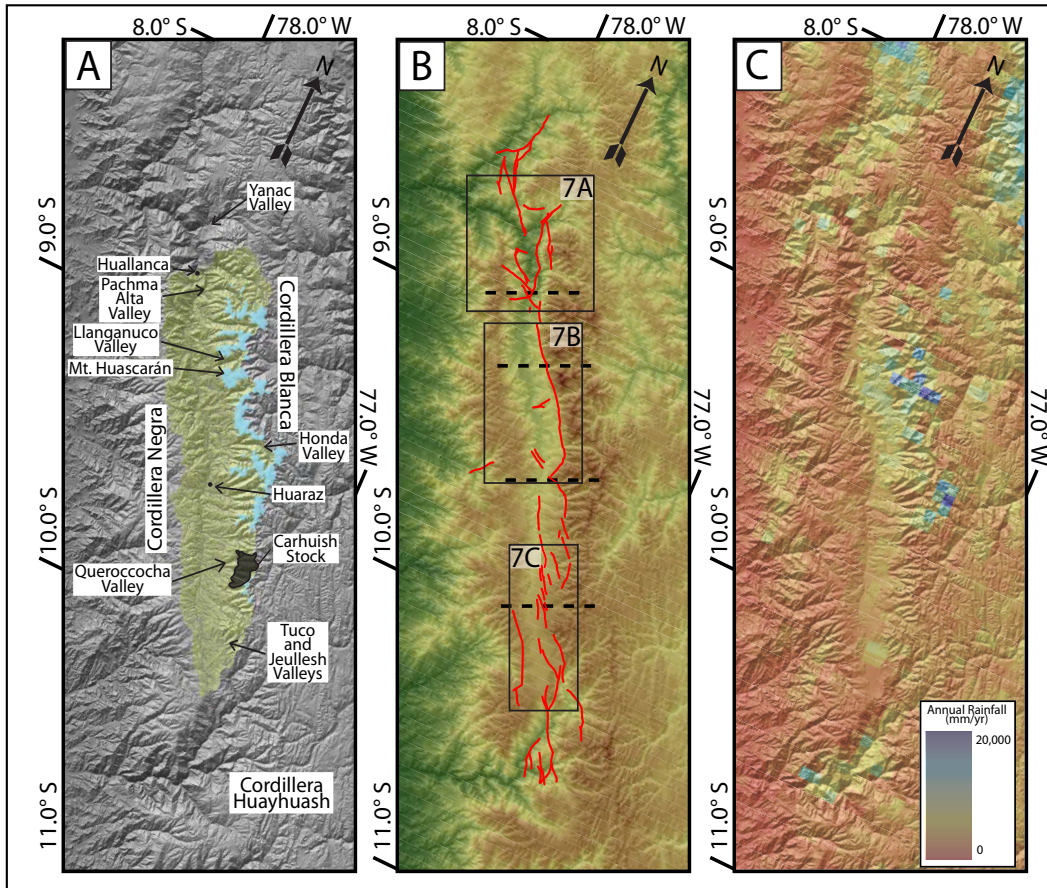


Figure 2. Geographic, structural, and Tropical Rainfall Measurement Mission (TRMM) maps of the Cordillera Blanca, Peru. (A) Geographic map of the Cordillera Blanca region displaying the names and locations of mountain ranges (Cordilleras), cities and valleys discussed in the text on a SRTM 90m shaded relief map. Yellow shaded area corresponds to the Callejón de Huaylas Supradetachment basin and light blue areas are locations of modern glaciers. Dark grey-shaded area indicates mapped extent of the Carhuish Stock. (B) Structural map of the CBDF displayed on a SRTM 90m shaded relief map. Red lines represent fault trace published in INGEMET 30' quadrangle geologic maps. Dashed black lines mark the approximate locations of segment boundaries suggested by Schwartz (1988). Black boxes refer to locations of panels in Figure 7. (C) TRMM annual rainfall map overlain onto a SRTM 90 m shaded relief map. TRMM compilation from Bookhagen (in review), hillshade maps modified from SRTM DEMs (USGS, 2006).



Figure 3. Photographs of the CBDF. Clockwise from upper left: A) view south-west along the footwall escarpment of the CBDF (Fig. 2B), displaying ~1 km vertical relief; B) south-west view of offset Quaternary moraine material near Querococha Valley (Fig. 2A), terrace material visible on valley floor is that of Farber and Hancock (*in prep*); C) preserved fault scarp with striations indicating right-lateral slip component (pocket knife in lower right corner for scale); D) south-west facing outcrop view of scarp in image C, located ~10 km north of Mt. Huascaran (Fig. 2A).

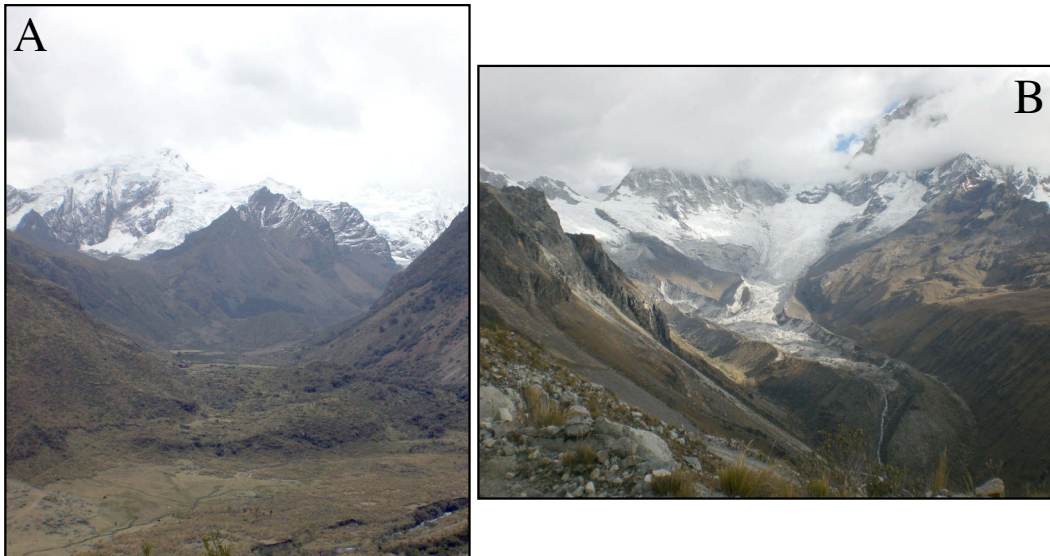


Figure 4. Photographs of glacial features in the Cordillera Blanca. (A) North-west view up Quilcayhuanca Valley (near Huaraz), representing the typical U-shaped glacial valley morphology in the region with modern glaciers visible on the peaks. Multiple terminal and lateral moraines are visible on the valley floor, as well as pampa and bog sediments in foreground. (B) South-west view of modern glacier retreating from recent moraine on the east side of Mt. Huascaran (partially concealed by clouds in upper right corner).

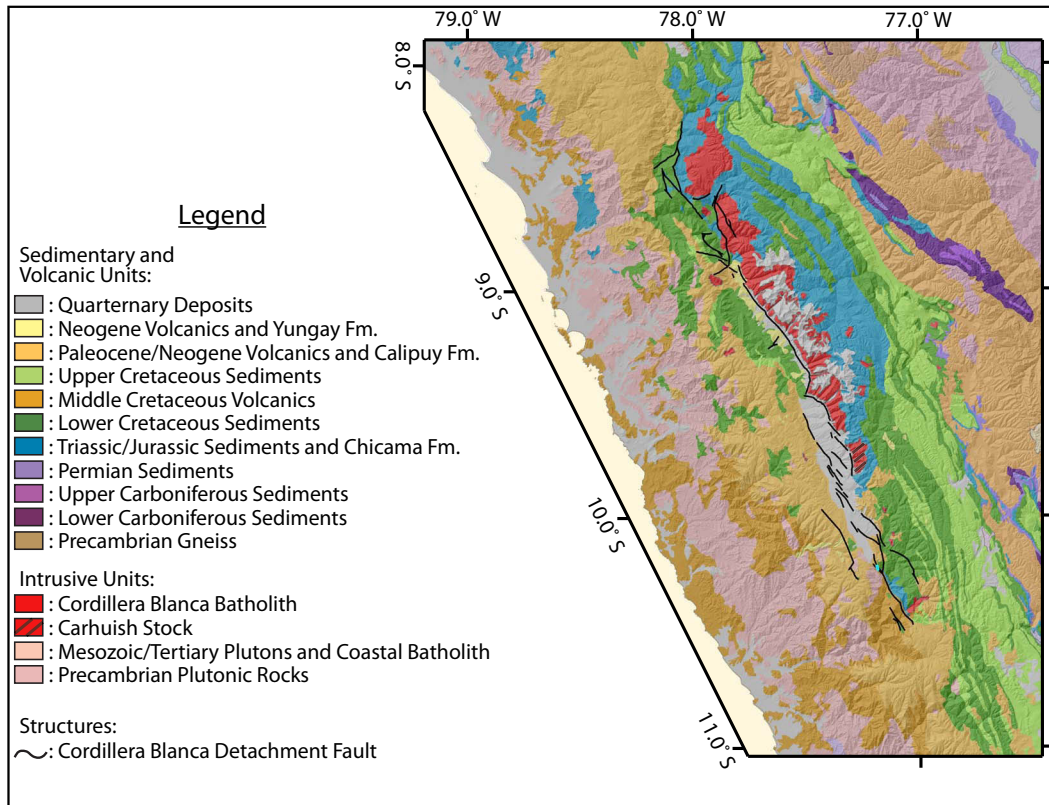


Figure 5. Geologic map of the greater Cordillera Blanca region overlain onto a hillshade topographic map. Black lines refer to structures associated with the CBDF. Lithologic units and their locations modified from the INGEMET digital geologic map of Peru. Hillshade produced from 90 m SRTM DEMs (USGS, 2006).



Figure 6: Mylonitized granitoids from the Cordillera Blanca Batholith, taken from Ulla Valley adjacent to the south side of Mt. Huascarán (Fig. 2A). Foliation is well developed (A) and rotated plagioclase clasts indicating a normal sense of motion are abundant (B).

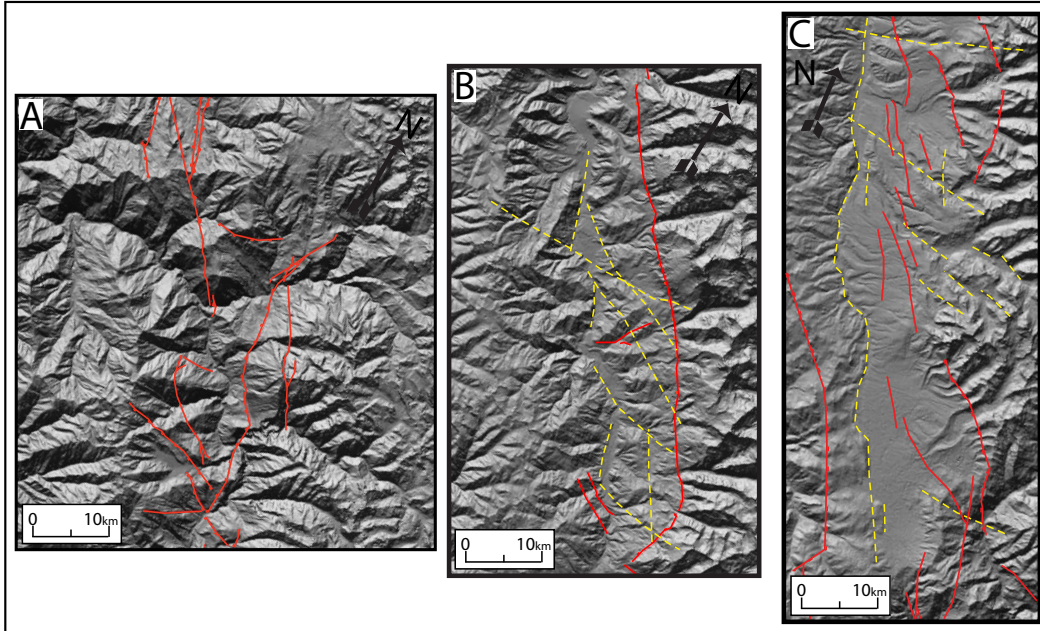


Figure 7. Structural maps of portions of the Cordillera Blanca. See Figure 2B for locations of figures. Red lines are structures associated with the CBDF from 1:100,000 scale INGEMMET geologic maps. Dashed yellow lines are prominent lineations possibly representing additional structures. (A) The structurally complex region near Huallanca where the known extent of the CBDF ends. (B) Northern portion of the Callejón de Huaylas Supradetachment basin. The CBDF is well defined here, but linear features opposite the CBDF and crossing the valley could indicate more complex patterns of extension in this region. (C) Southern end of the Callejón de Huaylas Supradetachment basin. Here the CBDF horsetails and splays, distributing extension across many fault strands. The sharp face along the opposite side of the valley may indicate the presence of a full graben. Base map is shaded relief topography produced from 90 m SRTM DEMs (USGS, 2006).

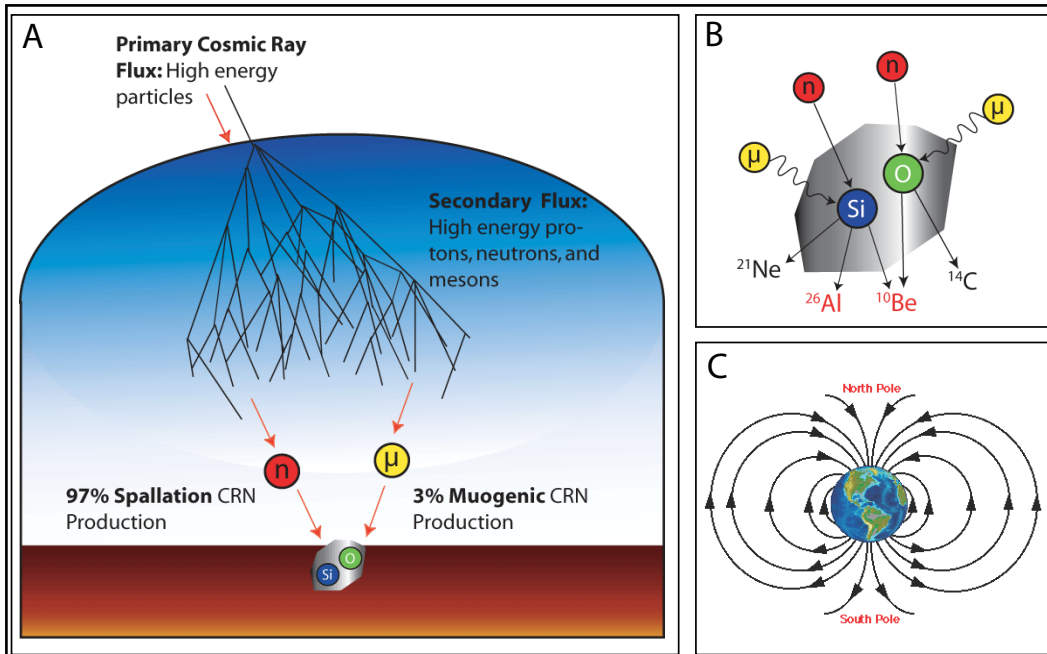


Figure 8. Cartoons of CRN production phenomena. (A) Incoming primary cosmic ray flux and the production of the secondary cosmic ray flux as neutrons (spallation) and muons (muogenic interactions). (B) Reactions in a target mineral to produce ^{26}Al and ^{10}Be from Si and O atoms. (C) Schematic image of the earth's magnetic field, showing lines of equal strength as parallel to the earth's surface near the equator. Image modified from: <http://www.unc.edu/depts/oceanweb/turtles/geomag.html>.

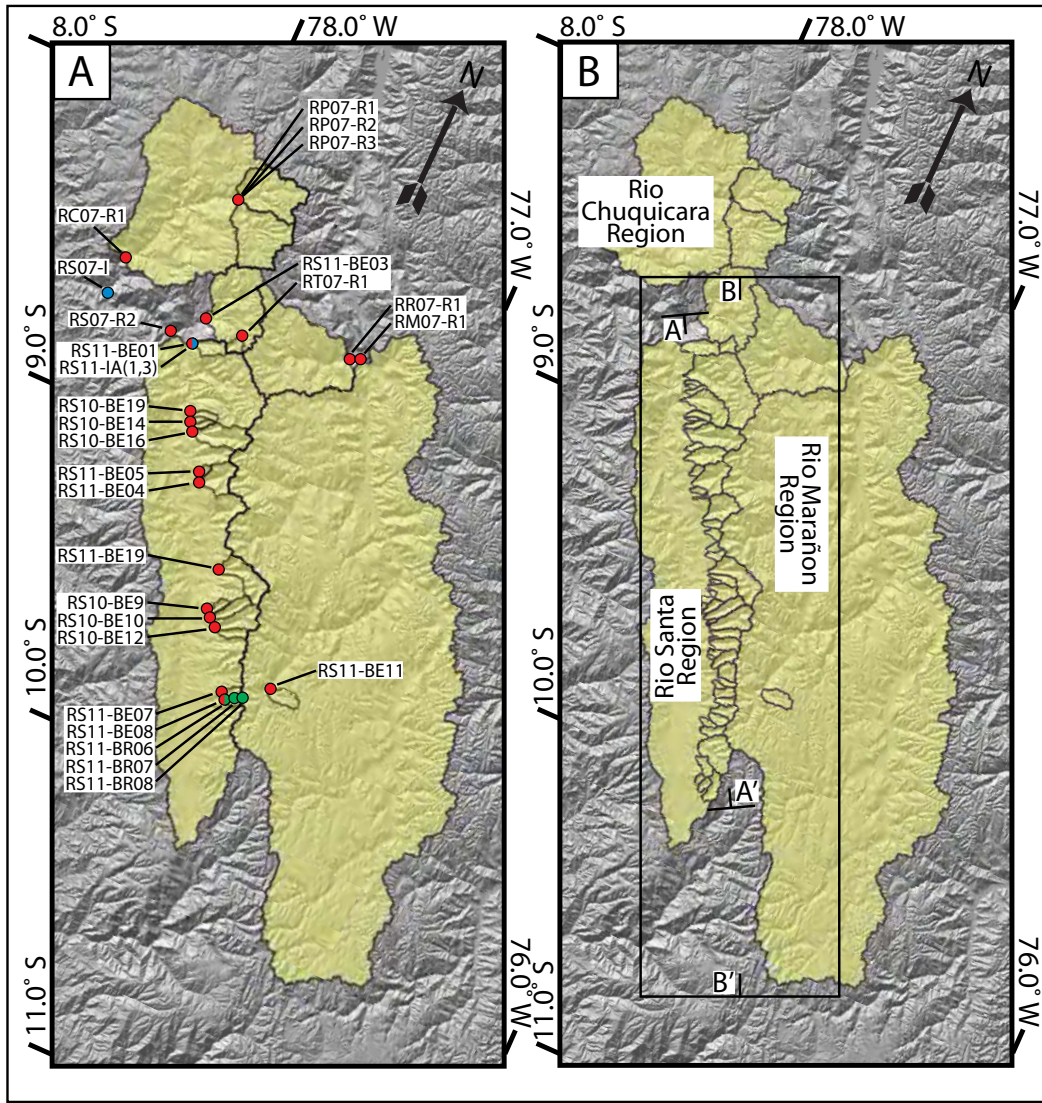


Figure 9. Maps of sample locations and basins used for morphometric analysis. (A) Map displaying the locations of samples collected for this study: ^{10}Be erosion rate (red dots), ^{10}Be surface exposure age (Blue dots), and thermochronology (green dots). Dots with 2 colors indicate 2 types of analyses at a given location. Yellow shaded areas indicate up-stream extent of basins used to find a ^{10}Be basin-averaged erosion rate. (B) Map showing basins and zones used for morphometric analysis. Yellow shaded areas indicate basin extents used to calculate basin morphometrics. A to A' marks the reference line used to compare along-strike trends in basin statistics in Figure 8. Black box and B to B' indicate the area used for generation of swath profiles and the reference scale used in Figure 9. Base maps are hillshade topography produced from 90 m SRTM DEMs (USGS, 2006).

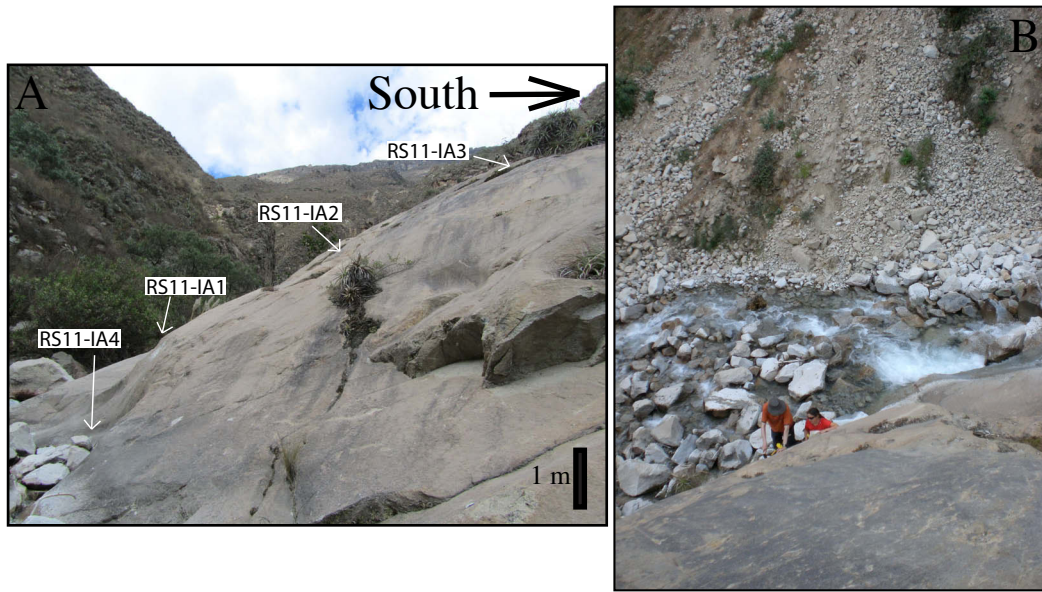


Figure 10. Photographs of the location of the Cordillera Blanca incision rate transect (RS11-IA; Fig. 9A). (A) Eastward view of sampled outcrop of fluvially polished granitoid bedrock with ~10 m total relief above river bed. Arrows indicate location of bedrock samples from vertical transect. (B) View looking down from top of outcrop (upper-right corner on Left). Note active channel at base and people for scale.



Figure 11. Photographs of typical CRN basin-averaged erosion sample collection site. (A) Location of sample collection (RS11-BE05) adjacent to active channel. Sample comes from a small eddy allowing accumulation of finer grained material compared to bedload in center of channel (B).

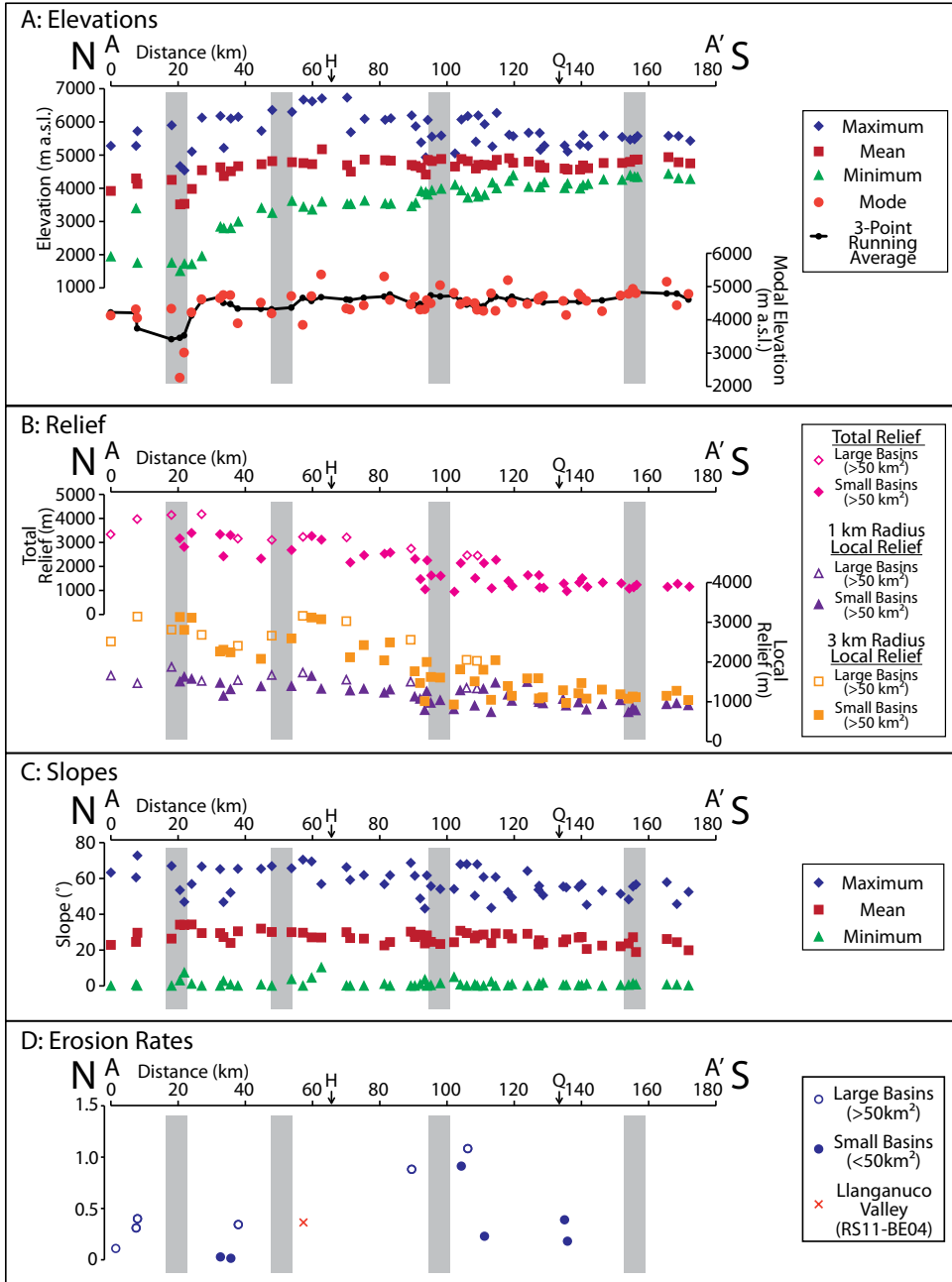


Figure 12 (previous page). Patterns of basin morphometry from basins along the CBDF along the transect A-A' (Fig. 9B). (A) Along-strike results of basin elevations including: maximum (blue diamonds), mean (dark red squares), minimum (green triangles), and modal (red circles). A running average is included for modal elevation (black line). Maximum elevations reach a maximum around 60 km south. Minimum elevations decrease northward. Mean and modal elevations remain fairly constant along much of the transect. (B) Along-strike results for relief within basins along the CBDF. Three forms of relief are shown: total basin relief (pink diamonds), 1 km local relief (purple triangles), and 3 km local relief (orange squares). Hollow shapes represent basins larger than 50 km². Note consistent southwards decrease in relief and position of larger basins relative to smaller ones nearby. (C) Basin slopes plotted against distance along-strike. Maximum (blue diamonds), mean (red squares) and minimum (green triangles) slope are shown. (D) ¹⁰Be basin averaged erosion rates from basins along the CBDF. Hollow circles represent basins larger than 50 km², the red cross represents sample RS11-BE04, which may be inaccurate (see text). Vertical grey bars represent approximate locations of the fault segment boundaries suggested by Schwartz (1988). All morphometrics were calculated using 90 m SRTM DEMs (USGS, 2006).

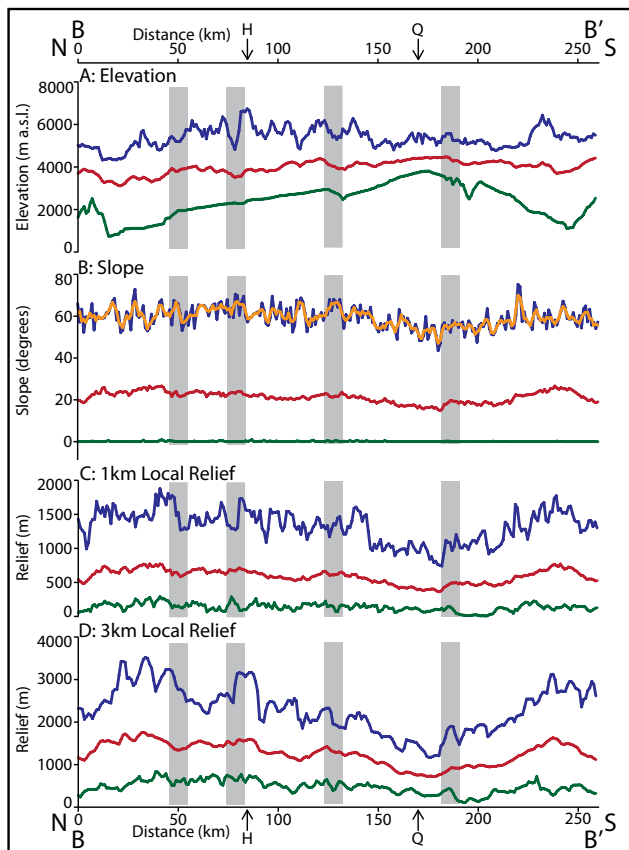


Figure 13. Swath profile results. Refer to Figure 9B for swath transect location (B-B'). In all cases blue, red and green lines are maximum, mean and minimum values, respectively. (A) Elevations, (B) slopes with running average from maximum slope shown as orange line, (C) 1km local relief, and (D) 3km local relief. Vertical grey bars represent approximate locations of the fault segment boundaries suggested by Schwartz (1988). Mean and minimum elevations decrease northward, but maximum elevations reach a maximum near 80 km south. Slope and relief decreases northward. All values were calculated using 90 m SRTM DEMs (USGS, 2006).

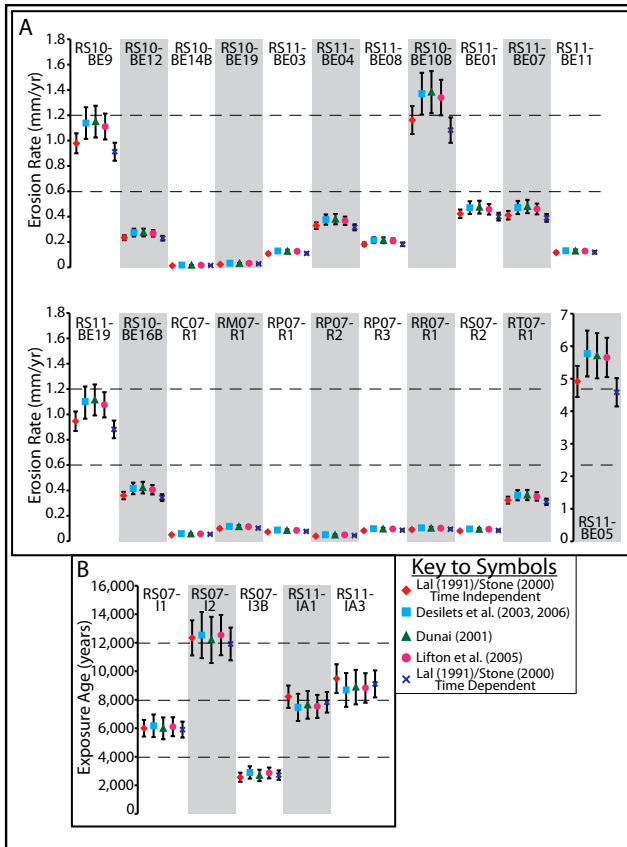


Figure 14. Erosion rates and exhumation ages calculated using various ^{10}Be scaling schemes. (A) Erosion rate results and (B) exposure age results. Symbols refer to the production models of: Lal (1991)/Stone (2000) (time invariant; red diamonds), Desilets et al. (2003 and 2006; light blue squares), Dunai (2001; green triangles), Lifton et al. (2005; pink circles), and Lal (1991)/Stone (2000) (time dependent; dark blue crosses). Note variance in age between methods relative to analytical errors. All ages calculated with the CRONUS web-based calculator (Balco et al., 2008).

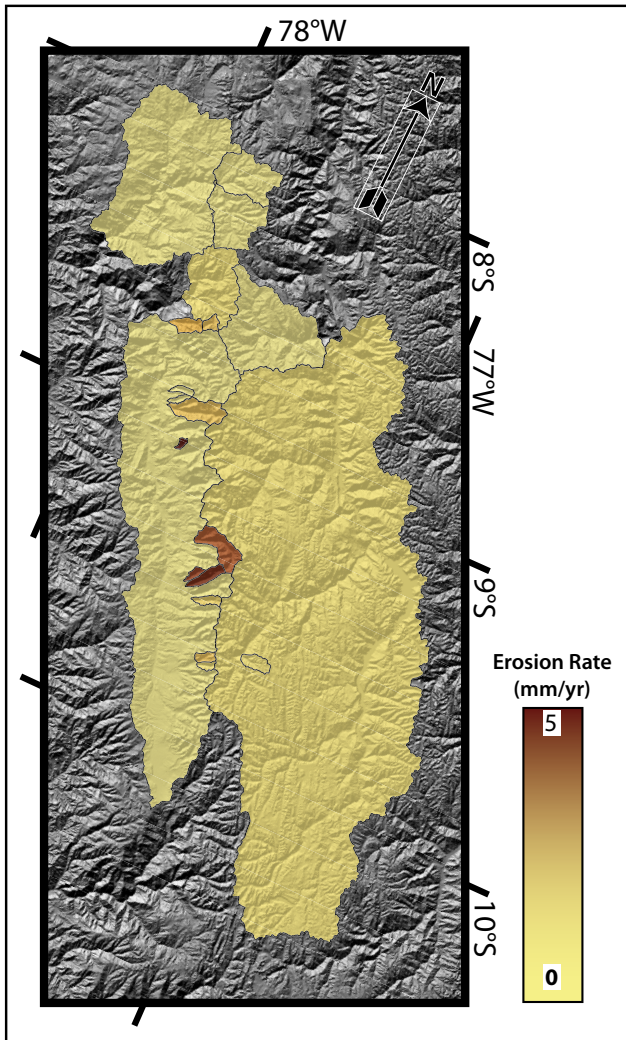


Figure 15. Map of ^{10}Be erosion rates measured in this study. Shaded regions mark the extent of measured basins (Fig. 9), and basin color represents the measured erosion rate from that basin in mm yr^{-1} . Note occurrence of high erosion rates in the small basins of the Cordillera Blanca. Base map is shaded relief topography produced from 90 m SRTM DEMs (USGS, 2006).

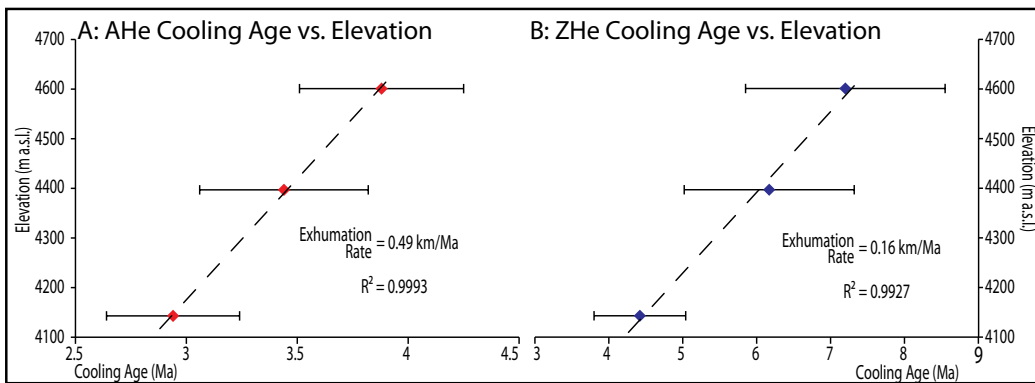


Figure 16. U-Th/He age-elevation plots. (A) AHe cooling ages and sampling elevations. Exhumation rate is 0.49 mm yr^{-1} . (B) ZHe cooling ages and sampling elevations. Exhumation rate is 0.16 mm yr^{-1} . All errors represent 1σ confidence intervals based on the analysis of 5 grains from each sample. AER results represent linear best fit to the mean ages for each sample.

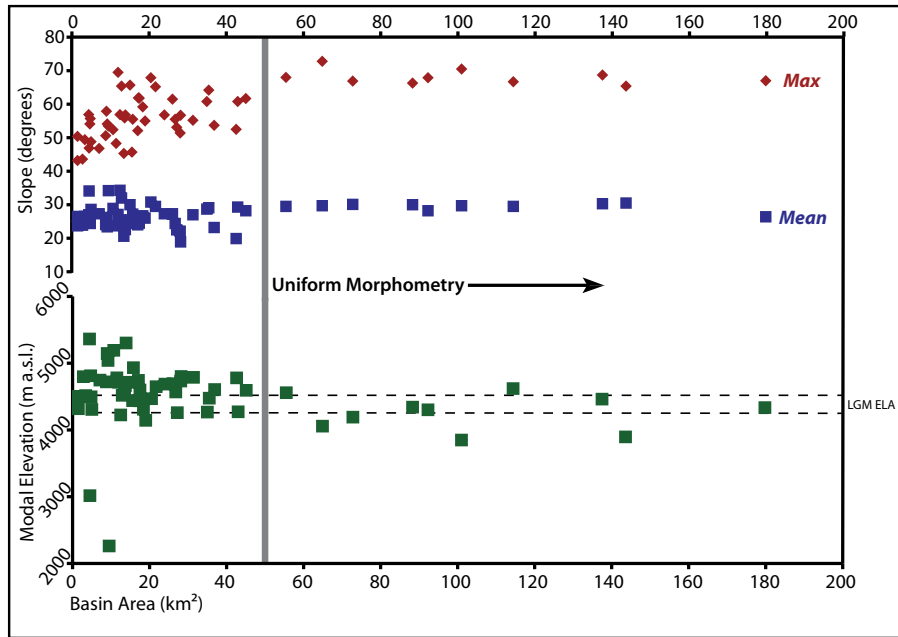


Figure 17. Plots of maximum (red diamonds) and mean (blue squares) basin slope and modal elevation (green squares) against basin area. Grey bar mark the break between the smaller, less consistent basins and the larger, more uniform basins, possibly reflecting maturity. Dashed line marks the approximate elevation of the LGM ELA after Smith et al. (2005).

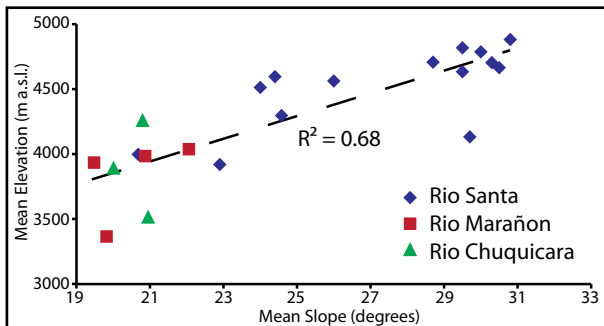


Figure 18. Mean slope vs. mean elevation plot for all basins used for ^{10}Be basin-averaged erosion rates analysis showing possible positive correlation. Basins from the 3 regions are identified: the Rio Santa (blue diamonds), Rio Marañon (red squares), and Rio Chuquicara (green triangles). Regression is linear best-fit to all samples shown.

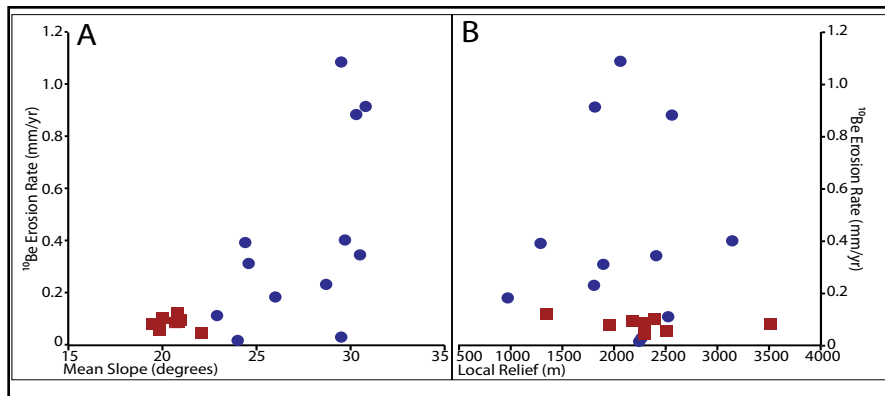


Figure 19. Mean slope (A) and local 3 km radius relief (B) vs. erosion rate plots for all ^{10}Be erosion rates measured. Symbols represent the glacial basins of the Cordillera Blanca mountain range (blue circles) and the fluvial basis measured elsewhere in the region (red squares).

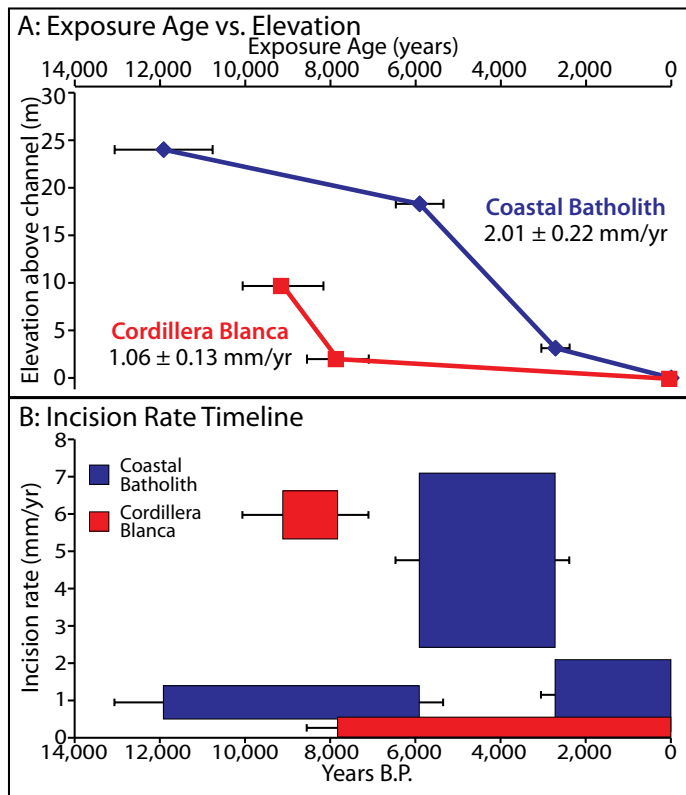


Figure 20. Exposure age vs. elevation and river incision rate plots from the two vertical transect locations: the Coastal Batholith (blue) and the CBB (red). (A) Exposure age vs. elevation relationships from the 2 locations, including overall incision rates. (B) Short-term incision rates recorded over the time-span of the samples. Error bars represent analytical and measurement errors. Coastal batholith location is incising twice as quickly overall. Cordillera Blanca locality may record relief generation across the CBDF.

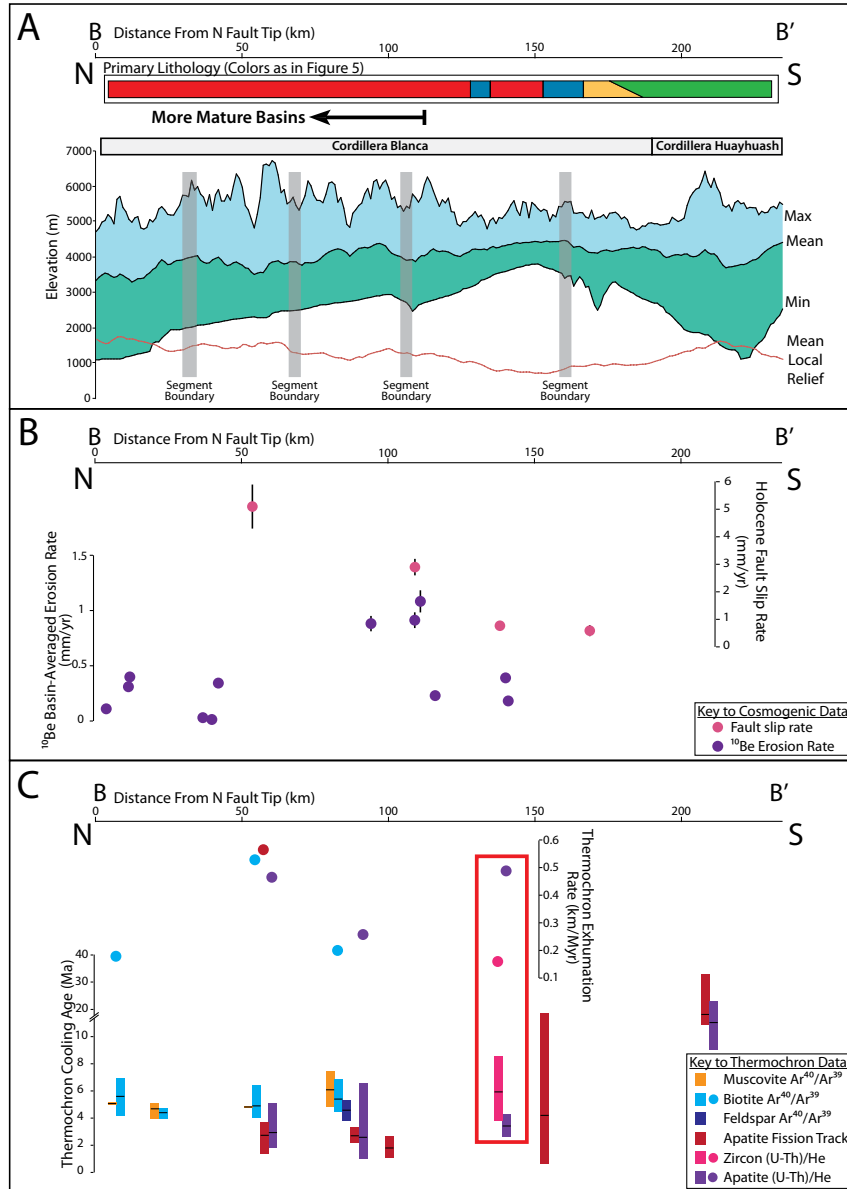


Figure 21. Synthesis figure comparing results from range morphology, lithology, structure, erosion and exhumation rates, and cooling ages. All data is plotted against its relative position along the transect B-B' (Fig. 9B). (A) Elevation swath profile displaying maximum, mean, and minimum elevations and mean 3 km local relief. Vertical grey bars represent approximate locations of the fault segment boundaries suggested by Schwartz (1988). Colored bar shows primary lithology for that portion of the range; colors correspond lithologies in Figure 5. (B) CRN basin-averaged erosion rates and Holocene fault slip rates for the CBDF (Farber and Hancock, in prep). All data shown with analytical error. Elevated erosion rates correspond to segment boundary. (C) Thermochronologic cooling ages and exhumation rates from the data discussed in text. Thermochronologic cooling ages are shown as bars spanning all measured ages from a given valley or transect, including reported errors. Note lack of differences between similar methods. Ages and exhumation rates in red box are from this study, others are from: Giovanni (2007), Montario (2001), and Garver et al. (2005). No errors are reported on exhumation rates due to a lack of proper thermal model for the CBB and surrounding region. Exhumation rates from Llanganuco Valley (around 55 km south) are consistently high compared to the rest of the range.

Tables

Table 1. Morphometric Statistics of Basins Along the Western Cordillera Blanca

Basin Name ^a	Sample Name ^b	Basin Area (km ²)					Basin-Wide Elevation (m a.s.l.)					Relief (m)			Slope (°)			Glacial Cover ^c		Distance South Along Strike (km) ^d
		Min	Max	Mean	Mode	Median	Range	Relief ^e (1km Circle)	Relief ^e (3km Circle)	Min	Max	Range	Mean	Area (km ²)	% Cover					
Yancu	RS11-BE03	515.0	1942	3920	4131	4062	3337	1659	2517	0.0	63.3	63.3	22.9	0.0	0.0	0.0	0.0	0.0		
-	RT10-R1	28.0	3392	5279	4297	4318	4291	1887	1109	1896	0.7	60.6	59.9	24.6	0.0	0.0	7.5			
Coronquillo	RS11-BE01	64.9	1751	5722	4133	4057	4340	3971	1467	3144	0.0	72.8	72.8	29.7	0.0	0.0	7.9			
Quintanasca	-	179.8	1754	5899	4254	4335	4300	4145	1877	2815	0.0	67.0	67.0	26.4	14.6	8.1	18.1			
Jatunpuco	-	9.5	1503	4667	3513	2262	3381	3164	1507	3133	3.0	53.5	50.5	34.2	0.0	0.0	20.6			
Catamarca	-	4.5	1723	4538	3533	3016	3399	2815	1626	2810	7.4	46.9	39.6	34.1	0.0	0.0	21.9			
Cajamarca Grande de los Cedros	-	12.5	1710	5105	3981	4225	4266	3395	1575	3115	1.1	56.9	55.9	34.3	0.0	0.0	24.1			
Rojayaco	RS10-BE19	114.4	1952	6128	4544	4620	4645	4176	1524	2684	0.0	66.7	66.7	29.5	16.0	14.0	27.1			
Carhuallán	-	7.1	2793	5216	4367	4747	4565	3338	1474	2266	0.0	65.2	65.2	29.5	3.5	16.1	32.6			
Raucocha	RS10-BE14	17.1	2796	6101	4513	4743	4659	3305	1313	2244	0.7	52.1	51.4	24.0	1.4	8.2	35.7			
Santa Cruz	RS10-BE16	143.6	2993	6152	4665	3896	4701	3159	1544	2408	0.0	65.4	65.4	30.5	29.6	20.6	37.9			
Huancotampampa	-	12.9	3404	5730	4725	4519	4787	2326	1387	2080	0.7	65.4	64.7	32.0	2.9	22.6	44.8			
Paron	-	72.8	3254	6358	4818	4192	4849	3104	1673	2663	0.0	66.9	66.9	30.1	24.9	34.2	48.0			
Raururi	RS11-BE05	15.1	3616	6301	4787	4715	4754	2685	1393	2594	3.7	65.7	62.0	30.0	5.4	36.0	53.9			
Llanganuco	RS11-BE04	101.0	3439	6670	4760	3849	4736	3231	1735	3162	0.0	70.5	70.5	29.7	24.8	24.6	57.3			
Armapampa	-	12.0	3354	6708	5176	5363	5180	3114	1325	3077	10.3	56.9	46.6	27.0	8.2	187.0	62.8			
Lullayacu	-	88.3	3523	6733	4697	4342	4674	3210	1556	3028	0.1	66.3	66.2	30.0	22.7	25.7	70.3			
Ulla	-	4.4	3594	6708	5176	5363	5180	3114	1325	3077	10.3	56.9	46.6	27.0	8.2	187.0	62.8			
Gatuy	-	18.4	3524	6690	4501	4310	4526	2166	1281	2119	0.0	59.2	59.2	26.7	3.5	19.3	71.4			
Hualcan	-	17.3	3623	6090	4866	4437	4877	2467	1324	2426	1.0	56.8	55.8	22.6	9.4	67.8	81.6			
Alauquey	-	13.9	3536	6063	4846	5303	4982	2527	1227	2042	0.0	61.8	61.8	24.5	8.5	48.7	83.3			
Lepimayuy	-	17.5	3531	6109	4833	4598	4820	2578	1306	2493	0.0	68.7	68.7	20.3	36.4	26.5	89.5			
Huanda	RS11-BE19	26.1	3557	2869	4672	4695	4699	2312	1129	1767	0.0	61.5	61.5	27.3	3.2	12.4	90.7			
Akllipoo	-	1.9	3847	6072	4672	4695	4699	2312	1129	1767	0.0	61.5	61.5	27.3	3.2	12.4	90.7			
Yanacocha	-	1.3	3884	4933	4114	4318	4433	1049	790	1015	3.5	43.3	39.7	23.7	0.3	6.4	93.7			
Chupay	-	4.5	3807	6061	4857	4594	4855	2254	1261	2001	0.0	61.7	61.7	28.7	10.3	22.7	94.3			
Alfaca	-	4.8	3933	5557	4820	4097	4789	1624	972	1624	0.3	55.7	53.4	24.2	0.3	6.9	95.5			
Mullaca	-	9.2	3981	5589	4883	5041	4892	1608	1039	1608	1.4	54.1	52.7	23.4	4.6	50.3	98.3			
Alfaca	-	4.7	4102	5051	4655	4812	4680	949	811	931	4.9	54.1	49.2	24.4	0.0	0.0	102.4			
Llaca	RS10-BE9	20.5	3932	6072	4882	4468	4883	2140	1286	1815	0.7	67.9	67.2	30.8	6.0	29.5	104.3			
Churo	RS10-BE10	55.5	3715	6176	4818	4558	4834	2461	1349	2055	0.0	68.0	68.0	29.5	9.9	17.8	106.2			
Churo	-	1.5	3891	5405	4595	4504	4602	1514	901	1514	0.8	50.4	49.5	26.5	0.1	9.3	108.6			
Quilichuanca	-	92.3	3743	6195	4704	4302	4759	2137	1324	1806	0.0	67.9	67.9	28.2	18.1	19.6	109.3			
Churup	RS10-BE12	35.0	3794	5931	4708	4268	4759	2137	1324	1806	0.0	60.8	60.8	28.7	7.7	22.0	111.2			
Shallap	-	2.8	4167	5259	4689	4798	4722	1092	738	1049	2.3	43.6	41.3	23.9	0.0	0.0	113.5			
Raururi	-	43.0	3995	6270	4858	4272	4855	2275	1478	2047	0.0	60.8	60.8	29.3	11.2	26.0	114.8			
Raucocha	-	10.7	4216	5613	4905	5193	4916	1397	1177	1397	0.2	52.4	52.2	28.9	4.2	38.8	118.5			
Cashan	-	3.4	4388	5571	4768	4515	4703	1183	1023	1183	0.0	64.2	64.2	29.1	8.2	23.0	124.3			
Shashua	-	35.5	4038	5673	4806	4476	4833	1635	1036	1591	0.2	53.7	53.4	23.2	5.7	15.4	127.6			
Rurec	-	36.9	4029	5667	4703	4606	4661	1124	991	1085	1.2	55.9	54.8	25.5	0.0	0.0	127.8			
Punahuaganga	-	13.7	4032	5288	4618	4720	4606	1113	959	1113	1.7	50.6	48.9	24.1	0.0	0.5	129.0			
Aranaca	-	8.8	4175	5288	4596	4569	4604	1289	1069	1289	0.5	55.5	55.0	24.4	1.8	6.7	135.0			
Quilco	RS11-BE07	26.8	4002	5291	4596	4569	4604	1289	1069	1289	0.5	55.5	55.0	24.4	1.8	6.7	135.0			
Yanamary	RS11-BE08	19.0	4137	5108	4563	4144	4582	971	904	971	0.5	55.0	54.5	26.0	0.1	0.4	135.9			
Conde	-	31.4	3988	5318	4565	4788	4584	1330	983	1213	0.3	55.2	54.9	27.0	0.5	1.6	139.6			
Pamparaju	-	24.0	4091	5600	4689	4687	4693	1509	1102	1470	0.3	56.8	56.5	27.3	2.3	9.6	140.5			
Maryhuca	-	13.5	4127	5275	4605	4570	4716	1148	803	1080	1.0	45.3	44.3	20.6	0.3	2.1	142.0			
Tranco Ruri	-	27.2	4259	5587	4763	4733	4757	1295	939	1307	0.0	53.1	53.1	22.5	4.7	17.4	146.6			
Raria	-	28.1	4251	5546	4763	4733	4757	1295	939	1307	0.0	53.1	53.1	22.5	4.7	17.4	146.6			
Tanash	-	11.5	4388	5466	4796	4781	4783	1078	737	1078	0.5	48.3	47.8	23.7	0.4	3.5	154.5			
Huayllaco	-	15.8	4346	5478	4864	4933	4879	1132	849	1132	1.3	55.5	54.2	27.2	0.2	1.0	155.8			
Huacuco	-	28.2	4338	5574	4868	4801	4826	1236	783	1115	0.7	56.7	56.1	18.9	0.0	0.0	156.7			
Huacuco	-	9.0	4430	5580	4939	5146	4915	1150	938	1150	0.7	57.9	57.1	26.2	0.0	0.0	165.9			
Jeullesh	-	15.6	4298	5574	4781	4779	4781	1276	961	1276	0.6	48.7	48.2	24.4	0.0	0.0	168.9			
Paray	-	42.6	4275	5431	4780	4746	4746	1156	910	1043	0.2	52.5	52.3	19.9	0.0	0.0	172.4			

a. Basin names are given where known. Names of major rivers are used where no basin name can be identified.
b. The samples used for basin-averaged erosion rates.
c. Glacier areas determined using the GLIMS glacier database (Armstrong, et al., 2005).
d. Distances correspond to reference line A-A' from Fig. 5.

Table 2. Morphometric Statistics of Other Basins of Interest to this Study

Region ^a	Corresponding Sample Name ^b	Area (km ²)	Basin-Wide Elevation (m a.s.l.)				Relief (m)			Slope (Degrees)				
			Min	Max	Mean	Mode	Median	Total Basin	Relief (1km Circle)	Relief (3km Circle)	Min	Max	Range	Mean
Rio Marañon	RS11-BE11	56.6	3269	4741	4257	4481	4361	1472	910	1350	0.1	52.5	52.4	20.8
Rio Chuquicara	RC07-R1	2997	922	5018	3366	3977	3471	4096	1550	2510	0	66.32	66.32	19.82
Rio Marañon	RM07-R1	14058	2123	6418	3890	3364	4006	4295	1674	2388	0	74.03	74.03	20.01
Rio Chuquicara	RP07-R1	326	2178	4871	3935	3977	4102	2693	1261	1958	0	64.91	64.91	19.48
Rio Chuquicara	RP07-R2	367	2175	5008	4038	4010	4176	2833	1343	2292	0	64.48	64.48	22.06
Rio Chuquicara	RP07-R3	696	2131	5008	3985	3977	4138	2877	1343	2292	0	64.91	64.91	20.87
Rio Marañon	RM07-R1	954	2123	4584	3513	2123	3593	2461	1655	2179	0	63.91	63.91	20.95
Rio Santa	RS07-R2	5752	1117	6733	3998	4022	4122	5616	1877	3520	0	72.82	72.82	20.68

a: Regions are as discussed in text.

b: ¹⁰Be samples used for basin-averaged erosion rates.

Table 3. ¹⁰Be Sample Information

Sample	Grain Size ^a (mm)	Sample Thickness ^b (mm)	Latitude ^c (d.d.)	Longitude ^d (d.d.)	Elevation ^e (m a.s.l.)	Air Pressure ^f (hPa)	Assumed Erosion Rate ^g (mm yr ⁻¹)	¹⁰ Be Concentration (atoms g ⁻¹)	Topo-Shielding Factor ^h	Basin Area (km ²)	Niemi et al. (2005) Min Area ⁱ (km ²)
RS10-BE9	0.25 - 1.4	-	-9.4363	-77.4469	4882	564.77	-	3.10E+04 ± 6.5E+02	0.96	20.5	109.6
RS10-BE12	0.25 - 1.0	-	-9.4995	-77.3691	4708	577.56	-	1.21E+05 ± 3.6E+03	0.96	35.0	435.0
RS10-BE14B	0.25 - 1.0	-	-8.9073	-77.7643	4513	602.56	-	2.05E+06 ± 3.5E+04	0.95	17.1	6675.6
RS10-BE19	0.25 - 1.0	-	-8.8872	-77.7481	4665	591.65	-	1.16E+06 ± 2.1E+04	0.97	21.7	3597.1
RS11-BE03	0.25 - 0.5	-	-8.5260	-77.8032	4367	580.45	-	2.32E+05 ± 4.1E+03	0.98	515.0	906.1
RS11-BE04 ^h	0.25 - 0.5	-	-9.0564	-77.6227	4634	582.72	-	9.31E+04 ± 2.7E+01	1	101.0	-
RS11-BE05 ^h	0.25 - 0.5	-	-9.0528	-77.6744	4787	571.60	-	5.90E+03 ± 3.5E+02	0.95	15.1	21.8
RS11-BE08	0.25 - 0.5	-	-9.7024	-77.2757	4563	587.95	-	1.48E+05 ± 2.6E+03	0.97	19.0	550.4
RS10-BE10B	0.5 - 2.0	-	-9.4879	-77.4592	4818	533.40	-	2.78E+04 ± 1.5E+03	0.96	55.5	92.3
RS11-BE01	0.25 - 0.5	-	-8.6979	-77.8875	4133	605.73	-	5.74E+04 ± 1.3E+03	0.96	64.9	249.9
RS11-BE07	0.25 - 0.5	-	-9.7031	-77.3144	4596	569.94	-	7.26E+04 ± 1.7E+03	0.97	26.8	256.1
RS11-BE11	0.25 - 2.0	-	-9.6173	-77.1814	3242	679.72	-	1.42E+05 ± 3.8E+03	0.99	56.6	839.8
RS11-BE19	0.25 - 0.5	-	-9.3338	-77.4973	4704	561.85	-	3.23E+04 ± 7.7E+02	0.95	137.5	113.4
RS10-BE16B	0.25 - 0.5	-	-8.9553	-77.7741	4665	564.76	-	8.34E+04 ± 1.6E+03	0.95	143.6	291.3
RC07-R1	-	-	-8.2017	-77.9424	3366	803.87	-	1.55E+03 ± 8.1E+02	0.99	2997.0	1854.9
RM07-R1	-	-	-8.2017	-77.9424	3890	646.79	-	1.70E+03 ± 8.9E+02	1	14058.0	973.2
RP07-R1	-	-	-8.2056	-77.9498	3935	679.34	-	1.68E+03 ± 8.8E+02	0.99	326.0	1304.8
RP07-R2	-	-	-8.5336	-78.2059	4038	679.34	-	1.71E+03 ± 8.9E+02	0.98	367.0	2257.8
RP07-R3	-	-	-8.6577	-78.2321	3986	679.34	-	1.27E+03 ± 6.6E+02	0.98	696.0	1161.7
RR07-R1	-	-	-8.5109	-77.3622	3513	713.20	-	1.69E+03 ± 8.8E+02	0.99	954.0	1060.5
RS07-R2	-	-	-8.6028	-77.7537	3998	662.90	-	1.26E+03 ± 6.6E+02	1	5752.0	1189.9
RT07-R1	-	-	-8.6874	-77.9686	4297	592.87	-	1.13E+03 ± 5.9E+02	0.98	28.0	322.3
RS07-11	-	10	-8.6600	-78.2091	558	950.43	0.001	1.92E+04 ± 6.0E+02	0.78	-	-
RS07-12	-	30	-8.6600	-78.2091	563.4	949.84	0.001	3.70E+04 ± 7.8E+02	0.78	-	-
RS07-13B	-	50	-8.6600	-78.2091	542.8	952.08	0.001	8.12E+03 ± 6.9E+02	0.78	-	-
RS11-1A1	-	20	-8.6980	-77.8875	2199	784.78	0.001	8.33E+04 ± 1.6E+03	0.86	-	-
RS11-1A3	-	20	-8.6980	-77.8875	2206.7	784.06	0.001	9.52E+04 ± 4.5E+03	0.86	-	-

a: All grains were ground to 0.25 to 0.5 mm, unless enough material could be recovered in that size fraction.

b: Measured as normal to exposed surface. Averaged where several pieces were collected.

c: Reported value is the mean for the corresponding basin area for all basin-averaged erosion rate samples.

d: Accounting for the regional pressure anomaly described in text and by Farber et al. (2005).

e: Erosion rate for exposure ages is assumed to be negligible, all samples were fluvially polished bedrock.

f: Reported error accounts for inaccuracies in laboratory procedures and analytical measurements.

g: Calculated using 90m SRTM DEMs (USGS, 2006).

h: Calculated as 100/Erosion Rate.

i: Sample contained excess Al, produced poor analytical result (see text).

Table 4: ^{10}Be Erosion Rate Results

Sample	Time Independent			Desillets et al. (2003, 2006)			Dunai (2001)			Lifton et al. (2005)			Time Dependent			Erosion Timescale (years)
	Lal (1991)/Stone (2000)			Desillets et al. (2003, 2006)			Dunai (2001)			Lifton et al. (2005)			Lal (1991)/Stone (2000)			
	Production rate (atoms $\text{g}^{-1} \text{yr}^{-1}$)	Erosion Rate (mm yr^{-1})	Error (mm yr^{-1})	Production rate (atoms $\text{g}^{-1} \text{yr}^{-1}$)	Erosion Rate (mm yr^{-1})	Error (mm yr^{-1})	Production rate (atoms $\text{g}^{-1} \text{yr}^{-1}$)	Erosion Rate (mm yr^{-1})	Error (mm yr^{-1})	Production rate (atoms $\text{g}^{-1} \text{yr}^{-1}$)	Erosion Rate (mm yr^{-1})	Error (mm yr^{-1})	Production rate (atoms $\text{g}^{-1} \text{yr}^{-1}$)	Erosion Rate (mm yr^{-1})	Error (mm yr^{-1})	
RS10-BE9	4.61E+01	9.8E-01	7.9E-02	1.1E+00	1.1E+00	1.2E-01	1.1E+00	1.3E-01	1.0E-01	1.1E+00	1.0E-01	9.1E-01	7.1E-02	649		
RS10-BE12	4.28E+01	2.3E-01	2.0E-02	2.7E-01	2.7E-01	3.1E-02	2.7E-01	3.1E-02	2.5E-02	2.7E-01	2.5E-02	2.3E-01	1.9E-02	2578		
RS10-BE14B	3.88E+01	1.2E-02	1.0E-03	1.8E-02	1.7E-02	2.0E-03	1.8E-02	1.9E-03	1.7E-03	1.7E-02	1.7E-03	1.5E-02	1.2E-03	39559		
RS10-BE19	4.23E+01	2.3E-02	1.9E-03	3.3E-02	3.1E-02	3.7E-03	3.3E-02	3.5E-03	3.2E-02	3.1E-02	3.1E-03	2.8E-02	2.2E-03	21316		
RS11-BE03	3.75E+01	1.1E-01	8.6E-03	1.3E-01	1.4E-02	1.4E-02	1.3E-01	1.4E-02	1.3E-01	1.3E-01	1.4E-02	1.1E-01	8.6E-03	5370		
RS11-BE04	4.31E+01	3.3E-01	2.6E-02	3.8E-01	4.0E-02	4.0E-02	3.8E-01	4.1E-02	3.8E-01	3.7E-01	3.3E-02	3.2E-01	2.4E-02	1852		
RS11-BE05	4.37E+01	4.9E+00	4.8E-01	5.8E+00	7.1E-01	7.1E-01	5.7E+00	6.9E-01	6.1E-01	5.7E+00	6.1E-01	4.6E+00	4.4E-01	129		
RS11-BE08	4.07E+01	1.8E-01	1.5E-02	2.1E-01	2.3E-02	2.3E-02	2.1E-01	2.3E-02	2.1E-01	1.9E-02	1.9E-02	1.8E-01	1.4E-02	3262		
RS10-BE10B	4.92E+01	1.2E+00	1.1E-01	1.4E+00	1.7E-01	1.7E-01	1.4E+00	1.7E-01	1.4E+00	1.3E+00	1.4E-01	1.1E+00	1.0E-01	547		
RS11-BE01	3.61E+01	4.2E-01	3.4E-02	4.7E-01	5.1E-02	5.1E-02	4.7E-01	5.1E-02	4.2E-02	4.6E-01	4.2E-02	4.0E-01	3.1E-02	1481		
RS11-BE07	4.52E+01	4.1E-01	3.4E-02	4.7E-01	4.8E-01	5.2E-02	4.7E-01	4.8E-01	4.3E-02	4.6E-01	4.3E-02	3.9E-01	3.1E-02	1518		
RS11-BE11	2.39E+01	1.2E-01	9.3E-03	1.3E-01	1.4E-02	1.4E-02	1.3E-01	1.4E-02	1.3E-01	1.3E-01	1.2E-02	1.2E-01	9.2E-03	4976		
RS11-BE19	4.63E+01	9.5E-01	7.7E-02	1.1E+00	1.2E-02	1.2E-02	1.1E+00	1.2E-02	1.0E-01	1.1E+00	1.0E-01	8.8E-01	7.0E-02	672		
RS10-BE16B	4.55E+01	3.6E-01	2.9E-02	4.2E-01	4.6E-02	4.6E-02	4.2E-01	4.6E-02	3.7E-02	4.1E-01	3.7E-02	3.4E-01	2.7E-02	1726		
RC07-R1	2.34E+01	5.0E-02	4.1E-03	5.9E-02	6.5E-03	6.5E-03	5.7E-02	6.2E-03	5.4E-02	5.8E-02	5.4E-02	5.4E-02	4.3E-03	10992		
RM07-R1	3.08E+01	9.9E-02	8.2E-03	1.2E-01	1.3E-02	1.3E-02	1.1E-01	1.2E-02	1.1E-01	1.1E-01	1.1E-02	1.0E-01	8.3E-03	5767		
RP07-R1	3.10E+01	7.3E-02	6.0E-03	8.7E-02	9.7E-03	9.7E-03	8.4E-02	9.2E-03	8.0E-03	8.5E-02	8.0E-03	7.7E-02	6.2E-03	7732		
RP07-R2	3.22E+01	4.0E-02	4.1E-03	5.1E-02	6.4E-03	6.4E-03	4.8E-02	6.1E-03	5.5E-03	4.9E-02	4.5E-03	4.4E-02	4.5E-03	13380		
RP07-R3	3.14E+01	8.2E-02	6.9E-03	9.8E-02	1.1E-02	1.1E-02	9.5E-02	1.1E-02	9.1E-03	9.6E-02	9.1E-03	8.6E-02	7.1E-03	6884		
RR07-R1	2.53E+01	9.1E-02	7.3E-03	1.0E-01	1.1E-02	1.1E-02	1.0E-01	1.1E-02	1.0E-01	1.0E-01	9.2E-03	9.4E-02	7.3E-03	6283		
RS07-R2	3.24E+01	8.0E-02	6.7E-03	9.6E-02	1.1E-02	1.1E-02	9.3E-02	1.0E-02	8.9E-03	9.4E-02	8.9E-03	8.4E-02	6.9E-03	7051		
RT07-R1	3.60E+01	3.2E-01	2.7E-02	3.6E-01	4.0E-02	4.0E-02	3.6E-01	4.0E-02	3.4E-02	3.5E-01	3.4E-02	3.1E-01	2.6E-02	1910		

Table 5: ^{10}Be Exposure Age Results

Sample	Time Independent			Desillets et al. (2003, 2006)			Dunai (2001)			Lifton et al. (2005)			Time Dependent		
	Lal (1991)/Stone (2000)			Desillets et al. (2003, 2006)			Dunai (2001)			Lifton et al. (2005)			Lal (1991)/Stone (2000)		
	Production rate (atoms $\text{g}^{-1} \text{yr}^{-1}$)	Exposure Age (years)	Error (Years)	Production rate (atoms $\text{g}^{-1} \text{yr}^{-1}$)	Exposure Age (years)	Error (Years)	Production rate (atoms $\text{g}^{-1} \text{yr}^{-1}$)	Exposure Age (years)	Error (Years)	Production rate (atoms $\text{g}^{-1} \text{yr}^{-1}$)	Exposure Age (years)	Error (Years)	Production rate (atoms $\text{g}^{-1} \text{yr}^{-1}$)	Exposure Age (years)	Error (Years)
RS07-11	3.14E+00	6005	584	6175	795	768	5998	6111	666	5907	559				
RS07-12	3.10E+00	12341	1230	12537	1618	1620	12199	12537	1411	11916	1150				
RS07-13B	3.02E+00	2564	318	2901	431	399	2693	2867	381	2718	332				
RS11-IA1	1.05E+01	8215	786	7468	953	972	7643	7536	809	7826	725				
RS11-IA3	1.05E+01	9482	1013	8688	1187	1212	8890	8829	1038	9113	948				

Table 6: Apatite (U-Th)/He Sample Information and Results

Sample Name	Latitude	Longitude	Elevation (m a.s.l.)	He (mol)	U (ppm)	Th (ppm)	Grain Mass (g)	Ft ^a	Grain Age ^b (Ma)	Average Age ^c (Ma)
RS11-BR06A1	-9.7136	-77.3080	4143	3.12E-15	24.9	52.2	6.11E-06	0.815	3.11 ± 0.05	
RS11-BR06A2	-9.7136	-77.3080	4143	1.26E-15	21.0	33.9	3.09E-06	0.791	3.27 ± 0.06	
RS11-BR06A3	-9.7136	-77.3080	4143	1.47E-15	30.3	61.2	2.64E-06	0.762	3.00 ± 0.05	2.94 ± 0.60
RS11-BR06A4	-9.7136	-77.3080	4143	9.43E-16	23.3	41.2	2.46E-06	0.767	2.79 ± 0.05	
RS11-BR06A5	-9.7136	-77.3080	4143	4.31E-16	22.2	36.5	1.46E-06	0.706	2.51 ± 0.04	
RS11-BR07A1	-9.6949	-77.2654	4397	1.09E-15	25.0	42.3	2.42E-06	0.765	3.11 ± 0.04	
RS11-BR07A2	-9.6949	-77.2654	4397	8.33E-16	0.0	0.0	1.91E-06	0.774	NaN ± NaN	
RS11-BR07A3	-9.6949	-77.2654	4397	4.37E-15	22.9	40.5	7.50E-06	0.829	3.98 ± 0.06	3.44 ± 0.38
RS11-BR07A4	-9.6949	-77.2654	4397	1.27E-15	19.1	33.9	3.31E-06	0.786	3.33 ± 0.06	
RS11-BR07A5	-9.6949	-77.2654	4397	1.85E-15	27.4	48.4	3.40E-06	0.773	3.34 ± 0.05	
RS11-BR08A1	-9.6889	-77.2526	4601	1.87E-15	27.2	44.4	3.00E-06	0.790	3.86 ± 0.06	
RS11-BR08A2	-9.6889	-77.2526	4601	4.39E-15	22.0	35.4	7.65E-06	0.846	4.12 ± 0.05	
RS11-BR08A3	-9.6889	-77.2526	4601	2.44E-15	20.1	33.1	4.71E-06	0.820	4.16 ± 0.06	3.88 ± 0.37
RS11-BR08A4	-9.6889	-77.2526	4601	2.16E-16	30.5	46.6	5.08E-07	0.579	3.25 ± 0.10	
RS11-BR08A5	-9.6889	-77.2526	4601	4.08E-15	29.4	42.9	5.78E-06	0.823	4.00 ± 0.06	

a: Ft is the alpha-ejection correction factor of Hourigan et al. (2005).

b: Age of individual mineral grain with analytical error.

c: Averaged age of 5 grains from same sample with 2σ error.

Table 7: Zircon (U-Th)/He Sample Information and Results

Sample Name	Latitude	Longitude	Elevation (m a.s.l.)	He (mol)	U (ppm)	Th (ppm)	Grain Mass (g)	Ft ^a	Grain Age ^b (Ma)	Average Age ^c (Ma)
RS11-BR06Z1	-9.7136	-77.3080	4143	2.28E-14	293.6	100.0	3.34E-06	0.728	5.44 ± 0.10	
RS11-BR06Z2	-9.7136	-77.3080	4143	2.07E-13	2068.3	312.8	5.58E-06	0.772	4.13 ± 0.10	
RS11-BR06Z3	-9.7136	-77.3080	4143	1.00E-13	2048.0	350.5	3.16E-06	0.724	3.80 ± 0.08	4.42 ± 0.62
RS11-BR06Z4	-9.7136	-77.3080	4143	6.88E-14	826.1	228.7	4.46E-06	0.743	4.34 ± 0.11	
RS11-BR06Z5	-9.7136	-77.3080	4143	8.84E-14	1222.4	265.2	3.94E-06	0.731	4.40 ± 0.08	
RS11-BR07Z1	-9.6949	-77.2654	4397	6.91E-15	169.1	56.6	1.86E-06	0.659	5.69 ± 0.11	
RS11-BR07Z2	-9.6949	-77.2654	4397	8.00E-14	4134.6	675.7	1.17E-06	0.626	4.70 ± 0.08	
RS11-BR07Z3	-9.6949	-77.2654	4397	7.62E-14	980.5	287.0	2.56E-06	0.708	7.39 ± 0.11	6.17 ± 1.15
RS11-BR07Z4	-9.6949	-77.2654	4397	2.46E-13	3249.3	1531.4	3.11E-06	0.696	5.78 ± 0.13	
RS11-BR07Z5	-9.6949	-77.2654	4397	1.14E-13	234.3	65.4	1.39E-05	0.828	7.31 ± 0.14	
RS11-BR08Z1	-9.6889	-77.2526	4601	3.98E-14	237.0	67.6	6.34E-06	0.787	5.82 ± 0.12	
RS11-BR08Z2	-9.6889	-77.2526	4601	7.25E-14	361.4	141.5	5.83E-06	0.776	7.49 ± 0.19	
RS11-BR08Z3	-9.6889	-77.2526	4601	6.14E-14	529.8	143.9	3.19E-06	0.717	8.76 ± 0.17	7.20 ± 1.35
RS11-BR08Z4	-9.6889	-77.2526	4601	1.05E-13	896.0	217.9	4.66E-06	0.754	5.80 ± 0.12	
RS11-BR08Z5	-9.6889	-77.2526	4601	1.09E-12	737.2	82.7	3.71E-05	0.876	8.15 ± 0.17	

a: Ft is the alpha-ejection correction factor of Hourigan et al. (2005).

b: Age of individual mineral grain with analytical error.

c: Averaged age of 5 grains from same sample with 2σ error.